Controls on granitic weathering fronts in contrasting climates

Nick R. Hayes[a], Heather L. Buss[a*], Oliver W. Moore[b], Pavel Krám[c], Richard D. Pancost[a,d]

[a] School of Earth Sciences, University of Bristol, Wills Memorial Building, Queens Road, Bristol, BS8 1RJ, UK

[b] School of Earth and Environment, University of Leeds, Maths/Earth and Environment Building, Leeds, LS2 9JT, UK

[c] Czech Geological Survey, Klárov 3, 118 21 Prague 1, Czech Republic

[d] Organic Geochemistry Unit, School of Earth Sciences, Cabot Institute for the Environment, University of Bristol, BS8 1RJ, UK

*H.Buss@bristol.ac.uk

Abstract

Granitic weathering profiles display highly diverse morphologies, reflecting the complex relationships between climate and weathering rates. Some profiles exhibit abrupt transitions from fresh bedrock to highly weathered material over short (<1 m) distances, while others exhibit only limited weathering extending 10s of meters into the bedrock. Although granitic weathering processes have been well studied, the controls on profile morphology and weathering rates within granitic, and many other lithologies remain poorly understood; these are likely influenced by a range of both intrinsic and extrinsic factors, which in turn will have crucial implications for understanding, for example, climate-weathering feedbacks. In this study we present multi-scale elemental and mineralogical analyses of a >30 m granitic weathering profile from the cool, temperate, Lysina catchment in the NW Czech Republic, from which we calculated mass transfer, weathering indices, and mineral specific weathering rates. The Lysina profile exhibits limited weathering extending

>30 m into fractured bedrock, dominated by albite weathering at a rate of 9.3 x 10^{-17} mol m^2 s^{-1}.

To identify environmental and geological controls on weathering front morphology and chemical weathering rates, Lysina was compared to previously published granitic weathering profiles from around the world. Weathering front morphology and weathering rates were calculated for the additional sites from published data and were correlated to mean annual precipitation (MAP), mean annual temperature (MAT), and erosion rates, with MAP having the strongest relationship. Higher MAP likely promotes lower saturation indices in pore waters, allowing weathering reactions to occur further from equilibrium. Comparison of erosion rates amongst the granitic catchments revealed an inconsistent effect on chemical weathering rates, but high erosion rates may promote weathering by reducing the thickness of the regolith and exposing the bedrock to reactive fluids. Mean annual temperatures appear to only have significant impacts on weathering fronts in environments with high precipitation and high erosion rates. Fractured bedrock profiles (Lysina and Río Icacos) have higher weathering intensities, than the other sites studied here. High connected porosity in fractured rocks enhances water movement allowing more efficient removal of weathering products, thus reducing thermodynamic saturation, increasing weathering rates, and producing sharper weathering gradients. These findings indicate that CO_2 drawdown on geological timescales is also likely to be governed by precipitation rates, as well as temperature, and that much of the climate-significant weathering may occur within very narrow zones of the Earth's surface.

Keywords: Chemical Weathering, Critical Zone, Weathering Rates, Granite, Erosion, Climate Feedbacks

1. Introduction

The chemical weathering of silicate minerals is generally accepted to be one of the primary controls on atmospheric CO_2 over geologic timescales and thus the long-term climate (>10^6 years) of the Earth (Berner et al., 1983). Although numerous factors operate on a range of scales to determine long-term silicate weathering rates, it is believed that the primary controls on these rates are climate and lithology (e.g., White and Blum, 1995; Riebe et al.,

2004; Maher, 2010). The relative influence of these two factors remains disputed, as well as the relative influence of different aspects of climate (i.e., temperature and precipitation), but typically, mafic lithologies weather more rapidly than felsic ones, and warmer, wetter climates promote more rapid weathering, with broad latitudinal trends identified in weathering profile morphology (Strakhov, 1967). Granitic lithologies, in particular, display large variations in weathering intensity compared to their mafic counterparts (Bazilevskaya et al., 2013). Although granitic weathering rates and mechanisms have been well studied (e.g., Melfi et al., 1983; White and Blum, 1995; Oliva et al., 2003; Riebe et al., 2004; Buss et al., 2005; Fletcher et al., 2006; Pierson-Wickmann et al., 2009; Frey et al., 2010), the controls that produce the variations in weathering front morphology, depth, and rates are not well understood. Greater constraint on these controls would enhance our ability to predict weathering responses through geologic time, as well as responses to future land use and climate change.

Most chemical weathering occurs in the Critical Zone, commonly defined as the region of Earth spanning the upper extent of vegetation to the lower extent of bedrock weathering. Significant differences exist in the intensity and depth of granitic weathering and the thickness of the weathering fronts in the critical zone. Some critical zone profiles exhibit only a few meters of weathering, whereas others show weathering to tens of meters deep (Bazilevskaya et al., 2013). The intensity of granitic weathering also varies significantly; some profiles weather from fresh bedrock to completely depleted regolith over weathering fronts less than 1 m thick, whereas other profiles show gradual alteration over tens of metres (e.g., Schaffhauser et al., 2014; Buss et al., 2017). It is unclear to what extent these variations are a product of the weathering environment or subtle differences in the mineralogy or intrinsic rock structure such as porosity and permeability. Regardless, these variations in weathering are likely to have implications for water flow rates and residence times within granitic profiles, which in turn could affect the coupling (or decoupling) of surface processes to those at depth and the flux of weathering products from the watersheds.

The depth of the bedrock-weathering boundary may also impact the initial weathering reactions. Weathering and biological reactions above weathering fronts can alter saturation indices and consume or produce reactants, such as CO_2 or O_2 in reactive fluids (Buss et al., 2005; Brantley et al., 2014). The manner and rate at which secondary porosity develops also

affects weathering mechanisms and fluid transport and can lead to distinct weathering morphologies (Navarre-Sitchler et al., 2011; Goodfellow et al., 2016).

Initiation of weathering in granitic rocks generally begins with either dissolution of highly reactive accessory minerals such as calcite (White et al., 2005) or oxidation of Fe(II) (Buss et al., 2008; Goodfellow et al., 2016). Similar reaction-driven fracturing mechanisms involving expansion during hydration of biotite (e.g., Isherwood and Street, 1976) or during hydrothermal alteration of mafic rocks (Røyne et al., 2008; Jamtveit et al., 2009) have been identified, but these mechanisms require connected pore space or exposed surfaces. Fracturing via oxidation of Fe(II), however, typically occurs within rocks where water cannot penetrate (Buss et al., 2008; Behrens et al., 2015) However, the majority of porosity formed during granitic weathering stems from the dissolution of aluminosilicate minerals, dominantly plagioclase (e.g., Buss et al., 2008). Typically, Ca and Na rich feldspars dissolve more rapidly than K rich feldspars (e.g., Bandstra et al., 2008). Relatively small variations in the composition and abundance of feldspars amongst granitic rocks may affect weathering rates within granitic lithologies (e.g., White et al., 2001). Furthermore, as the most abundant Ca-containing silicate mineral within most granitic rocks, the weathering of plagioclase is the dominant granitic weathering reaction contributing to CO_2 drawdown (e.g., Brantley et al., 2014).

As such, the chemical weathering of plagioclase minerals within the critical zone represents a major control on long-term climate. The initiation of weathering can begin 10s of meters below the rock-regolith interface (e.g., Riebe et al., 2017), but the practical difficulties in accessing and sampling weathering bedrock at depth means there are few available datasets appropriate for weathering studies that extend below the augerable, or outcropping, regolith (here defined as all disaggregated material overlying intact bedrock). The relatively limited number of such investigations means that our understanding of the fundamental processes that govern weathering profile development remain poorly understood (e.g., Bazilevskaya et al., 2013). In this study, we present new elemental and mineralogical data from a core drilled 30.3 m into a temperate granitic weathering profile, representing one of the first deep critical zone granitic weathering studies from such settings (e.g., White et al., 2001; Schaffhauser et al., 2014). Bulk rock and mineral-specific chemical weathering rates were calculated, and the intensity, depth, and morphology of the

weathering fronts were analysed. We compare these findings to granitic weathering profiles from the literature, spanning a range of precipitation and temperature regimes. These comparisons were used to assess the relative impact of weathering factors such as climate, lithology, and subsurface architecture (i.e., variations in primary and secondary porosity and permeability with depth) on the resulting weathering front morphologies and chemical weathering rates.

2. Methods

2.1. Primary field site

The small granitic catchment (0.273 km^2) of Lysina is part of the Slavkov Forest Critical Zone Observatory in the NW Czech Republic (Krám et al., 2012; Fig 1; Krám et al., 2017). The region is located within the so-called 'Black Triangle', an area of Central Europe heavily affected by pollution from coal-fired power plants (Krám et al., 1999; Kopacek et al., 2016). The region has been formally monitored by the Czech Geological Survey since 1989, with a focus on the recovery from anthropogenic acidification since the collapse of the Communist government of Czechoslovakia and the subsequent decommissioning or retrofitting of the power plants (Hruska et al., 2002; Krám et al., 2014).

The Lysina bedrock is dominated by leucogranite: a granite rock type high in silica, deficient in base metals (particularly Mg) (Krám et al., 1997), and containing a relatively high proportion of Li, present within micas such as zinnwaldite (Navrátil, 2000; Krám et al., 2012; Štědrá et al., 2016). The Lysina unit also contains smaller amounts of quartz monzonite and alkali-feldspar granite (Štědrá et al., 2016). Although a separate unit, the Lysina granite is associated with the Younger Intrusive Complex (YIC), a series of granitic intrusions dating from the late Carboniferous to early Permian (~300 Ma) (Blecha and Štemprok, 2012). The broad region remains hydrothermally active, and the Lysina catchment is located about 25 km from the spa town of Karlovy Vary which is renowned for its therapeutic, mineral-rich hot springs (Vylita et al., 2007).

Lysina is situated at a relatively high altitude (~900 m) and experiences a cool humid climate, and supports a managed coniferous forest consisting almost exclusively of Norway

spruce (*Picea abies*). Mean annual precipitation is approximately 950 mm yr^{-1} and the MAT is 5 ^{o}C (Table 1; Krám et al., 1997). The region is not believed to have been affected by glaciation, despite its cool climate and high altitude (Hruska et al., 2002; Krám et al., 2012). The base-poor nature of the underlying bedrock makes the catchment highly susceptible to acidification, and as a result, the stream waters of the Lysina catchment have a discharge-weighted annual mean pH of 4.2. This vulnerability to acidification was exacerbated, in particular, by sulfur pollution during the 1980s. While the catchment has recovered significantly, the stream waters of the Lysina catchment remain acidified relative to pre-1980s levels (Krám et al., 1999; Hruska et al., 2002; Kopacek et al., 2016).

The total denudation rates within the Lysina catchment, calculated from $^{10}Be/^{9}Be$ ratios, is 185 ± 23 t km^{-2} yr^{-1} (70 m Myr^{-1}), although only 10% of the total denudation is believed to be from chemical weathering (Dannhaus et al., 2018). Assuming that total denudation in Lysina is comprised of a 90/10 split of erosion (physical) to chemical weathering, erosion rates are therefore ~63 m Myr^{-1} and chemical weathering rates are ~7 m Myr^{-1}. Erosion rates within the Lysina catchment are considerably higher than those of the nearby Pluhův Bor (serpentinite bedrock 25 m Myr^{-1}) and Na Zelenem (amphibolite bedrock, 19 m Myr^{-1}) catchments, although chemical weathering rates are lower (Dannhaus et al., 2018).

2.2. Additional sites

To investigate the impact of climate on weathering front morphologies, geochemical data from previous studies of other granitic profiles were compiled for comparison to the Lysina profile. These sites experience a range of climates from cool temperate to humid tropical and have been extensively studied over the last two to three decades (Table 1). Bulk chemistry data were used to calculate mass transfer coefficients (normalized to Ti, due to its low mobility) and weathering indices for each site (e.g., Pavich, 1989; White et al., 2001; Buss et al., 2017). The deepest sample was used as the parent material in each case.

2.2.1. Davis Run, Virginia, USA

Davis Run is located within the Virginia Piedmont of the Eastern USA, and the catchment overlies the Cambrian-Ordovician age Occoquan granite (Pavich, 1989; White et al., 2001). The Occoquan granite is classified as a monzogranite with lesser granodiorite and tonalite, consisting primarily of K-feldspar and sodic to calcic plagioclase phases (Drake and Froelich,

1986; White et al., 2001). The catchment experiences a temperate climate but is warmer and slightly more humid than Lysina (Table 1).

2.2.2. Panola, Georgia, USA

The Panola catchment overlies the same Piedmont formation as Davis Run, although the Panola granodiorite contains more Ca plagioclase and is substantially younger (~320 Ma) (White et al., 2001; White et al., 2002). The Panola site experiences a subtropical climate, significantly warmer and more humid than Davis Run.

2.2.3. Río Icacos, Puerto Rico, USA

The Río Icacos catchment is located within the Luquillo Critical Zone Observatory (LCZO) in northeastern Puerto Rico. The local bedrock is the Río Blanco Quartz Diorite formation, formed during the Eocene (Seiders, 1971). Despite its name, the bedrock is now classified as a tonalite, and is notably lacking in K-feldspar relative to the other granitic profiles (Buss et al., 2017). The primary plagioclase minerals have similar quantities of Na and Ca, although are slightly more Na rich, and are of similar composition to andesine (Buss et al., 2008). The Río Icacos catchment has one of the highest granitic chemical weathering rates in the world (43-58 m Myr^{-1}) (White et al., 1998; Chabaux et al., 2013). The region experiences a humid tropical climate, with strong altitudinal variations in annual precipitation, and year-round warm temperatures (McDowell and Asbury, 1994; Table 1). Puerto Rico is regularly affected by tropical cyclones, and major hurricanes hit the region every few decades. Recent examples include Hurricane Hugo in 1989 and Hurricane Maria in 2017 (Shuckburgh et al., 2017). Río Icacos is the warmest of the four sites, and the site is substantially more humid than the next most humid site, Panola.

2.3. Sample Collection and Analysis

In 2012, continuous cores were drilled in three Slavkov Forest catchments as part of the Soil Transformations in European Catchments (SoilTrEC) Critical Zone Observatory project (Banwart et al., 2017). The drilling program, led by the Czech Geological Survey (Štědrá et al., 2015), recovered a 30.3 m core from Lysina (LY-V1; Štědrá et al., 2016). The Lysina core has been used to quantify bedrock solute contributions to streamwater chemistry and was

the focus of a mineralogical study of the Lysina granite (Štědrá et al., 2016; Krám et al., 2017). Štědrá et al. (2016) documented three facies in the Lysina bedrock core: quartz monzonite in the upper ~20 m, leucogranite below about 28 m, and alkali-feldspar granite in between. Sericitization and hematitization was observed throughout the upper 28 m, but evidence of hydrothermal alteration was most intense in the alkali-feldspar granite zone, where hematite caused a distinct pinkish discoloration of the core and clumps of secondary fluorite and carbonate were observed in association with feldspar and topaz.

For the present study, nine additional samples were taken from the Lysina core. One sample is a rock from the regolith at 1.85 m depth; the other eight samples were taken from zones of fractured rock below the rock-regolith interface (approximately 2.6 m depth), in contrast to previous samples (e.g., Štědrá et al., 2016) which were taken from zones of un-fractured, visibly pristine rock. Each sample was split in two, with one half prepared as a thin section and the other half pulverized and sieved (<63 µm) for geochemical analysis using a jaw crusher and ball mill. All equipment was cleaned with ethanol between samples. The milled powder was analysed by SGS Mineral Services, Ontario by ICP-OES after Li metaborate fusion digestion (major and some minor elements), ICP-MS after multi-acid digestion (for minor and trace elements), and titration for FeO. Uncertainties based upon the analytical detection limits, were propagated through all calculations. These data were combined with geochemical data from Nwaogu (2014) and Štědrá et al. (2016) (Table 2) to produce mass transfer profiles and a 30.15 m profile of weathering intensity.

Thin sections were prepared by Spectrum Petrographics (Vancouver, WA, USA). Thin sections were carbon coated and analysed by SEM (Hitachi S-3500N) in backscattered electron (BSE) mode with energy dispersive spectrometry (EDS, Thermo Scientific 10 mm^2 Silicon Drift Detector). Mineral identification and abundance were determined from EDS data of nine 0.86 x 0.86 mm squares on each thin section. Minerals were identified by EDS phase analysis using NSS 3.0 software, which was also used to measure mineral grain sizes for volumetric mineral surface area calculations. Mineral volumes from EDS analysis were converted to weight % values to allow for estimations of bulk-density using mineral density values from the literature (Deer et al., 2013). Images were obtained at a resolution of 1024 x 1024 pixels with an acquisition time of 4500 seconds per frame and a dwell time of 1 µs per pixel. Porosity values were also determined by EDS phase analysis.

2.4. Weathering calculations

Weathering intensity was assessed using the mass transfer coefficient (τ) (Brimhall and Dietrich, 1987) and the chemical index of alteration (CIA) (Nesbitt and Young, 1982). The mass transfer coefficient represents changes in the relative concentration of elements or minerals considered mobile during weathering, such as Ca or anorthite, normalized to a relatively immobile element or mineral, such as Ti or quartz (Brimhall and Dietrich, 1987; Anderson et al., 2002). These mass changes are normalized to concentrations in the parent material:

$$\tau = \left(\frac{C_{j,w}}{C_{j,p}}\frac{C_{i,p}}{C_{i,w}}\right) - 1 \quad \textbf{(1)}$$

Where C is concentration of the mobile, j, or immobile, i, component of interest in the weathered, w, or parent, p, material. The equation is such that τ = 0 if no change in concentration relative to the parent material has occurred (i.e., the component is immobile), τ = -1 indicates total depletion of the mobile component, and a τ value > 0 indicates enrichment of the mobile component relative to the parent material.

Immobile elements can become mobilized under certain conditions such as high acidity (Hodson, 2002). Volumetric strain (Eq. 2) was used to provide an indicator of element immobility (values should be near-zero for an immobile element in an isovolumetric weathering profile (Chadwick et al., 1990).

$$\varepsilon_{i,w} = \frac{\rho_p C_{i,p}}{\rho_w C_{i,w}} - 1 \quad \textbf{(2)}$$

Here, $\varepsilon_{i,w}$ is the volumetric strain in the weathered samples, ρ_p and ρ_w are the densities (g cm^{-3}) of the parent and weathered samples, respectively, while $C_{i,p}$ and $C_{i,w}$ are the concentrations of the immobile element in the parent and weathered samples. Sample densities were estimated from the phase analysis-derived mineral area percentages and mineral density values from the literature (Deer et al., 2013). Titanium was found to be relatively immobile in the Lysina profile (> -0.5 < 0.5) and thus was used as the immobile element for our mass transfer calculations.

The "freshness" of individual samples were assessed by calculating the CIA, which measures the degree of aluminosilicate weathering, independent of the parent material (Nesbitt and Young, 1982):

$$CIA = \left(\frac{Al_2O_3}{Al_2O_3 + CaO + K_2O + Na_2O}\right) * 100 \quad \textbf{(3)}$$

Equation 3 assumes that Al_2O_3 is immobile during weathering, such that a greater proportion of Al_2O_3 relative to the mobile oxides is considered to be indicative of weathering. A CIA value of 100 indicates total loss of the mobile oxides (Bahlburg and Dobrzinski, 2011). Values of CIA for unweathered aluminosilicate rocks vary depending on their composition; granites are typically in the 40-55 range. Note that CIA values were not corrected for apatite content.

The dimensionless mass transfer coefficient (Eq. 1) can be re-cast as a mass fraction (mol kg^{-1}) of element (or mineral) loss during weathering, C_w:

$$C_w = C_{j,p}\,(\tau_{i,j} + 1) \quad \textbf{(4)}$$

A weathering gradient is described by C_w with depth through a weathering profile, which was then used to calculate mineral-specific weathering rates (White, 2002):

$$R = 10^{-3}\,\frac{1}{\varphi\beta s}\,\frac{\omega}{b_s} \quad \textbf{(5)}$$

where R is the mineral-specific weathering rate in mol m^{-2} s^{-1}; φ is the mass fraction of the mineral in the weathering material (g g^{-1}); β is the mineral stoichiometry (mol element mol^{-1} mineral); s is the specific surface area of the mineral (m^2 g^{-1}); ω is the weathering advance rate of the profile (m s^{-1}); and b_s is the elemental weathering gradient (m kg mol^{-1}). In many cases, the total denudation rate (rate of surface lowering) is used as ω, where the profile is assumed to be in steady state, such that the surface lowering rate is equal to the weathering front advance rate (White, 2002; Phillips, 2010). Using total denudation as ω, where chemical weathering comprises a relatively small amount of the total surface lowering, may not be appropriate, as is believed to be the case for Lysina (Dannhaus et al., 2018). As such, using a whole-rock chemical weathering rate as ω may provide a more realistic estimate of weathering front advance rates where soil erosion and chemical weathering are not in steady state. Weathering rates were calculated for albite and K-

feldspar using mineral-specific gradients (Eq. 5). Whole-rock chemical weathering rates (ω) from Dannhaus et al. (2018) were used. Gradients were calculated between 14.64 m and the shallowest sample, across zones where mass transfer profiles revealed trends in mass loss and to avoid lithological differences in samples below 14.64 m (Štědrá et al., 2016). Mineral abundance data in Štědrá et al. (2016) excluded porosity and secondary clays, and primary minerals were normalized to 100 %. As such, they are not compatible with the mineral abundance dataset in this study.

Geometric surface areas of minerals were calculated (White and Peterson, 1990):

$$s = \frac{6\lambda}{\rho_m D} \quad \textbf{(6)}$$

where s is the specific surface area of a mineral ($m^2\ g^{-1}$), 6 is the geometric grain size parameter (6 indicates cubic geometry); the roughness factor, λ (100 for Li-mica and 7 for all other silicate minerals) (White and Brantley, 2003); the mineral density ρ_m (g cm^{-3}), and D, the mineral diameter (µm) (White and Peterson, 1990). The accuracy of the measuring tool in NSS 3.0 was assessed using 100 measurements of the 500 µm scale bar, indicating a tendency to under-measure the scale bar with an average error of 0.2% (mean measurement value = 499 µm, range = 481-507 µm) (Moore et al., 2019). Mineral diameters for specific minerals were calculated as the average between the square root of the long and short axes where mineral grains had an elongated shape. The number of mineral grains measured varied depending on mineral abundance and grain size within the samples; 15-45 grains of each mineral were measured in samples with large grain sizes, and 50-200 grains in samples with smaller grain sizes. Clay minerals were too small to accurately resolve individual grains. Uncertainty values for average mineral diameters within samples were estimated using standard error.

3. Results

3.1. Lysina mineralogy

Phase analysis of the Lysina core samples indicate the primary minerals are quartz, K-feldspar, and albite (defined here as $An_{0\text{-}10}$ $Ab_{90\text{-}110}$), with some variation in their relative abundances through the core (Table 3). Albite abundance decreases significantly from 2.77 to 1.85 m depth, across the rock-regolith interface (Table 3). No Ca-rich plagioclase phases were identified, in contrast to previous studies on fresher samples which found small quantities (<1 % normalised volume) of Ca plagioclase (Štědrá et al., 2016). Much of the Ca concentration within our rock samples appears to be associated with apatite, which comprises < 1 vol % of the Lysina bedrock (Table 3). A Mg-poor, but Li-rich, mica is also relatively abundant within the core (5-10 vol %). Within deeper sections of the core (> 20 m), mineral grain sizes are relatively large, with some exceeding 1 mm in size (Table 4). Previous studies of the core suggest Li-rich micas are relatively abundant (Navrátil, 2000; Štědrá et al., 2016), however the EDS detector used in this study is not capable of identifying elements lighter than Be. Overall, the Lysina granite is Mg-poor (< 0.6 wt %), although Li (measured using ICP-MS) is relatively abundant (0.1-0.2 wt %, Table 2). The stoichiometric ratios (excluding Li) of the mica were most similar to a Li-rich mica called zinnwaldite (Deer et al., 2013), the type locality (Zinnwald, Cínovec) of which is located in the neighboring mountain range (Ore Mountains), on the German/Czech border, 110 km NE from Lysina. Zinnwaldite and other Li-micas have been previously identified in the Lysina granite, and no other Li-bearing minerals were identified (Navrátil, 2000; Štědrá et al., 2016). Other studies identified multiple mica phases, including biotite and muscovite, based on optical and luminescence petrography (Nwaogu, 2014; Štědrá et al., 2016); however, the stoichiometric ratios indicated by EDS phase analyses of micas in this study did not match those of biotite or muscovite due to low Mg and high Fe content, respectively.

SEM analyses of thin sections show secondary clays within all samples (Table 3). These clays appear at the edges of fractures, particularly in samples deeper than 20 m. In the thin section from the deepest sample (28.75 m), secondary clays have an abundance of 12.5 vol % comprised mainly of kaolinite, with some illite. Below 20 m in the core, secondary clay volumes reach their highest value of 20.9 % at 20.22 m depth. Within the core as a whole, the highest secondary clay content (24.2 vol %) is observed in the shallowest sample (1.85 m). Although CIA values in the centre of the core (7.1 m – 14.64 m) are near or within the

upper range of "fresh" granites, the central part of the core still shows ~10 vol % of secondary clays.

Nearly all minerals within the core show some degree of alteration to secondary clays or porosity development in SEM images. Weathering appears to be most pronounced in the albites, with significant porosity development and alteration to secondary clays. The highest secondary clay volumes are associated with significantly reduced albite volumes, relative to the rest of the core. EDS phase analysis indicates clays within the mica pore spaces (Fig. 2A). Weathering of K-feldspar is also evident, but to a lesser degree than albite. Fluorite occupies apparent pore spaces within weathered albites at 20.22 and 23.68 m (Fig. 2B). Small quantities of Fe-oxides (<5 vol%) exist within these samples, which also occupy apparent pore spaces within weathered minerals.

Albite surface areas averaged 0.027 $m^2 g^{-1}$ in the parent sample, while K-feldspar and the Li-mica had larger average surface areas at 0.040 $m^2 g^{-1}$ and 0.53 $m^2 g^{-1}$, respectively. Clay mineral surface areas were not determined as individual grains were too small to accurately measure. Our surface area values are consistent with those from the literature with similar mean grain sizes (Bandstra et al., 2008). Mineral surface areas increase from 14.64 m towards the surface, especially from 4.3 m upwards, where albite, and to a lesser degree, K-feldspar, surface areas increase substantially (Fig. 3).

3.2. Lysina Weathering Parameters

The strongest depletion in the Lysina profile is exhibited by Ca (τ = -0.94 at the shallowest sample) and displays a clear depletion trend with two primary zones of depletion (14.64-12.6 m and 2.77-1.85 m, respectively; Fig. 4A). There is a notable steepening of the weathering gradient between 2.77 m and 1.85 m depth, which covers the zone where bedrock transitions to disaggregated regolith. Sodium and K also show a depletion trend through the profile (Fig. 4B and D). Lithium shows a general depletion trend above 5 m, but is slightly enriched between 14.64 m and about 7 m, (Fig. 4C).

The CIA profile (Fig. 5) shows a bimodal weathering pattern, with the highest values occurring at 1.85 m (CIA = 64.4) and 22.35 m (CIA = 62.4); lowest values occur at the base of

the core (CIA = 54.9) and between about 7 and 15 m (CIA = ~56). Such values are generally higher than those expected for fresh granites and granodiorites (CIA = 40-55; Bahlburg and Dobrzinski, 2011). From 7 m towards the surface CIA values increase, whereas below about 24 m CIA is variable (Fig. 4).

Bulk density values show no obvious trend within the core (Table 3). Similar rock densities are observed in the deepest and shallowest samples (2.52 g cm^{-3} and 2.53 g cm^{-3}, respectively). The highest density (2.72 g cm^{-3}) occurs at 23.68 m depth, and the lowest density occurs at 4.3 m (2.47 g cm^{-3}).

Elemental mass losses (C_w) at Lysina are minimal in most of the bedrock, although elemental mass loss (Eq. 4) increases in the shallower samples (< 4.3 m; Fig. 4 and 6). Weathering rates calculated using Equation 5, are fastest for albite (9.3 x 10^{-17} mol m^2 s^{-1}), while K-feldspar weathers somewhat slower (5.7 x 10^{-17} mol m^2 s^{-1})(Table 5).

3.3. Weathering mass transfer at additional sites

3.3.1. Davis Run

Weathering in the Davis Run profile extends down to approximately 22 m, with much of this weathering occurring at depth (Pavich, 1989). CIA values show the greatest change from 22 to 11 m depth (CIA = 53.6 and 81.6, respectively), coincident with a zone of Na and Ca loss (Fig. 7C, 8B and F). The profile becomes mostly depleted in Ca (Fig. 8B) and Na (Fig. 8F) by 11 m depth, while K (Fig. 9B) and Mg (Fig. 9F) show more gradual mass loss. Potassium and magnesium depletion profiles become sharper from 11 m towards the surface, with an increase in Mg loss above 5 m.

3.3.2. Panola

The Panola profile is weathered to 11 m, with Ca and Na approaching total depletion around 8 and 4.5 m, respectively (White et al., 2001; Fig.7D,8C and G, 9C and G). Potassium and Mg show little evidence of mass loss below 4.8 m, and the Mg gradient is steeper relative to K between 4.8 m and the surface (Fig. 9C and G). CIA values show steady depletion from fresh values of 50 at 11 m to values of 84 near the surface (Fig. 7D). An apparent decrease in CIA

values near the surface may be caused by loss of Al, as mass transfer profiles show no evidence of base metal enrichment near the surface (Fig. 8C and G, 9C and G).

3.3.3. Río Icacos

Weathering depths within the Río Icacos catchment varies from site to site, but transitions from fresh to near totally depleted material generally occur over a distance of 1 m or less (Buss et al., 2008; Orlando et al., 2016). The profile assessed here reaches fresh bedrock at approximately 7 m, although other cores have much deeper (>25 m) profiles with mostly fresh, spheroidally weathering corestones embedded in highly weathered regolith (Buss et al., 2008; Orlando et al., 2016). Calcium and sodium show near total depletion between 5.2 and 4.6 m depth (Fig. 8D and H). Significant loss of Mg also occurs over this zone but does not reach total depletion ($\tau \approx -0.8$; Fig. 9D). Potassium remains slightly enriched relative to the bedrock through much of the profile, likely due to mineral heterogeneity in the parent sample (Fig. 9H). The Río Icacos bedrock contains little to no K-Feldspar and thus K is a relatively minor component of the bedrock chemistry, compared to the other sites in this study. Nonetheless, K mass transfer values decrease between 5.2 and 4.6 m. Chemical Index of Alteration values reflect the rapid loss of Ca and Na, with a rapid transition from fresh values to near totally weathered values (~95) (Fig. 7F).

4. Discussion

The depth and thickness of weathering fronts affect numerous critical zone characteristics such as water flow paths (e.g., Schaffhauser et al., 2014; Orlando et al., 2016), subsurface microbial communities (e.g., Buss et al., 2005), stream solute sources (e.g., Calmels et al., 2011) and isotope fractionation mechanisms (e.g., Schaffhauser et al., 2014; Chapela Lara et al., 2017). Granitic weathering front depth and thickness, as well as weathering intensity and rates, vary significantly around the globe, but the controls that produce these variations are not well understood. Below we interpret the weathering front characteristics from the new Lysina weathering profile and then compare them to deep granitic weathering profiles from a range of precipitation and temperature regimes to assess the effects of these climate variables on weathering profiles. We further assess the roles of lithology (plagioclase composition), erosion, and subsurface architecture (i.e., variations in primary and secondary porosity and permeability with depth) on the resulting weathering front morphologies and chemical weathering rates.

4.1. Weathering and alteration processes within the Lysina profile

The dominant weathering reactions, as well as the initial weathering reactions, govern the development of a weathering profile (e.g., Buss et al., 2008; Goodfellow et al., 2016), and such reactions vary from site to site. The dominant weathering reaction in the Lysina profile is the dissolution of albite. In contrast, K-feldspar exhibits relatively limited alteration to secondary clays and remains relatively stable in abundance below 6.17 m depth, whereas Li-micas increase in abundance towards the surface, despite a gradual depletion trend in Li above 6 m depth (Table 3; Fig. 4C). SEM analysis of quartz grains reveal little evidence of weathering, and quartz exhibits no appreciable decrease in abundance towards the surface (Table 3).

Albite dissolution appears to precede the weathering of other minerals in the Lysina profile. Albite crystals show evidence of alteration to secondary clays in the deepest samples of the profile (below 25 m), whereas other minerals (e.g., K-feldspar and Li-micas) show comparatively little evidence of alteration. As such, the dissolution of albite is likely the first weathering reaction to occur and is the primary mechanism of secondary porosity development in the Lysina profile. In contrast, dissolution or oxidation of relatively minor minerals (calcite and biotite, respectively) are the initial weathering reactions in Panola and Río Icacos, respectively (e.g., White et al., 2001; Buss et al., 2008).

An episode of hydrothermal alteration within the Lysina profile likely occurred after the onset of albite weathering. In general, weathering profiles result from the interaction of weatherable minerals with meteoric water in the critical zone and hydrothermal alteration is not typically considered to be part of this process (e.g., Giardino and Houser, 2015). The Lysina core is altered to at least 30 m and possibly beyond the depth of the core, as evidenced by secondary clay abundances throughout the core and similar observations of a previous petrographic study (Table 3; Štědrá et al., 2016). However, weathering and hydrothermal alteration cannot be easily assessed independently in a quantitative way (e.g., Eq. 1-4) below about 20 m depth. The concentrations of fluorite and Fe-oxides within pore spaces between 25 and 20 m depth are interpreted as evidence of hydrothermal alteration that occurred after initial weathering, consistent with the observations of Štědrá et al. (2016). Fluorite was not observed in other sections of the core. Furthermore, fluorite grains are restricted to pore spaces within or associated with albite and do not occur in association

with less weathered minerals like quartz and K-feldspar, consistent with formation after the onset of weathering. The hydrothermally altered zone also coincides with a band of higher CIA values, while CIA and mass transfer values between 6.17 m and 14.64 m are relatively consistent (Fig. 4 and 5). The regolith layer (above 2.6 m depth) is more intensely weathered than the bedrock as evidenced by higher CIA values and secondary clay volumes in addition to lower primary mineral volumes. Weathering in the regolith layer is likely enhanced by the acidic porewaters (pH = 3.5-4.6). Much of the mineral mass loss occurs within the upper 3-4 m of the profile, although only a thin layer of soil and regolith exists (2-3 m). Despite the presence of hydrothermal overprinting below 20 m, the profile above 15 m is sufficient to assess weathering processes within the Lysina profile, including calculation of mineral weathering rates and correlating weathering front characteristics with climate parameters.

4.2. Weathering fronts in different climate regimes

Sites from around the world exhibit significantly different weathering profiles, both in depth and the intensity of weathering (CIA) (Fig. 7). Lysina has limited weathering over 10s of metres of bedrock under a thin (2.6 m) regolith, whereas the Río Icacos profile has a dramatic transition from fresh to near totally weathered regolith over only 1 m below a 5 m thick regolith. Although higher elevation weathering profiles in the Río Icacos catchment can have thicker regolith (> 25 m), the embedded bedrock corestones have similarly sharp transitions from un-weathered rock to highly depleted regolith (Orlando et al., 2016), reflecting rapid weathering (e.g., White et al., 1998; Buss et al., 2008). Davis Run and Panola represent intermediate profiles, with more gradual but deeper weathering at Davis Run and a shallower but sharper transition from fresh to weathered material at Panola. Thus, the weathering gradients become thinner (sharper) with increasing MAP and MAT (Fig. 7).

Globally, weathering intensity correlates well with climatic factors, with intense weathering commonly found in warm, humid environments (Strakhov, 1967; Goldberg and Humayun, 2010). Weathering profiles on a given lithology, in warmer, more humid environments also transition from fresh to weathered material over shorter distances, while these transitions in the cooler and drier environments are more gradual (e.g., White et al., 2001; Hewawasam et al., 2013; Schaffhauser et al., 2014; Buss et al., 2017). Conversely, fresh bedrock is reached at shallower depths at sites where weathering is more intense, regardless of the regolith thickness (Fig. 7).

Variations in bedrock porosity and permeability can also determine weathering profile morphology. A more permeable bedrock would expose greater volumes of minerals to reactive fluids. The permeability of the Panola bedrock is lower than that of Davis Run, which exhibits less intense, but deeper weathering (Table 1; White et al., 2001). The greater permeability at Davis Run relative to Panola (hydraulic conductivity is > 4 x 10^{-3} m yr^{-1} and 1 x 10^{-3} m yr^{-1}, respectively) may allow weathering to penetrate further into the bedrock (White et al., 2001). Similarly, the Río Icacos bedrock has low permeability (primary porosity < 0.03 %; Buss et al., 2008), with secondary porosity generated largely through reaction-driven fracturing (Fletcher et al., 2006), followed by dissolution and micro-cracking (Buss et al., 2008). Advective flow of reactive fluids through fractures promotes rapid weathering at Río Icacos, where regolith is deeper where the bedrock is more fractured (Orlando et al., 2016; Hynek et al., 2017).

Comparisons between the profiles above strongly indicate that weathering fronts become sharper within warmer and more humid climates, with the weathering front in the Río Icacos transitioning from fresh to near-totally weathered material over a distance of 1 m. The parameters affecting weathering processes within this transition zone are thus critical for understanding controls on weathering and its long-term impact on global climate. Below we further assess the parameters affecting weathering to determine the extent to which individual parameters determine weathering rates and profile morphology.

4.3. Controls on weathering rates in different climate regimes

4.3.1. Plagioclase Composition

Plagioclase weathering rates are available for four of the profiles: Lysina, Davis Run, Panola, and Río Icacos (in order of increasing MAT and MAP; Tables 1 and 5; White et al., 2001; White et al., 2002; Buss et al., 2008). In all four profiles, plagioclase weathers faster than K-feldspar or micas, with plagioclase rates ranging from log R = -16.4 mol m^{-2} s^{-1} at Davis Run to -13.0 in the Río Icacos profile (Eq. 5; Table 5). The plagioclase of both Lysina and Davis Run is predominately albite, whereas the Panola and Río Icacos plagioclases contain more

Ca: An_{23} and An_{48}, respectively (White et al., 2001; Buss et al., 2008). Ca-rich plagioclase is typically more reactive than Na-rich plagioclase (e.g., Bandstra et al., 2008). Lysina has significantly higher plagioclase weathering rates (log R = -16.1 mol m^{-2} s^{-1}) than Davis Run (log R = -16.4 m^{-2} s^{-1}), despite mean annual temperatures that are 5 ^{o}C warmer at Davis Run. MAP values are similar between the two sites, with less than 10% difference. Plagioclase weathering rates are slightly faster at Panola (Log R = -15.7 mol m^{-2} s^{-1}) than Lysina, but more than 2 orders of magnitude slower than at Río Icacos (Log R = -13.0 mol m^{-2} s^{-1}). MAT differs by 5 ^{o}C between Panola and Río Icacos (17 ^{o}C and 22 ^{o}C, respectively), and between Lysina and Davis Run (5 ^{o}C and 10 ^{o}C, respectively), but weathering rates differ significantly between the two warmer sites (1.4 – 2.7 orders of magnitude), and comparatively little at the two cooler sites (< 1 order of magnitude). Within this dataset, precipitation appears to have a strong influence on plagioclase weathering rates, while the influence of temperature appears to be weaker (Fig. 10A).

Although differences in composition will have some impact on plagioclase weathering rates, it is unlikely that they explain the scale of the differences in rates seen between the four sites. A comparison of laboratory-derived rates reveals only around 1 order of magnitude difference in weathering rates between albite and andesine (Bandstra et al., 2008). Furthermore, recent studies have indicated that differences in mineral stoichiometry may have less impact on weathering rates than previously thought; a study covering a range of plagioclase compositions (An_{21} – An_{50}) found differences of only a tenth of an order of magnitude in dissolution rates (White et al., 2017). As such, it is unlikely that the variations in plagioclase compositions significantly influence the differences in weathering rates seen in our dataset and suggests that other factors such as tectonic and climatic influences must be considered.

4.3.2. Erosion and Tectonics

A number of studies have argued that erosion (and thus tectonic activity) is a strong control on weathering rates (e.g., Berner et al., 1983; Raymo and Ruddiman, 1992; Riebe et al., 2001; Dixon and von Blanckenburg, 2012). Erosion can promote weathering by exposing fresh mineral surfaces and reducing soil and regolith accumulation, whereas the accumulation of thick weathered regolith can reduce the exposure of weatherable mineral surfaces to reactive fluids. Ratios of $^{10}Be/^{9}Be$ indicate that Lysina experiences approximately

63 m Myr^{-1} of erosion, accounting for approximately 90% of the total denudation (Dannhaus et al., 2018). Similarly, high erosion rates (20-100 m Myr^{-1}) have been observed at several other highland catchments in Europe, although the causes of these high rates remain unclear (Schaller et al., 2001). Low surface erosion rates likely account for the thicker regolith at Davis Run and Panola (11 m and 5 m, respectively) relative to Lysina and Río Icacos (2.6 m and 5 m, respectively; Table 1; Bacon et al., 2012; Brantley et al., 2017). Erosion in Río Icacos is dominated by landslides along slopes, but the regolith-mantled ridgetops are remarkably stable (Larsen and Torres-Sanchez, 1998; Brocard et al., 2015). Ridgetop weathering profiles in Río Icacos are believed to be in steady state (erosion rates = weathering rates, with regolith thickness stable through time), and an erosion rate of ~43 m Myr^{-1} have been derived using both ^{10}Be and U/Th methods (Brown et al., 1995; Chabaux et al., 2013). This rate is considerably higher than erosion rates at Davis Run and Panola (4.5-13 m Myr^{-1} at both sites) (Pavich, 1985; Brantley et al., 2017).

Crucially, although Río Icacos and Lysina experience a similar long-term average rate of erosion (43 m Myr^{-1} and 63 m Myr^{-1}, respectively), plagioclase weathering rates at Río Icacos are nearly three orders of magnitude higher than those at Lysina (Tables 1 and 5). It is possible that chemical weathering responses to erosion are site specific, as indicated by other studies (Ferrier and West, 2017). Thinner regolith may promote more rapid chemical weathering by allowing greater quantities of reactive fluids to make contact with minerals in the bedrock (Fletcher et al., 2006; Gabet and Mudd, 2009). Such a process may explain why plagioclase weathering rates are faster at Lysina than Davis Run, despite a cooler and slightly drier climate. Lysina's relatively thin regolith layer (2-3 m) contrasts with the deeper regolith of Davis Run (11 m), and albite mass loss increases significantly above Lysina's regolith-bedrock boundary (Table 3). There is no clear trend of faster mineral weathering rates at sites with higher erosion rates in this limited dataset (Fig. 10C). Regolith depth does appear to have a relationship with erosion rates, however, especially when considering the larger dataset of sites (Table 1), with the thinnest regolith generally found at the sites with the highest erosion rates (Fig. 11).

Although mineral specific weathering rates exhibit only a limited response to higher erosion rates, whole-rock chemical weathering rates (CWR) from other sites could be used to argue for a stronger erosional influence. The humid tropical sites of Nsimi in Cameroon, and

Hakgala in Sri Lanka, both experience low CWR, despite high precipitation and warm MAT (Table 1). In the case of Hakgala, the low CWR is attributed to the very low erosion rate, leading to a low supply rate of fresh material to the weathering environment (Hewawasam et al., 2013). At the humid site of Nsimi, deep (38 m), highly weathered regolith has been produced, likely as a result of the low erosion rate (Braun et al., 2005; Braun et al., 2012). In contrast, the arid site of Curacavi in Chile experiences comparable erosion rates (40.5 m Myr^{-1}) to Lysina and Río Icacos, but exhibits only limited weathering (Table 1; Vázquez et al., 2016). As such, data from the sites presented here show no clear trend between erosion and CWR, in contrast to results from previous studies (Riebe et al., 2004; West et al., 2005). However, Río Icacos, which has the highest CWR of our sites, has both a high erosion rate and high MAP (Table 1). Therefore, erosion rates may exert a significant control on CWR in environments where other variables, such as precipitation, do not restrict weathering. This effect is consistent with observations from previous compilations (West et al., 2005) and modeling studies that suggest that erosion is a control on weathering *regimes* (Lebedeva et al., 2010), where the balance between erosion and water infiltration determines whether a profile is "transport limited" or "weathering limited".

4.3.3. Climate and the Subsurface

In the absence of strong lithological and erosional controls on chemical weathering rates, climatic differences likely explain much of the variation in mineral and whole-rock weathering rates amongst the four key sites studied here (Tables 1 and 5). A relationship between climate and chemical weathering has been long established (Strakhov, 1967), although debate continues as to the relative influences of temperature and precipitation (e.g., White et al., 1999; Maher, 2010; Ibarra et al., 2016). The sharpness of weathering fronts (weathering gradients) in granitic profiles shows a strong correlation with MAP and a weak correlation with MAT (r^2 = 0.86 and 0.29, respectively). Figure 12 shows the Na weathering gradients (as a proxy for plagioclase weathering) of the sites (Table 1) plotted against MAT and MAP. The strong correlation between the Na gradient and MAP indicates that as MAP increases, Na becomes depleted in profiles over smaller distances, thus leading

to sharper weathering fronts. These results are in line with those indicated by correlations between plagioclase weathering rates and climate variables (Fig. 10), as well as correlations between climate variables and whole-rock chemical weathering rates , both of which have a strong correlation with MAP (Fig. 14; Oliva et al., 2003; Maher, 2010; Ibarra et al., 2016). The Na gradient appears to be only weakly influenced by MAT, while erosion has essentially no impact on Na gradient values (Fig.12C). The similarity of the response of Na gradients, CWR, and plagioclase weathering rates to MAP suggests that water fluxes to the profile determines both the sharpness of the weathering front and whole-rock chemical weathering rates.

In environments where both precipitation and infiltration rates are high (i.e., high effective precipitation), groundwater residence times are shorter and weathering products are more easily removed from the profile, thus lowering the geochemical saturation state of the groundwater, with respect to weatherable minerals, and favoring faster mineral weathering rates. The link between groundwater geochemical saturation states and fluid residence times within weathering profiles, has been proposed as a strong control on weathering rates (Maher, 2010). In cases where high effective precipitation keeps pore water thermodynamically undersaturated, effective precipitation would be the dominant control on chemical weathering rates and weathering gradients, with high weathering rates causing rapid depletion of minerals from the profile, resulting in sharper gradients. This scenario was demonstrated by reactive transport models that indicated that the highest plagioclase weathering rates were only achieved under high water flow rates and rapid fluid transit times, allowing groundwater to be further from equilibrium and permitting more rapid weathering reactions (Maher and Druhan, 2014). Similar observations have been made in studies of laboratory derived weathering rates, which are frequently 2-4 orders of magnitude more rapid than field derived rates (White and Brantley, 2003; Riebe et al., 2004). This difference in rates has been attributed to, in part, the far from equilibrium laboratory conditions in most experiments and the nearer to equilibrium conditions found in natural settings.

If water fluxes and fluid residence times are key controls on weathering gradients and rates, the structure of the subsurface and its impact on these factors must be considered. Greater secondary porosity should promote fluid transport through the regolith, increasing flow

rates and reducing residence times (Maher and Druhan, 2014). Furthermore, even slight weathering may still result in drastic changes in the secondary porosity of the bedrock, allowing new weathering pathways to be produced (St Clair et al., 2015; Goodfellow et al., 2016). Within the Lysina core, samples from fractured zones show slightly higher CIA values than those from less fractured zones (Fig.5; Štědrá et al., 2016). Fractured samples within this study typically display more evidence of weathering in the form of higher CIA values than samples from Štědrá et al. (2016) and greater secondary clay content than those with fewer fractures (Table 3). While these differences in weathering are very small, representing only a change in CIA values of 2-3, these remain outside the range of calculated uncertainty (Fig. 5). It is possible that fractures promote water movement in the Lysina core, leading to greater weathering in fractured zones. A more extreme version of this process may be occurring in the Río Icacos catchment. Much of the variation in regolith depth between profiles at Río Icacos has been attributed to differences in the extent of fracturing, with fractures allowing for more efficient transport of water and weathering products (Orlando et al., 2016).

Such examples highlight the potential impact of subsurface architecture on both weathering rates and weathering gradients, as well as the key role of secondary porosity development on exposing fresh minerals to reactive fluids. The dataset compiled here (Table 1) reveals a trend of weathering deep into the bedrock in cooler and drier environments such as Lysina and Davis Run, where weathering is sufficiently slow to allow fluids to penetrate the bedrock but insufficiently rapid to produce regolith. These slower weathering rates produce deep profiles with gentle transitions between fresh and highly weathered material over 10s of meters. In contrast, the bedrock in warm and humid environments such as Panola, Hakgala, and Río Icacos is largely un-weathered, with sharp weathering transitions between the bedrock and regolith over small distances (~1 m). Such sharp transitions may represent weathering “hotspots”, where chemical weathering occurs rapidly, producing thin weathering fronts (Buss et al., 2017) and high fluxes of inorganic nutrients and energy sources for subsurface biota (Buss et al., 2005; 2010).

Extensive, weathering-relevant datasets from deep critical zone boreholes are relatively few in number, and although compelling trends were identified in this study, conclusively determining the impact of subsurface architecture on weathering rates may not be possible

from field data alone. Recent advances in topographic stress modeling and geophysical analysis of the critical zone could, however, provide a way to predict catchment-scale subsurface architecture with fewer deep boreholes (Moon et al., 2017). Reactive transport models also provide a method of determining the impact of subsurface architecture, independent of climate conditions (e.g., Maher and Druhan, 2014).

Although higher erosion rates could promote more rapid chemical weathering rates within our dataset (as evidenced by the more rapid weathering at Lysina relative to Davis Run), comparison with additional sites and studies suggest the effects of erosion are highly site specific (Ferrier and West, 2017). Importantly, they do not appear to significantly increase weathering rates at sites where precipitation is limited, as evidenced by the high erosion/low precipitation site of Curacavi (Table 1, Fig. 9). However, where high erosion rates combine with warm and humid conditions (e.g., tectonically active tropical mountain belts or volcanic islands (e.g., Rad et al., 2007)), chemical weathering rates have the potential to be very high, as seen in Río Icacos. The steep slopes in mountainous environments may also promote more effective water transport, reducing fluid residence times (Maher, 2010).

Despite CWR and weathering front sharpness both being strongly influenced by MAP, CWRs may be decoupled from weathering front sharpness. While a sharp weathering front indicates that a profile becomes depleted in weatherable minerals over a short distance, the CWR of a profile will be primarily determined by the rate of weathering front advance. However, a front that advances slowly will result in low CWR in a profile. As such, a sharp weathering front in a profile where weathering advance rates are high will likely produce high CWR, but a sharp weathering front is not necessarily indicative of high CWR. The dependence of CWR on weathering advance rates likely explains the stronger erosion control on CWR (Fig. 13C) relative to weathering gradients (Fig. 12C).

Our analysis indicates that precipitation represents a primary environmental control on granitic weathering rates, presumably by increasing water fluxes and lowering geochemical saturation within weathering profiles. Similarly, the sharpness of weathering fronts are also likely determined by water fluxes and geochemical saturation states. Sharper weathering

fronts (fresh to highly weathered material over distances of a few meters or less) occur when the water in the profile is more understaturated with respect to weatherable minerals. Temperature appears to exert a minimal influence on most of the profiles within this study, although the impact of temperature may be amplified under more humid conditions (Oliva et al., 2003). These findings are consistent with West et al. (2005), who showed that chemical weathering rates correlate most strongly with mean annual runoff and had no significant correlation with temperature (Fig. 13), but extends those findings to the deep subsurface. The latitudinal trends in weathering profiles identified by Strakhov (1967) suggest that climate has a stronger influence on weathering front morphology than lithology or subsurface architecture (which is the result of the parent lithology and weathering). The effect of subsurface architecture on weathering fronts may be more signifcant at the local scale (profile to watershed) where variations in climate are more limited. However, the potential for subsurface architecture to affect weathering fronts lies in its control on water flow, thus, together, these parameters appear to be more important than temperature in establishing weathering fronts and rates.

5. Conclusions

We presented new geochemical analyses of a granitic weathering profile in a temperate forest, Lysina, from which we calculated mineral specific weathering rates and identified key weathering processes. We then compared the weathering intensities (CIA), mineral-specific weathering rates and weathering front morphology with additional granitic profiles from the literature from different climatic regimes to identify dominant weathering controls.

Lysina exhibits thin regolith overlying a weathered bedrock extending down at least 15 m and likely beyond 30 m, suggesting deep infiltration of meteoric water. SEM observations, EDS phase analyses, and mass loss calculations indicate that the fastest mineral to weather in the Lysina profile is albite (log R = -16.1 mol m^{-2} s^{-1}), while K-feldspar and Li-micas weather more slowly.

Comparison with three additional granitic profiles revealed a wide array of weathering front morphologies, ranging from 10s of metres of slightly weathered bedrock at Lysina to the sharp, ~ 1 m transition of fresh bedrock to highly weathered regolith at Río Icacos. Plagioclase weathering rates vary by over three orders of magnitude among these four sites,

with the most rapid rates occurring at the tropical Río Icacos and the slowest rates occurring at the temperate Davis Run catchment. In contrast to some earlier studies (e.g., White and Blum, 1995; White et al., 1999; Riebe et al., 2004), weathering rates in our dataset indicated a weaker association with temperature and erosion and a stronger association with precipitation. This relationship likely stems from the higher water fluxes and shorter water residence times within regolith in high-precipitation environments, allowing for lower geochemical saturation in the subsurface, which promotes faster weathering rates, consistent with Maher (2010). Comparison with additional sites suggested that precipitation is the primary limiting factor on whole-rock weathering rates (CWR), with erosion playing a secondary role. These limiting effects could be highly significant for weathering and climate interactions over geological time and indicate the potential importance of rapidly eroding sites in warm and humid environments on long-term atmospheric CO_2 concentrations. Such environments would then disproportionately contribute to the global drawdown of atmospheric CO_2 via the 'weathering thermostat'; by extension, the geographical distributions of such environments could control the efficacy of that thermostat.

The structure, or *architecture*, of the subsurface likely plays a key role in determining water flow rates and geochemical saturation states through weathering profiles. A high degree of variability in secondary porosity exists between sites, even amongst similar lithologies. High secondary porosity likely promotes high water fluxes and shorter residence times in the subsurface environment. These variations are difficult to predict at the watershed scale but can lead to significant differences in weathering profile morphology within individual catchments, especially in intense weathering environments. Structures that promote more rapid water flow, such as fractures, could result in weathering "hotspots", especially at depth. Furthermore, deep fractures may lead to decoupling between the weathering zone and the surface environment by allowing weathering reactions to occur further from the surface. Furthermore, the interplay of subsurface architecture and precipitation in controlling water flow and thus weathering rates means that the nature of precipitation is important, i.e., intense, episodic precipitation leads to high runoff and poor infiltration but high erosion. Additional field site data from more critical zone profiles and reactive transport modeling will allow us to better understand the impacts of episodic precipitation

and mechanisms of shallow and deep weathering processes on profile morphology and weathering rates on various spatial and time scales.

6. Acknowledgements

This work was supported by European Research Council under the European Union's Seventh Framework Programme (FP/2007-2013)/ERC Project "The Greenhouse Earth System" (T-GRES), Grant Agreement no. 340923. Drilling in the Slavkov Forest CZO was funded by the European Commission FP7 Collaborative Project "Soil Transformations in European Catchments" (SoilTrEC), Grant Agreement no. 244118. P. Krám was supported by the internal project 310010 of the Czech Geological Survey. We thank S. Kearns and B. Buse (University of Bristol) for SEM-EDS training and assistance. We also thank E. Mouchos (University of Bristol), M. Chapela Lara (University of New Hampshire), Veronika Štědrá and Tomáš Jarchovský (Czech Geological Survey) and Juraj Farkaš (University of Adelaide) for helpful discussions.

We also thank the editor and an anonymous reviewer for constructive comments.

References

Anderson, S.P., Dietrich, W.E., Brimhall, G.H., 2002. Weathering profiles, mass-balance analysis, and rates of solute loss: Linkages between weathering and erosion in a small, steep catchment. Geological Society of America Bulletin, 114: 1143-1158.

Bacon, A.R., Richter, D.d., Bierman, P.R., Rood, D.H., 2012. Coupling meteoric ^{10}Be with pedogenic losses of ^{9}Be to improve soil residence time estimates on an ancient North American interfluve. Geology, 40(9): 847-850.

Bahlburg, H., Dobrzinski, N., 2011. A review of the Chemical Index of Alteration (CIA) and its application to the study of Neoproterozoic glacial deposits and climate transitions. Geological Society, London, Memoirs, 36(1): 81-92.

Bandstra, J.Z., Buss, H.L., Campen, R.K., Liermann, L.J., Moore, J., Hausrath, E.M., Navarre-Sitchler, A.K., Jang, J.-H., Brantley, S.L., 2008. Appendix: Compilation of Mineral Dissolution Rates. In: Brantley, S.L., Kubicki, J.D., White, A.F. (Eds.), Kinetics of Water-Rock Interaction. Springer, New York, pp. 737-823.

Banwart, S. et al., 2017. Soil Functions in Earth's Critical Zone: Key Results and Conclusions. Advances in Agronomy, 142: 1-27.

Bazilevskaya, E., Lebedeva, M., Pavich, M., Rother, G., Parkinson, D.Y., Cole, D., Brantley, S.L., 2013. Where fast weathering creates thin regolith and slow weathering creates thick regolith. Earth Surface Processes and Landforms, 38(8): 847-858.

Behrens, R., Bouchez, J., Schuessler, J.A., Dultz, S., Hewawasam, T., von Blanckenburg, F., 2015. Mineralogical transformations set slow weathering rates in low-porosity metamorphic bedrock on mountain slopes in a tropical climate. Chemical Geology, 411: 283-298.

Berner, R.A., Lasaga, A.C., Garrels, R.M., 1983. The carbonate-silicate geochemical cycle and its effect on atmospheric carbon dioxide over the past 100 million years. American Journal of Science, 57: 641-683.

Blecha, V., Štemprok, M., 2012. Petrophysical and geochemical characteristics of late Variscan granites in the Karlovy Vary Massif (Czech Republic) - implications for gravity and magnetic interpretation in shallow depths. Journal of Geosciences, 57: 65-85.

Brantley, S.L., Lebedeva, M., Bazilevskaya, E., 2014. Relating Weathering Fronts for Acid Neutralization and Oxidation to pCO_2 and pO_2, Treatise on Geochemistry, pp. 327-352.

Brantley, S.L., Lebedeva, M.I., Balashov, V.N., Singha, K., Sullivan, P.L., Stinchcomb, G., 2017. Toward a conceptual model relating chemical reaction fronts to water flow paths in hills. Geomorphology, 277: 100-117.

Braun, J.J., Ngoupayou, J.R.N., Viers, J., Dupre, B., J.P., B.B., Boeglin, J.L., Robain, H., Nyeck, B., Freydier, R., Nkamdjou, L.S., Rouiller, J., Muller, J.P., 2005. Present weathering rates in a humid tropical watershed: Nsimi, South Cameroon. GCA, 69(2): 357-387.

Braun, J.J., Marechal, J.C., Riotte, J., Boeglin, J.L., Bedimo Bedimo, J.P., Ndam Ngoupayou, J.R., Nyeck, B., Robain, H., Sekhar, M., Audry, S., Viers, J., 2012. Elemental weathering fluxes and saprolite production rate in a Central African lateritic terrain (Nsimi, South Cameroon). GCA, 99: 243-270.

Brimhall, G., Dietrich, W.E., 1987. Constitutive mass balance relations between chemical composition, volume, density, porosity, and strain in metasomatic hydrochemical systems: results on weathering and pedogenisis. GCA, 51: 567-587.

Brocard, G.Y., Willenbring, J.K., Scatena, F.N., Johnson, A.H., 2015. Effects of a tectonically-triggered wave of incision on riverine exports and soil mineralogy in the Luquillo Mountains of Puerto Rico. Applied Geochemistry, 63: 586-598.

Brown, E.T., Stallard, R., Larsen, M.C., Raisbeck, G.M., Yiou, F., 1995. Denudation rates determined from the accumulation of in situ-produced ^{10}Be in the Luquillo Experimental Forest, Puerto Rico. Earth and Planetary Science Letters, 129: 193-202.

Buss, H.L., Bruns, M.A., Schultz, M.J., Mathur, C.F., Moore, J., Brantley, S.L., 2005. Microbial Fe cycling in deep regolith. GCA, 69(10): A225-A225.

Buss, H.L., Sak, P.B., Webb, S.M., Brantley, S.L., 2008. Weathering of the Rio Blanco quartz diorite, Luquillo Mountains, Puerto Rico: Coupling oxidation, dissolution, and fracturing. GCA, 72(18): 4488-4507.

Buss, H.L., Mathur, R., White, A.F., Brantley, S.L., 2010. Phosphorus and iron cycling in deep saprolite, Luquillo Mountains, Puerto Rico. Chemical Geology, 269: 52-61.

Buss, H.L., Chapela Lara, M., Moore, O.W., Kurtz, A.C., Schulz, M.S., White, A.F., 2017. Lithological influences on contemporary and long-term regolith weathering at the Luquillo Critical Zone Observatory. GCA, 196: 224-251.

Calmels, D., Galy, A., Hovius, N., Bickle, M., West, A.J., Chen, M.-C., Chapman, H., 2011. Contribution of deep groundwater to the weathering budget in a rapidly eroding mountain belt, Taiwan. Earth and Planetary Science Letters, 303: 48-58.

Chabaux, F., Blaes, E., Stille, P., di Chiara, R.R., Dosseto, A., Pelt, E., Ma, L., Buss, H.L., Brantley, S.L., 2013. Regolith formation rate from U-series nuclides: Implications from the study of a spheroidal weathering profile in the Rio Icacos watershed (Puerto Rico). GCA, 100: 73-95.

Chadwick, O.A., Brimhall, G.H., Hendricks, D.M., 1990. From black box to a grey box: a mass balance interpretation of pedogenesis. Geomorphology, 3: 369-390.

Chapela Lara, M., Buss, H.L., von Strandmann, P., Schuessler, J.A., Moore, O.W., 2017. The influence of critical zone processes on the Mg isotope budget in a tropical, highly weathered andesitic catchment. Geochimica Et Cosmochimica Acta, 202: 77-100.

Dannhaus, N., Wittmann, H., Krám, P., Christl, M., von Blanckenburg, F., 2018. Catchment-wide weathering and erosion rates of mafic, ultramafic, and granitic rock from cosmogenic meteoric $^{10}Be/^{9}Be$ ratios. GCA, 222: 618-641.

Deer, W.A., Howie, R.A., Zussman, J., 2013. An Introduction to the Rock-Forming Minerals. The Mineralogical Society, London, 498 pp.

Dixon, J.L., von Blanckenburg, F., 2012. Soils as pacemakers and limiters of global silicate weathering. Comptes Rendus Geoscience, 344(11-12): 597-609.

Drake, A.A., Jr, Froelich, A.J., 1986. Geologic Map of the Annandale Quadrangle, Fairfax and Arlington Counties, and Alexandria City, Virginia. U.S. Geological Survey.

Ferrier, K.L., West, N., 2017. Responses of chemical erosion rates to transient perturbations in physical erosion rates, and implications for relationships between chemical and physical erosion rates in regolith-mantled hillslopes. Earth and Planetary Science Letters, 474: 447-456.

Fletcher, R.C., Buss, H.L., Brantley, S.L., 2006. A spheroidal weathering model coupling porewater chemistry to soil thicknesses during steady-state denudation. Earth and Planetary Science Letters, 244(1-2): 444-457.

Frey, B., Rieder, S.R., Brunner, I., Plotze, M., Koetzsch, S., Lapanje, A., Brandl, H., Furrer, G., 2010. Weathering-associated bacteria from the Damma glacier forefield: physiological capabilities and impact on granite dissolution. Appl Environ Microbiol, 76(14): 4788-96.

Gabet, E.J., Mudd, S.M., 2009. A theoretical model coupling chemical weathering rates with denudation rates. Geology, 37(2): 151-154.

Giardino, J.R., Houser, C., 2015. Introduction to the Critical Zone. Developments in Earth Surface Processes, pp. 1-13.

Goldberg, K., Humayun, M., 2010. The applicability of the Chemical Index of Alteration as a paleoclimatic indicator: An example from the Permian of the Paraná Basin, Brazil. Palaeogeography, Palaeoclimatology, Palaeoecology, 293(1-2): 175-183.

Goodfellow, B.W., Hilley, G.E., Webb, S.M., Sklar, L.S., Moon, S., Olson, C.A., 2016. The chemical, mechanical, and hydrological evolution of weathering granitoid. Journal of Geophysical Research-Earth Surface, 121(8): 1410-1435.

Hewawasam, T., von Blanckenburg, F., Bouchez, J., Dixon, J.L., Schuessler, J.A., Maekeler, R., 2013. Slow advance of the weathering front during deep, supply-limited saprolite formation in the tropical Highlands of Sri Lanka. GCA, 118: 202-230.

Hodson, M.E., 2002. Experimental evidence for the mobility of Zr and other trace elements in soils. GCA, 66: 819-828.

Hruska, J., Moldan, F., Kram, P., 2002. Recovery from acidification in central Europe - observed and predicted changes of soil and streamwater chemistry in the Lysina. catchment, Czech Republic. Environmental Pollution, 120(2): 261-274.

Hynek, S., Comas, X., Brantley, S.L., 2017. The Effect of Fractures on Weathering of Igneous and Volcaniclastic Sedimentary Rocks in the Puerto Rican Tropical Rain Forest. Procedia Earth and Planetary Science, 17: 972-975.

Ibarra, D.E., Caves, J.K., Moon, S., Thomas, D.L., Hartmann, J., Chamberlain, C.P., Maher, K., 2016. Differential weathering of basaltic and granitic catchments from concentration–discharge relationships. GCA, 190: 265-293.

Isherwood, D., Street, A., 1976. Biotite-induced grussification of the Boulder Creek Granodiorite, Boulder County, Colorado. Geological Society of America Bulletin, 87: 366-370.

Jamtveit, B., Putnis, C., Malthe-Sorenssen, A., 2009. Reaction induced fracturing during replacement processes. Contributions to Mineralogy and Petrology, 157(1): 127-133.

Kopacek, J., Hejzlar, J., Kram, P., Oulehle, F., Posch, M., 2016. Effect of industrial dust on precipitation chemistry in the Czech Republic (Central Europe) from 1850 to 2013. Water Res, 103: 30-37.

Krám, P., Hruska, J., Wenner, B.S., Driscoll, C.T., Johnson, C.E., 1997. The biogeochemistry of basic cations in two forest catchments with contrasting lithology in the Czech Republic. Biogeochemistry, 37(2): 173-202.

Krám, P., Santore, R.C., Driscoll, C.T., Aber, J.D., Hruska, J., 1999. Application of the forest-soil-water model (PnET-BGC/CHESS) to the Lysina catchment, Czech Republic. Ecological Modelling, 120(1): 9-30.

Krám, P., Hruška, J., Shanley, J.B., 2012. Streamwater chemistry in three contrasting monolithologic Czech catchments. Applied Geochemistry, 27(9): 1854-1863.

Krám, P., Farkaš, J., Pereponova, A., Nwaogu, C., Štědrá, V., Hruška, J., 2014. Bedrock Weathering and Stream Water Chemistry in Felsic and Ultramafic Forest Catchments. Procedia Earth and Planetary Science, 10: 52-55.

Krám, P., Curik, J., Veselovsky, F., Myska, O., Hruska, J., Stedra, V., Jarchovsky, T., Buss, H.L., Chuman, T., 2017. Hydrochemical fluxes and bedrock chemistry in three contrasting catchments underlain by felsic, mafic and ultramafic rocks. Procedia Earth and Planetary Science, 17: 538-541.

Larsen, M.C., Torres-Sanchez, A.J., 1998. The frequency and distribution of recent landslides in three montane tropical regions of Puerto Rico. Geomorphology, 24(4): 309-331.

Lebedeva, M.I., Fletcher, R.C., Brantley, S.L., 2010. A mathematical model for steady-state regolith production at constant erosion rate. Earth Surface Processes and Landforms, 35: 508-524.

Maher, K., 2010. The dependence of chemical weathering rates on fluid residence time. Earth and Planetary Science Letters, 294(1-2): 101-110.

Maher, K., Druhan, J., 2014. Relationships between the Transit Time of Water and the Fluxes of Weathered Elements through the Critical Zone. Procedia Earth and Planetary Science, 10: 16-22.

McDowell, W.H., Asbury, C.E., 1994. Export of carbon, nitrogen, and major ions from three tropical montane watersheds. Limnology and Oceanography, 39(1): 111-125.

Melfi, A.J., Cerri, C.C., Kronberg, B.I., Fyfe, W.S., Mckinnon, B., 1983. Granitic Weathering - a Brazilian Study. Journal of Soil Science, 34(4): 841-851.

Moon, S., Perron, J.T., Martel, S.J., Holbrook, W.S., St. Clair, J., 2017. A model of three-dimensional topographic stresses with implications for bedrock fractures, surface processes, and landscape evolution. Journal of Geophysical Research: Earth Surface, 122(4): 823-846.

Moore, O., Buss, H., Dosseto, A., 2019. Incipient chemical weathering at bedrock fracture interfaces in a tropical critical zone, Puerto Rico. GCA, 252: 61-87.

Navarre-Sitchler, A., Steefel, C.I., Sak, P.B., Brantley, S.L., 2011. A reactive-transport model for weathering rind formation on basalt. GCA, 75(23): 7644-7667.

Navrátil, T., 2000. Beryllium in Waters of Czech Forested Ecosystems and the Release of Beryllium from Granites. GeoLines, 12: 18-40.

Nesbitt, H.W., Young, G.M., 1982. Early Proterozoic climates and plate motions inferred from major element chemistry of lutites. Nature, 199: 715-717.

Nwaogu, C., 2014. Mobility and biogeochemical cycling of base cations (Ca and Mg) during weathering processes in a sensitive forest ecosystem, Lysina, Slavkov Forest, Czech Republic. M.Sc. Thesis, Czech University of Life Sciences, Prague.

Oliva, P., Viers, J., Dupré, B., 2003. Chemical weathering in granitic environments. Chemical Geology, 202(3-4): 225-256.

Orlando, J., Comas, X., Hynek, S.A., Buss, H.L., Brantley, S.L., 2016. Architecture of the deep critical zone in the Rio Icacos watershed (Luquillo Critical Zone Observatory, Puerto Rico) inferred from drilling and ground penetrating radar (GPR). Earth Surface Processes and Landforms, 41(13): 1826-1840.

Pavich, M., 1985. ^{10}Be analysis of a Quaternary weathering profile in the Virginia Piedmont. Geology, 13: 39-41.

Pavich, M.J., 1989. Regolith residence time and the concept of surface age of the Piedmont peneplain. Geomorphology, 2(1-3): 181-196.
Phillips, J.D., 2010. The convenient fiction of steady-state soil thickness. Geoderma, 156(3-4): 389-398.
Pierson-Wickmann, A.C., Aquilina, L., Martin, C., Ruiz, L., Molénat, J., Jaffrézic, A., Gascuel-Odoux, C., 2009. High chemical weathering rates in first-order granitic catchments induced by agricultural stress. Chemical Geology, 265(3-4): 369-380.
Rad, S.D., Allegre, C.J., Louvat, P., 2007. Hidden erosion on volcanic islands. Earth and Planetary Science Letters, 262: 109-124.
Raymo, M.E., Ruddiman, W.F., 1992. Tectonic forcing of the late cenozoic climate. Nature, 359: 117-122.
Riebe, C.S., Kirchner, J.W., Granger, D.E., Finkel, R.C., 2001. Strong tectonic and weak climatic control of long-term chemical weathering rates. Geology, 29(6): 511-514.
Riebe, C.S., Kirchner, J.W., Finkel, R.C., 2004. Erosional and climatic effects on long-term chemical weathering rates in granitic landscapes spanning diverse climate regimes. Earth and Planetary Science Letters, 224: 547-562.
Riebe, C.S., Hahm, W.J., Brantley, S.L., 2017. Controls on deep critical zone architecture: a historical review and four testable hypotheses. Earth Surface Processes and Landforms, 42(1): 128-156.
Røyne, A., Jamtveit, B., Mathiesen, J., Malthe-Sørenssen, A., 2008. Controls on rock weathering rates by reaction-induced hierarchical fracturing. Earth and Planetary Science Letters, 275: 364-369.
Schaffhauser, T., Chabaux, F., Ambroise, B., Lucas, Y., Stille, P., Reuschlé, T., Perrone, T., Fritz, B., 2014. Geochemical and isotopic (U, Sr) tracing of water pathways in the granitic Ringelbach catchment (Vosges Mountains, France). Chemical Geology, 374-375: 117-127.
Schaller, M., von Blanckenburg, F., Hovius, N., Kubik, P.W., 2001. Large-scale erosion rates from in situ-produced cosmogenic nuclides in European river sediments. Earth and Planetary Science Letters, 188(3-4): 441-458.
Seiders, V.M., 1971. Geologic map of the El Yunque quadrangle, Puerto Rico. U.S. Geological Survey.
Shuckburgh, E., Mitchell, D., Stott, P., 2017. Hurricanes Harvey, Irma, and Maria: how natural were these 'natural disasters'? Weather, 72(11): 353-354.
St Clair, J., Moon, S., Holbrook, W.S., Perron, J.T., Riebe, C.S., Martel, S.J., Carr, B., Harman, C., Singha, K., Richter, D., 2015. Geophysical imaging reveals topographic stress control of bedrock weathering. Science, 350(6260): 534-8.
Štědrá, V., Krám, P., Farkaš, J., 2015. Petrology and whole-rock geochemistry of metabasites from borehole cores in the Na Zeleném and Pluhův Bor catchments in the Slavkov Forest, western Bohemia. Geoscience Research Reports for 2014: 103-108.
Štědrá, V., Jarchovský, T., Krám, P., 2016. Lithium-rich granite in the Lysina-V1 borehole in the southern part of the Slavkov Forest, western Bohemia. Geoscience Research Reports, 49: 137-142.
Strakhov, N.M., 1967. Principles of Lithogenesis. Consultants Bureau, New York.
Vázquez, M., Ramírez, S., Morata, D., Reich, M., Braun, J.-J., Carretier, S., 2016. Regolith production and chemical weathering of granitic rocks in central Chile. Chemical Geology, 446: 87-98.
Vylita, T., Žák, K., Cílek, V., Hercman, H., Mikšíková, L., 2007. Evolution of hot-spring travertine accumulation in Karlovy Vary/Carlsbad (Czech Republic) and its significance for the evolution of Teplá valley and Ohře/Eger rift. Zeitschrift für Geomorphologie, 51(4): 427-442.
West, A.J., Galy, A., Bickle, M., 2005. Tectonic and climatic controls on silicate weathering. Earth and Planetary Science Letters, 235: 211-228.
White, A.F., Peterson, M.L., 1990. Role of reactive surface area characterization in geochemical models. In: Melchior, D.C.a.B., R. L (Ed.), Chemical modeling of aqueous systems II. ACS Symp. Ser., pp. 461-475.

White, A.F., Blum, A., 1995. Effects of climate on chemical weathering in watersheds. GCA, 59(9): 1729-1747.
White, A.F., Blum, A.E., Schulz, M.S., Vivit, D.V., Stonestrom, D.A., Larsen, M., Murphy, S.F., Eberl, D., 1998. Chemical weathering in a tropical watershed, Luquillo Mountains, Puerto Rico: I. Long-term versus short-term weathering fluxes. GCA, 62(2): 209-226.
White, A.F., Blum, A.E., Bullen, T.D., Vivit, D.V., Schulz, M., Fitzpatrick, J., 1999. The effect of temperature on experimental and natural weathering rates of granitoid rocks. GCA, 63(19-20): 3277-3291.
White, A.F., Bullen, T.D., Schulz, M.S., Blum, A.E., Huntington, T.G., Peters, N.E., 2001. Differential rates of feldspar weathering in granitic regoliths. GCA, 65: 847-869.
White, A.F., 2002. Determining mineral weathering rates based on solid and soute weathering gradients and velocities: application to biotite weathering in saprolites. Chemical Geology, 190: 69-89.
White, A.F., Blum, A.E., Schulz, M.S., Huntington, T.G., Peters, N.E., Stonestrom, D.A., 2002. Chemical weathering of the Panola Granite: Solute and regolith elemental fluxes and the dissolution rate of biotite. In: Hellmann, R., Wood, S.A. (Eds.),
Water-rock Interaction, Ore Deposits, and Environmental Geochemisty: A tribute to David A. Crerar. The Geochemical Society, pp. 37-59.
White, A.F., Brantley, S.L., 2003. The effect of time on the weathering of silicate minerals: why do weathering rates differ in the laboratory and field? Chemical Geology, 202(3-4): 479-506.
White, A.F., Schulz, M.S., Lowenstern, J.B., Vivit, D.V., Bullen, T.D., 2005. The ubiquitous nature of accessory calcite in granitoid rocks: Implications for weathering, solute evolution, and petrogenesis. GCA, 69(6): 1455-1471.
White, A.F., Schulz, M.S., Lawrence, C.R., Vivit, D.V., Stonestrom, D.A., 2017. Long-term flow-through column experiments and their relevance to natural granitoid weathering rates. GCA, 202: 190-214.

Figure Captions

Figure 1. The field study was located in the west (dashed box) of the Czech Republic (dark grey). The inset shows the location of the Lysina catchment (red star) within the Slavkov Forest region (green).

Figure 2. (A) False colour BSE image of weathering Li-micas from a sample at 6.17 m depth from the Lysina core. Li-micas (Li) are highlighted in green, kaolinite (Kln) is highlighted in purple, and (Ab) albite in blue. The Li-micas maintain distinct mineral grains despite undergoing extensive alteration, as evidenced by the high abundance of clays within the mineral grains. Albite also shows extensive alteration and grains are beginning to lose their structure. Also shown are (Qtz) quartz in dark grey and (K-fs) K-feldspar grains in lighter

grey. (B) False colour BSE image of fluorite grains (flr, white) occupying pore spaces within albite grains (Ab, blue) with kaolinite (Kln, purple) in the Lysina core from 23.68 m depth. Also shown are apatite (Ap, cyan), K-feldspar (K-fs, light grey) and quartz (Qtz, dark grey). Fluorite grains are restricted to the more heavily weathered albite crystals and are absent from the less weathered K-feldspar and quartz grains, suggesting that fluorite formation occurred post albite weathering.

Figure 3. Geometric surface areas (Eq. 6) for the four key minerals within the Lysina profile. Dotted lines indicate the regolith-bedrock boundary. Note differing x-axis scale on panel c due to larger Li-mica surface area values. Uncertainty values were derived from standard error calculations on mineral diameters in each sample. Mineral surface areas increase relative to the parent sample in the upper 6.17 m of the core, particularly for (A) albite and (B) K-feldspar. (D) Quartz shows minimal significant changes in mineral surface areas through the profile.

Figure 4. Mass transfer coefficient (τ, Eq. 1) of select mobile elements within the Lysina profile, normalised to Ti. Black squares indicate data from Nwaogu (2014), open squares indicate data from Štědrá et al. (2016), while open circles indicate data produced in this study. Note differing x-axis scale on panel c due to enrichment of Li relative to the parent sample. All elements show a general depletion trend above 14.64 m except Li which shows depletion above 5 m.

Figure 5. The chemical index of alteration (CIA, Eq. 3) with depth in the Lysina core. The Lysina profile shows only limited weathering (CIA = 54-64); unweathered granites typically have CIA values of 40-55 (Bahlburg and Dobrzinski, 2011). Open circles indicate CIA values calculated using bulk geochemistry data from Štědrá et al. (2016). Error bars represent potential range of CIA values based on uncertainties in oxide abundance. Shaded area indicates hydrothermally altered zone while dotted-dashed lines indicate boundaries of a

zone of lithological variation identified by Štědrá et al. (2016) between 22.3 and 28 m depth. The hashed shaded area indicates zones of the core with a higher degree of fracturing.

Figure 6. Lysina elemental concentrations (C_w) normalised to Ti (Eq.4) in the upper 14.64 m of the Lysina core. Dashed red lines show gradients used in weathering rate calculations (Eq. 5) and dotted lines indicate the bedrock-regolith boundary. (A) Na shows gradual loss from 14.64 m to 4.3 m and more significant losses above 4.3 m. (B) K shows initial loss between 14.64 m and 14.4 m but remains relatively stable until 4.3 m, above which loss occurs towards the surface.

Figure 7. Chemical Index of Alteration (CIA, Eq. 3) with depth for (A) Curacavi, (B) Lysina, (C) Davis Run, (D) Panola, (E) Hakgala, and (F) Río Icacos in order of increasing MAP. Dotted lines indicate the bedrock-regolith boundaries. The Curacavi profile is entirely saprolite and fresh bedrock was not reached. Curacavi and Lysina show deep profiles with only limited changes in CIA values, while Davis Run, Panola, and Hakgala show clear transitions from fresh to more highly weathered material over 5-10 m distances. Río Icacos displays a sharp transition from fresh to nearly totally depleted material over only 1 m distance. Nsimi is excluded due to non-continuous sampling methods used on that profile.

Figure 8. Ca mass transfers, τ_{Ca} (Eq.1), normalised to Ti for (A) Lysina, (B) Davis Run, (C) Panola, (D) Río Icacos, and Na mass transfer coefficients normalised to Ti for (E) Lysina, (F) Davis Run, (G) Panola, and (H) Río Icacos. The dotted line indicates the regolith-bedrock boundary. Uncertainty estimates are unavailable for Davis Run and Panola.

Figure 9. K mass transfer coefficients, τ_K (Eq. 1), normalised to Ti for (A) Lysina, (B) Davis Run, (C) Panola, (D) Río Icacos, and Li or Mg mass transfer coefficients normalised to Ti (τ_{Li} for Lysina and τ_{Mg} for the other sites) for (E) Lysina, (F) Davis Run, (G) Panola, and (H) Río Icacos, representing mica weathering fronts at each site. Note differing x-axis scale on panel

e to show enrichment of Li in the Lysina profile. Dotted line indicates the regolith-weathering boundary. Uncertainty estimates are unavailable for Davis Run and Panola. Uncertainty values are sufficiently small at Río Icacos to be contained within the symbols.

Figure 10. Log plagioclase weathering rates from the four primary sites plotted against (A) mean annual temperature, (B) mean annual precipitation, and (C) erosion rates (Tables 1 and 5). Plagioclase rates show a stronger correlation with MAP ($r^2 = 0.98$, $p = 0.009$) than MAT ($r^2 = 0.68$, $p = 0.18$) which shows inconsistent changes in rates over similar values (i.e., a decrease in rates over a 5 ^{o}C increase between Lysina and Davis Run, and three orders of magnitude increase over a 5 ^{o}C increase between Panola and Río Icacos). Erosion rates show no clear correlation with plagioclase weathering rates in this sample. Due to the low sample size confidence in these correlations is very low.

Figure 11. Regolith depth plotted against erosion rates for all sites (Table 1). Regolith depth shows a general decrease where erosion rates are highest, although Curacavi (Erosion Rate = 40.5 m Myr^{-1}, Depth = 33 m) is an outlier in this trend. An exponential trendline returns a correlation of r^2=0.97 (significant at the 95% confidence level) if the outlier (Curacavi) is excluded.

Figure 12. Na weathering gradients (as a proxy for plagioclase weathering) correlated against (A) MAT, (B) MAT, and (C) erosion rates at six of the field sites (Table 1). Nsimi is excluded due to non-continuous sampling of that profile preventing the calculation of a gradient value. Na weathering gradients strongly correlate with MAP ($r^2 = 0.86$, $p = 0.007$), while correlations are much weaker for MAT and erosion rates.

Figure 13. Chemical weathering rates (CWR) from 18 sites plotted against (A) mean annual runoff (MAR), (B) mean annual precipitation, (C) mean annual temperatures (MAT), and (d) erosion rates, using data compiled by West et al. (2005) (black squares) and sites from this study (open circles) where data are available. Note that the Nsimi and Río Icacos catchments are included within the West et al. (2005) dataset. The strongest correlations are between CWR and MAP/MAR, with a slightly weaker correlation between CWR and erosion rates. MAT shows no significant correlation with CWR, suggesting that MAR, MAP and erosion are much stronger controls on CWR. The majority of the sites are granitic or granitic/metamorphic, along with four sites with purely metamorphic lithologies.

Figure 1

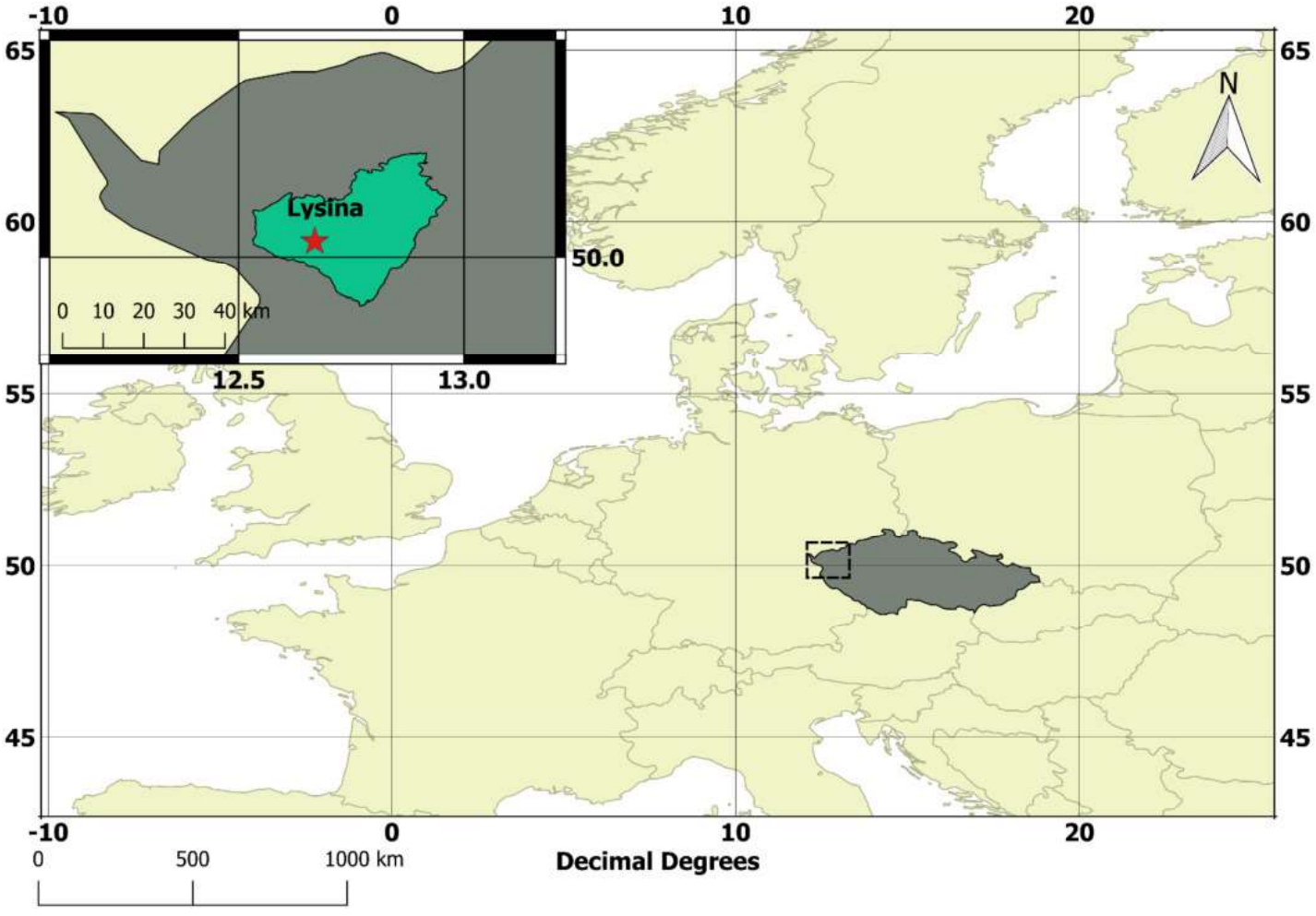
-10
0
10
20
65
60
55
50
45
Lysina
0 10 20 30 40 km
12.5
13.0
50.0
N
0
500
1000 km
Decimal Degrees

Figure 2

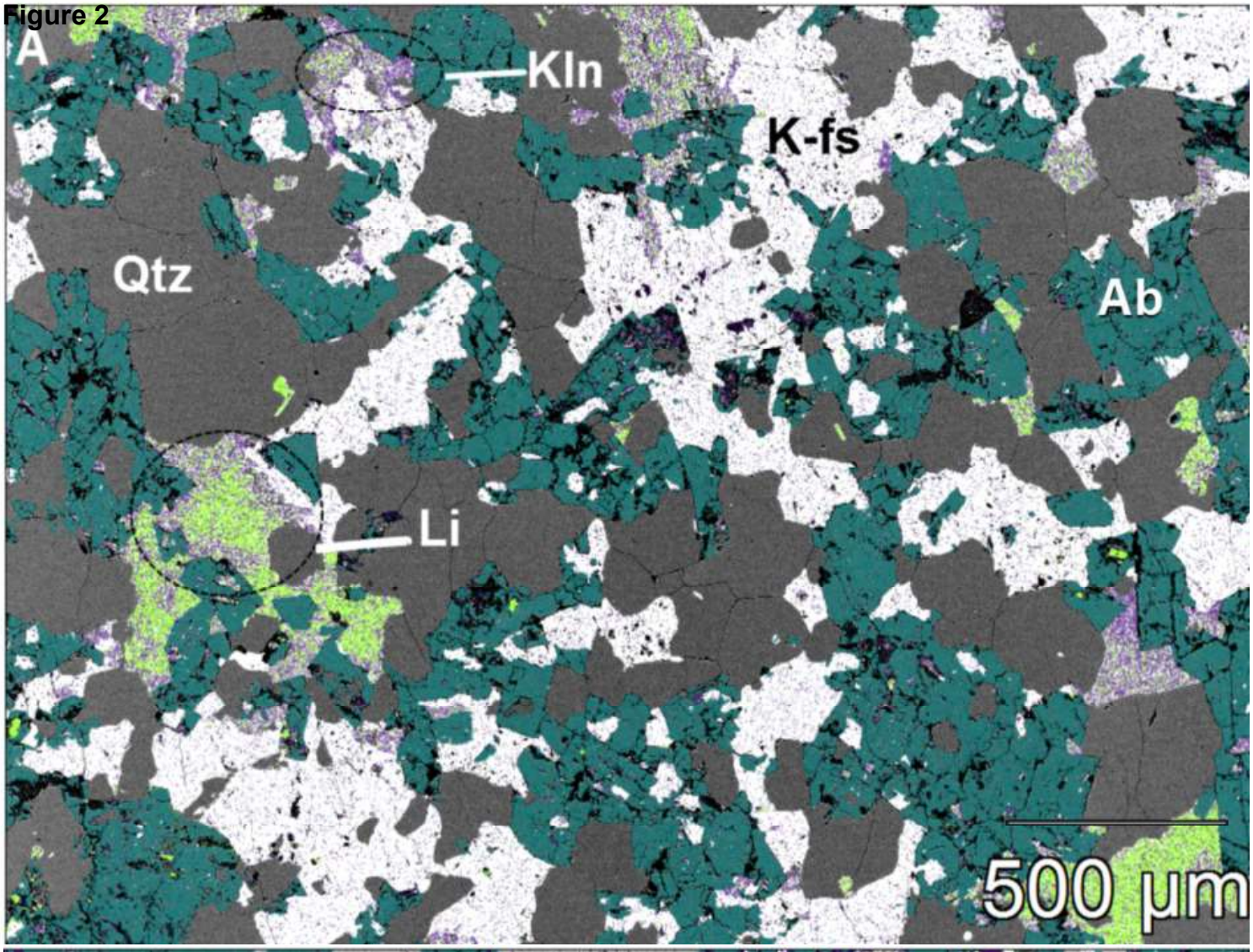

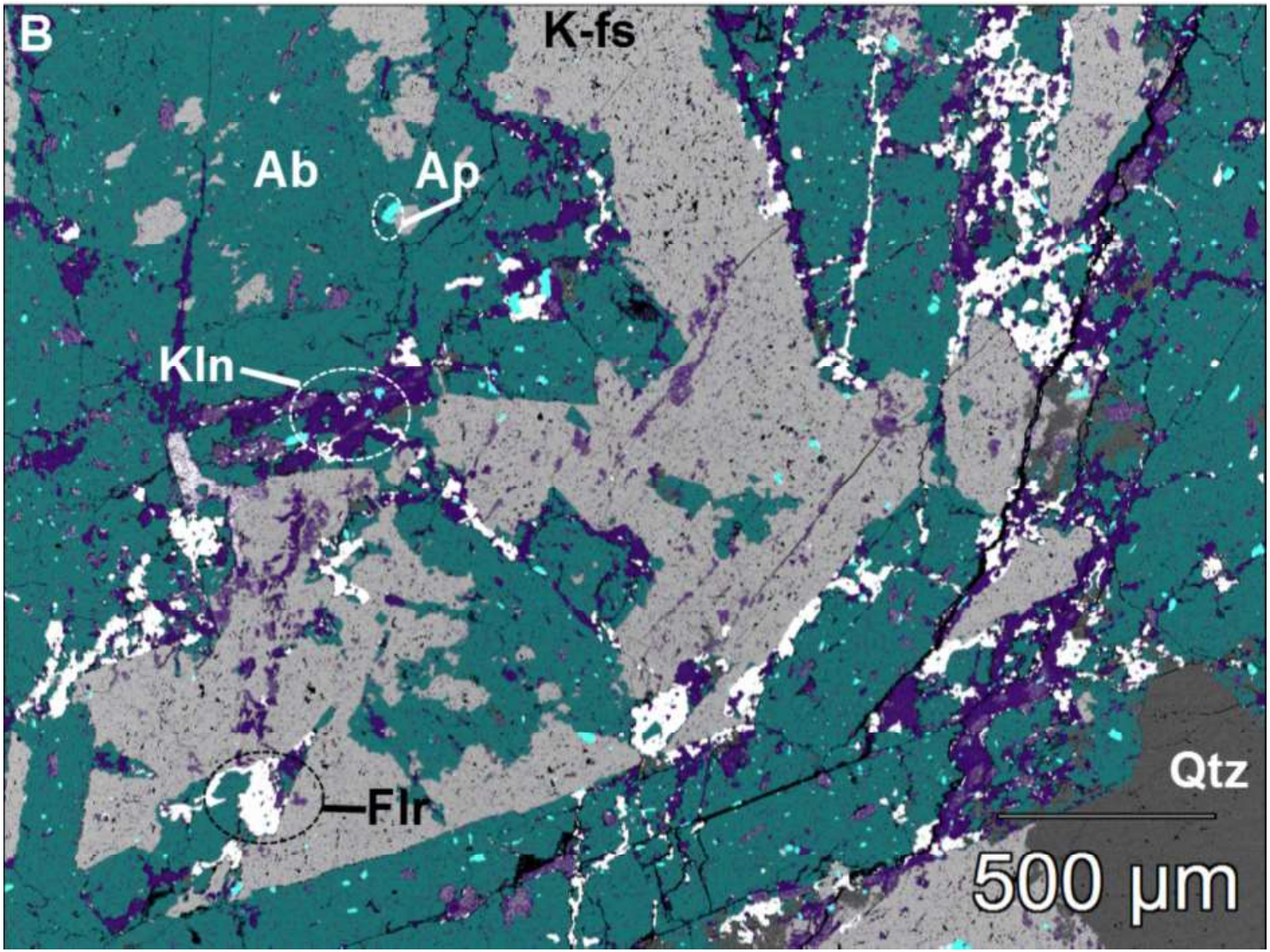

Figure 3

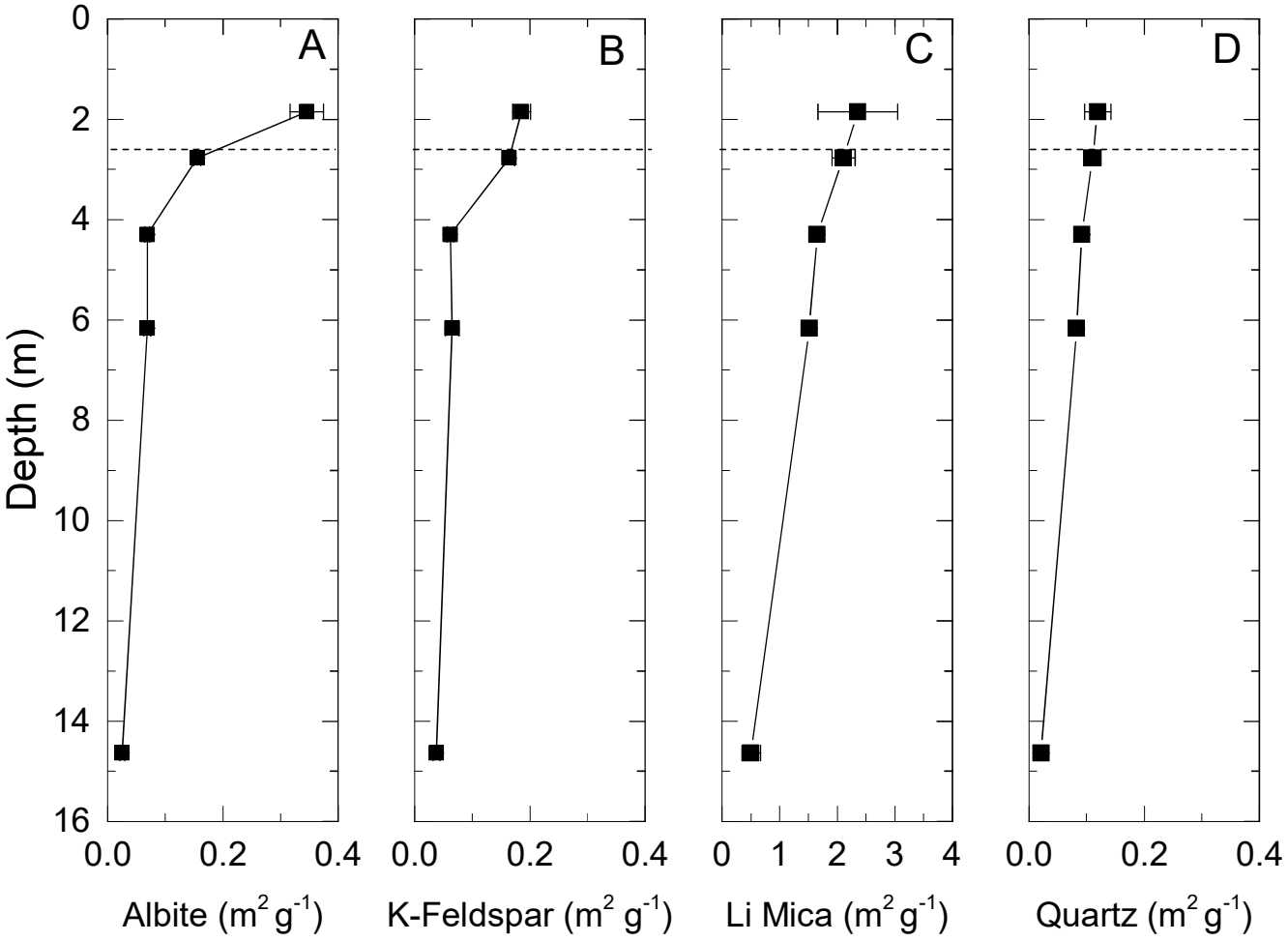
A
B
C
D
Depth (m)
0
2
4
6
8
10
12
14
16
0.0
0.2
0.4
0
1
2
3
4
Albite (m² g⁻¹)
K-Feldspar (m² g⁻¹)
Li Mica (m² g⁻¹)
Quartz (m² g⁻¹)

Figure 4

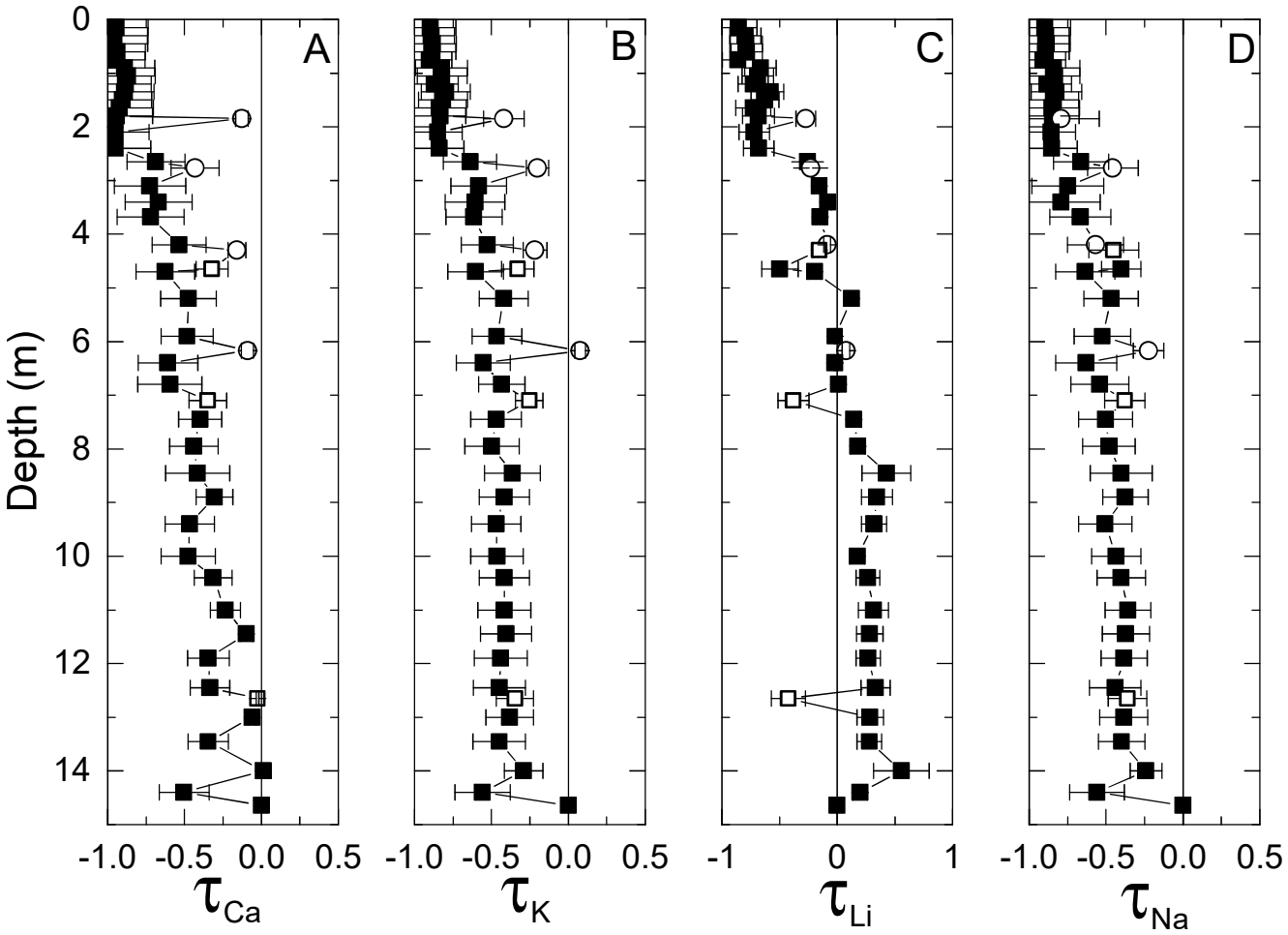
Depth (m)
0
2
4
6
8
10
12
14
A
B
C
D
-1.0 -0.5 0.0 0.5
-1.0 -0.5 0.0 0.5
-1 0 1
-1.0 -0.5 0.0 0.5
τCa
τK
τLi
τNa

Figure 5 Revised

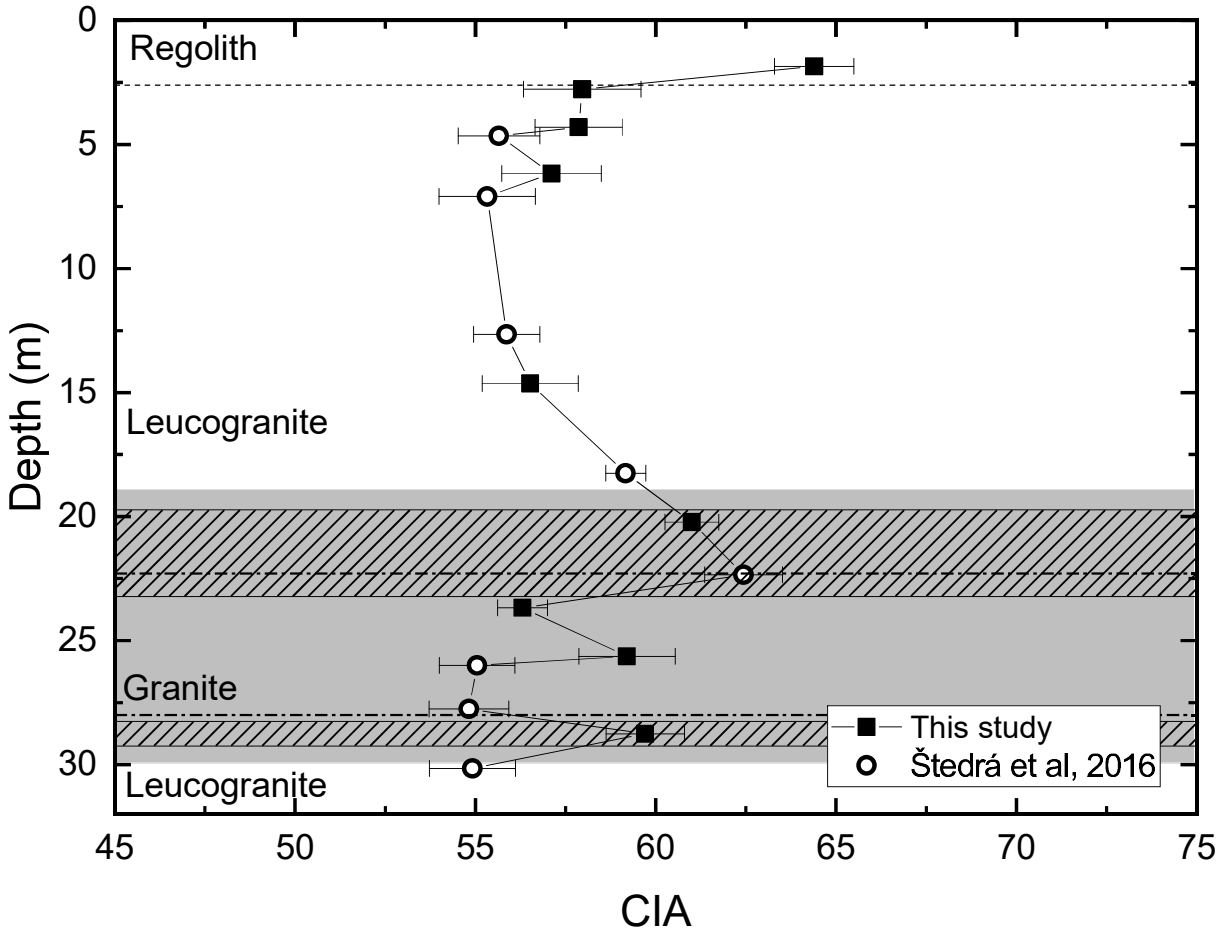

Figure 6

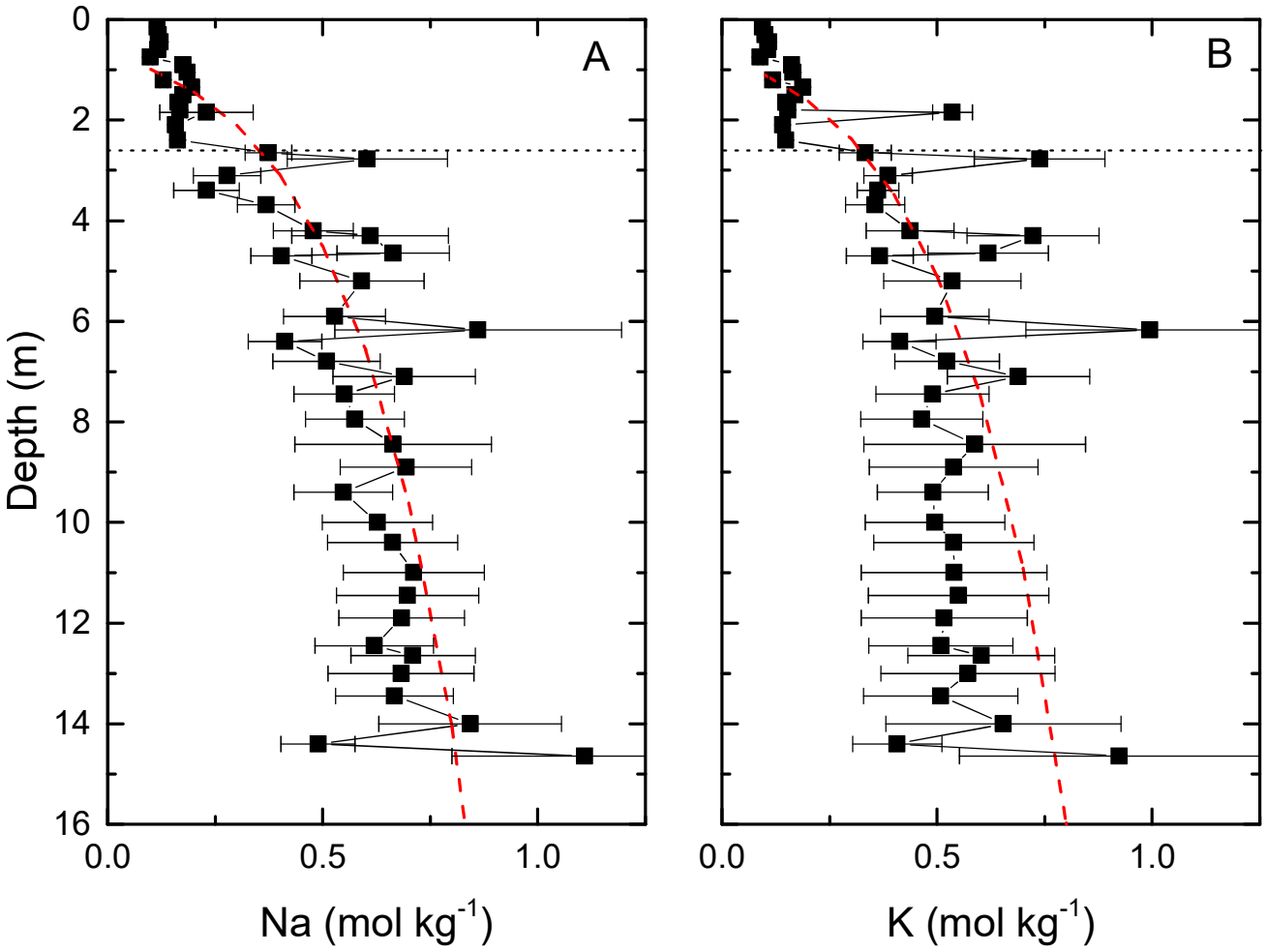

Figure 7

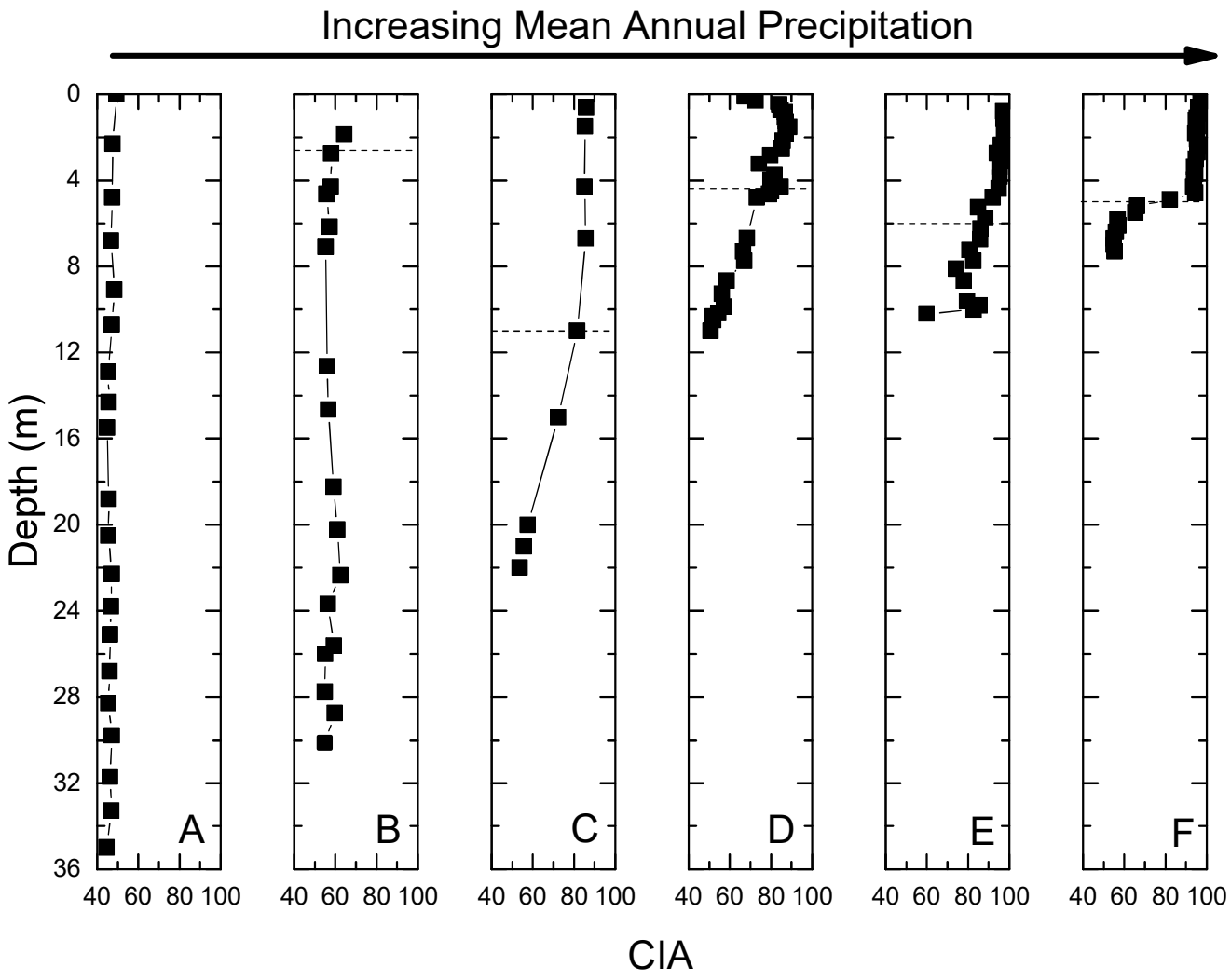
Increasing Mean Annual Precipitation
Depth (m)
0
4
8
12
16
20
24
28
32
36
A
B
C
D
E
F
40 60 80 100
CIA

Figure 8

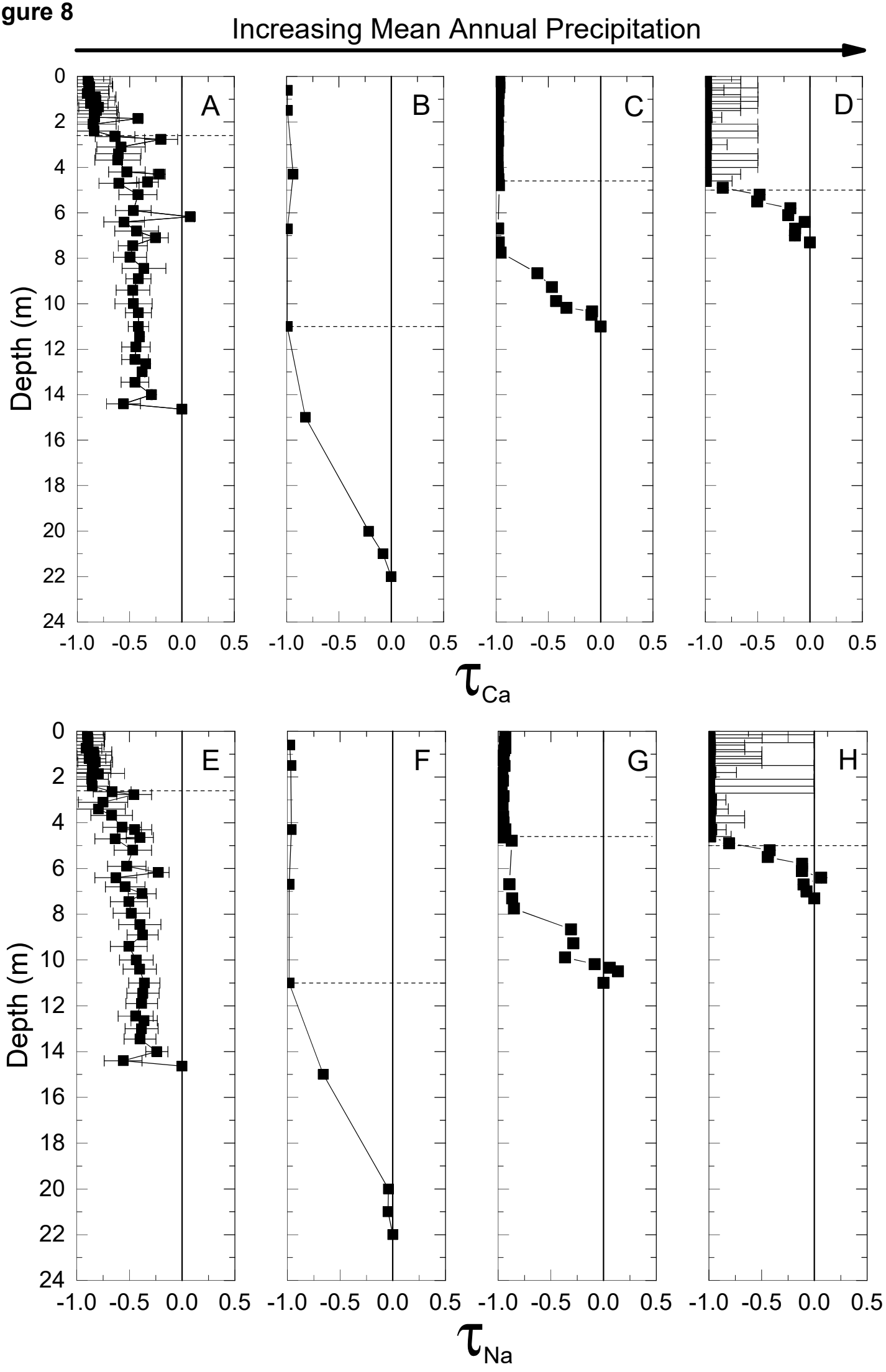
Increasing Mean Annual Precipitation
A
B
C
D
E
F
G
H
Depth (m)
0
2
4
6
8
10
12
14
16
18
20
22
24
-1.0
-0.5
0.0
0.5
τ_{Ca}
τ_{Na}

Figure 9

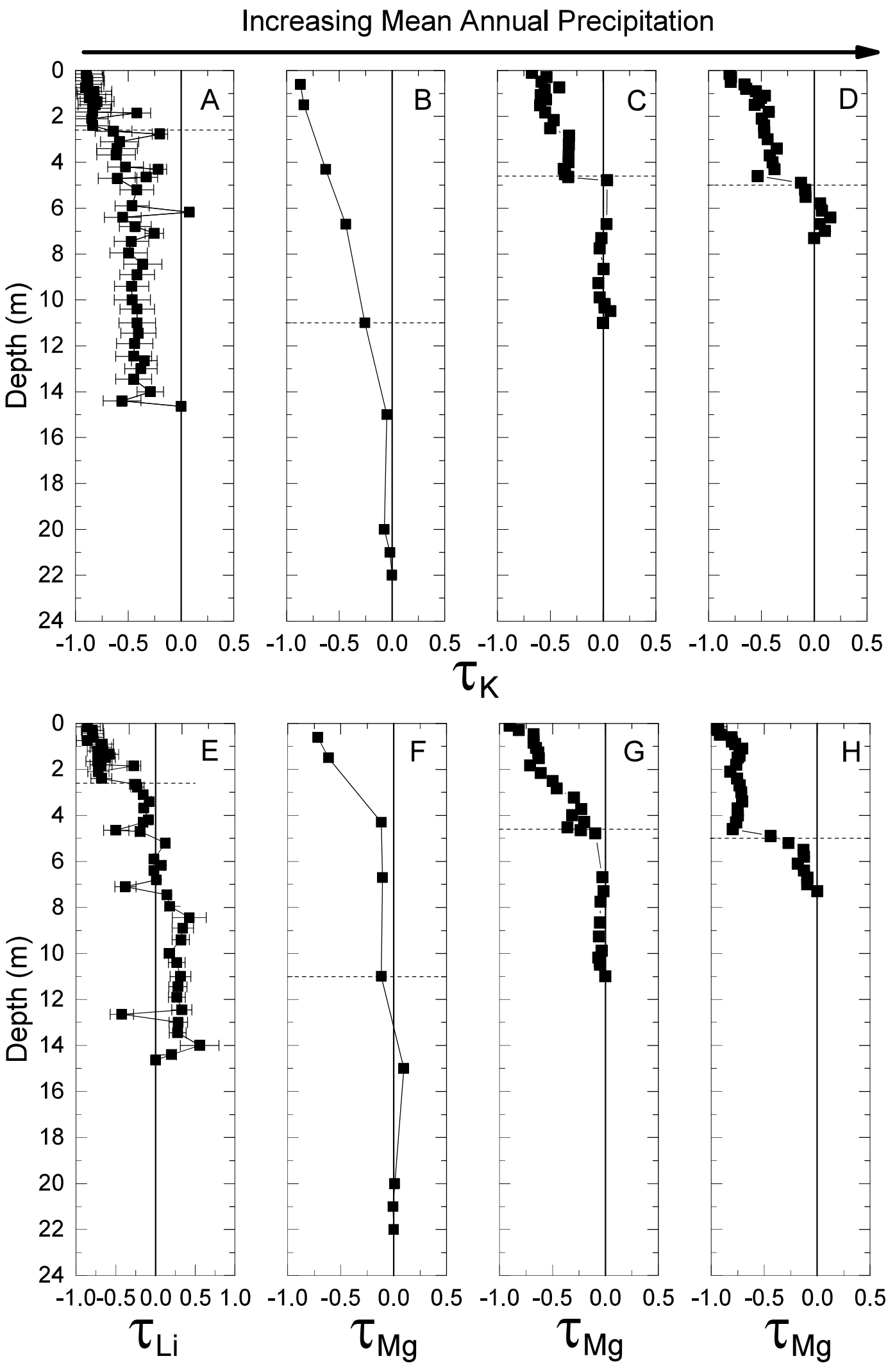
Increasing Mean Annual Precipitation
Depth (m)
A
B
C
D
E
F
G
H
τ_K
τ_{Li}
τ_{Mg}
τ_{Mg}
τ_{Mg}

Figure 10

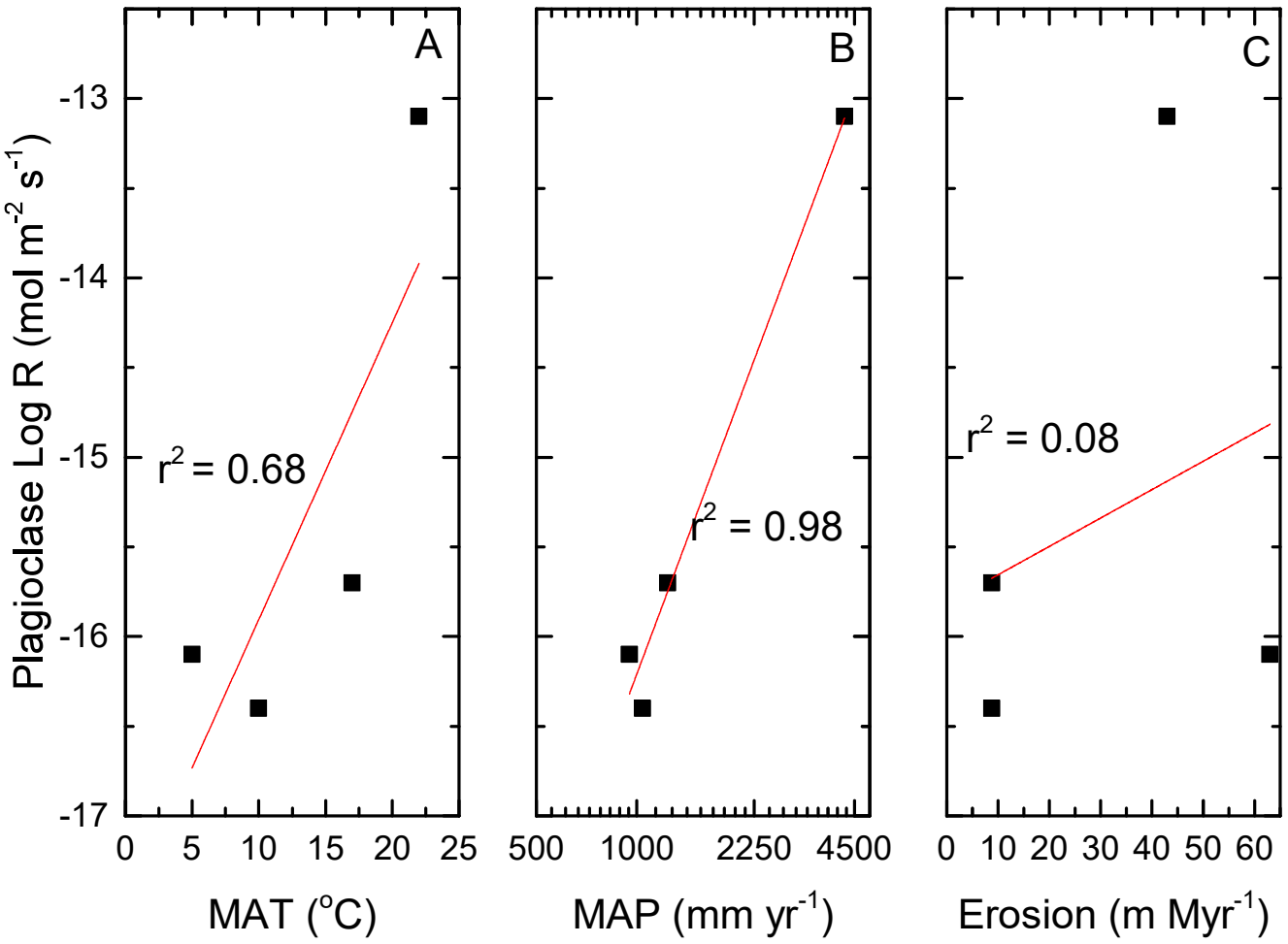
A
B
C
Plagioclase Log R (mol m-2 s-1)
-13
-14
-15
-16
-17
r2 = 0.68
r2 = 0.98
r2 = 0.08
0 5 10 15 20 25
500 1000 2250 4500
0 10 20 30 40 50 60
MAT (°C)
MAP (mm yr-1)
Erosion (m Myr-1)

Figure 11

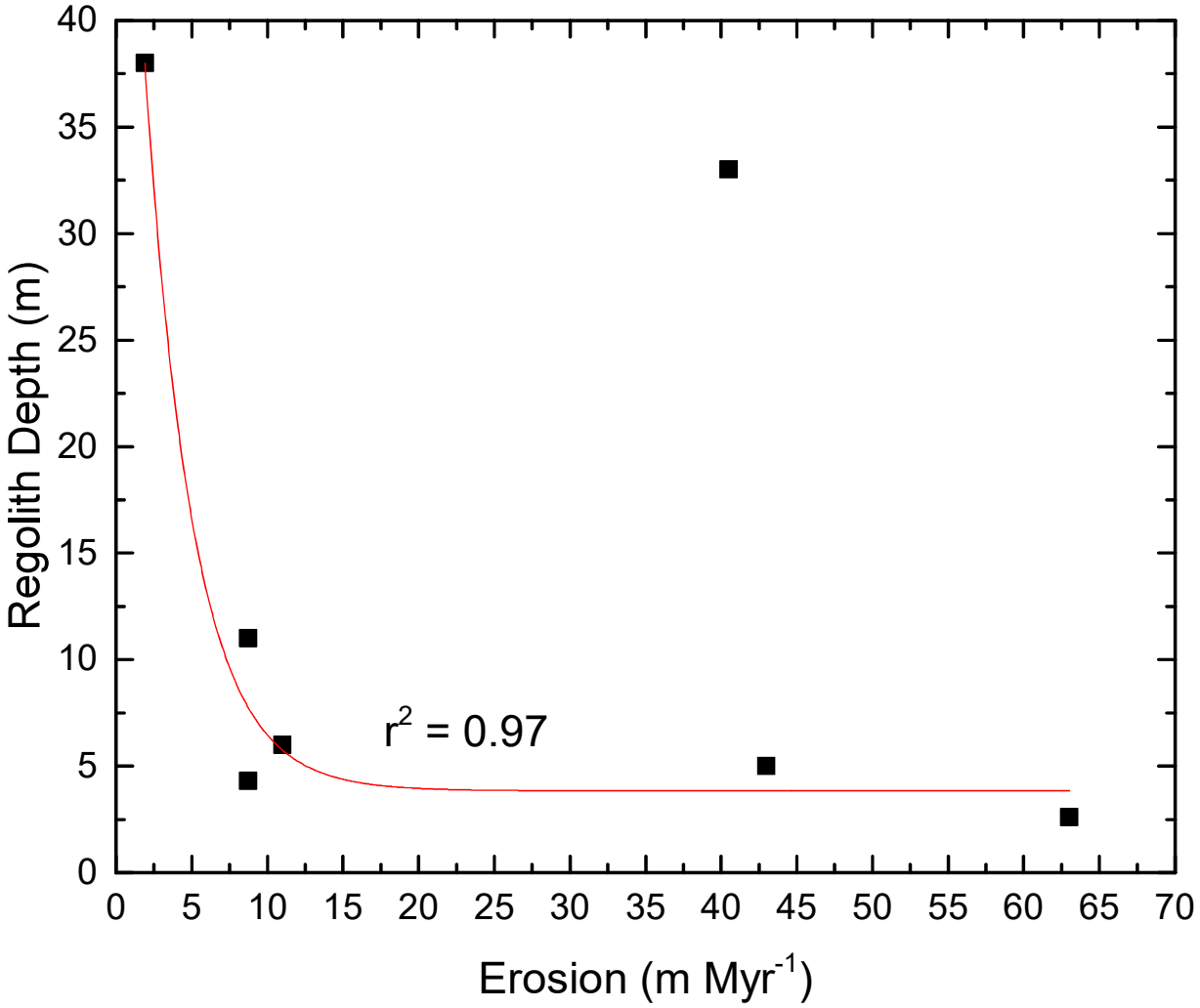
Regolith Depth (m)
Erosion (m Myr-1)
r2 = 0.97
0
5
10
15
20
25
30
35
40
45
50
55
60
65
70

Figure 12

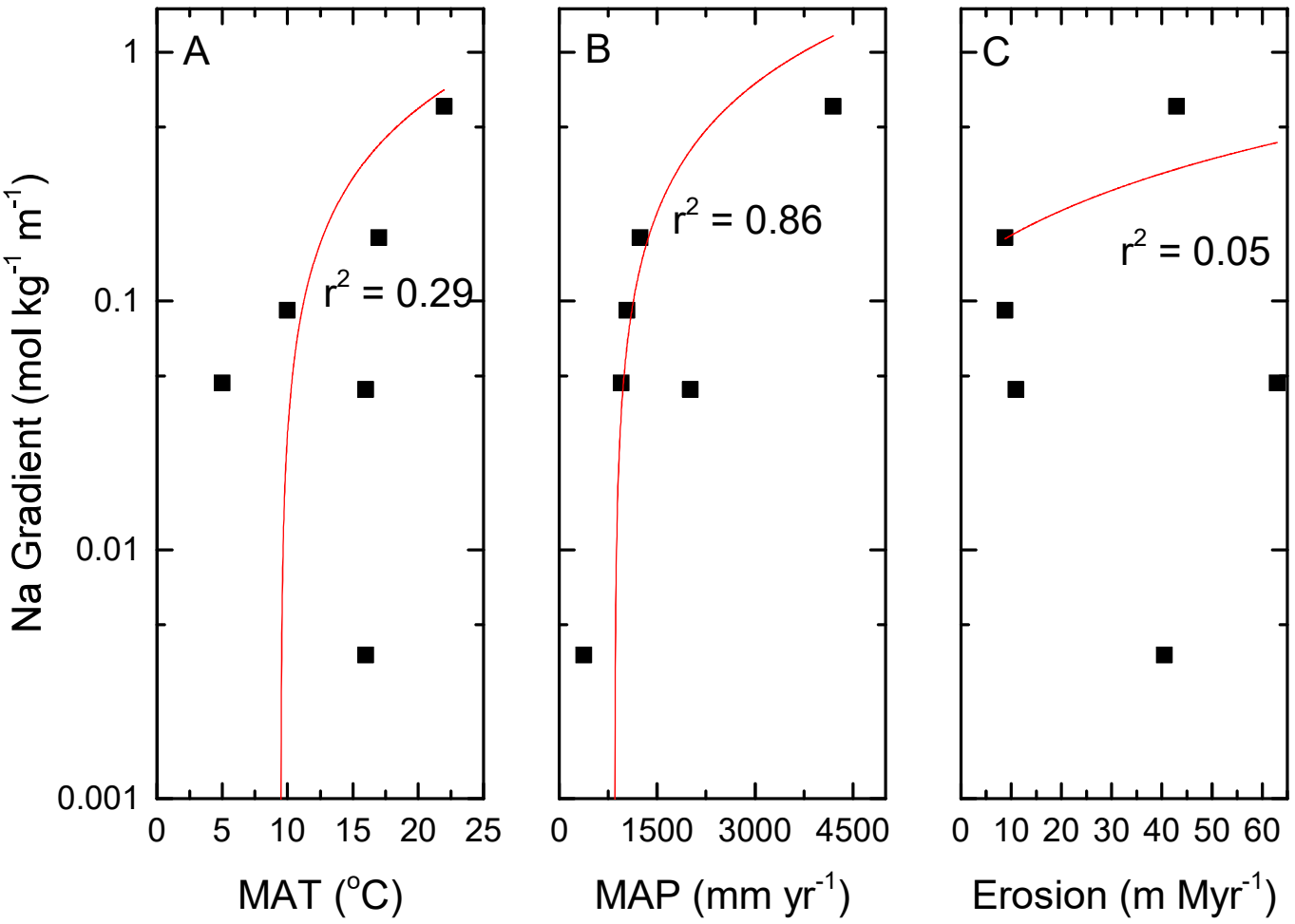
A
B
C
Na Gradient (mol kg-1 m-1)
1
0.1
0.01
0.001
r2 = 0.29
r2 = 0.86
r2 = 0.05
0 5 10 15 20 25
MAT (°C)
0 1500 3000 4500
MAP (mm yr-1)
0 10 20 30 40 50 60
Erosion (m Myr-1)

Figure 13

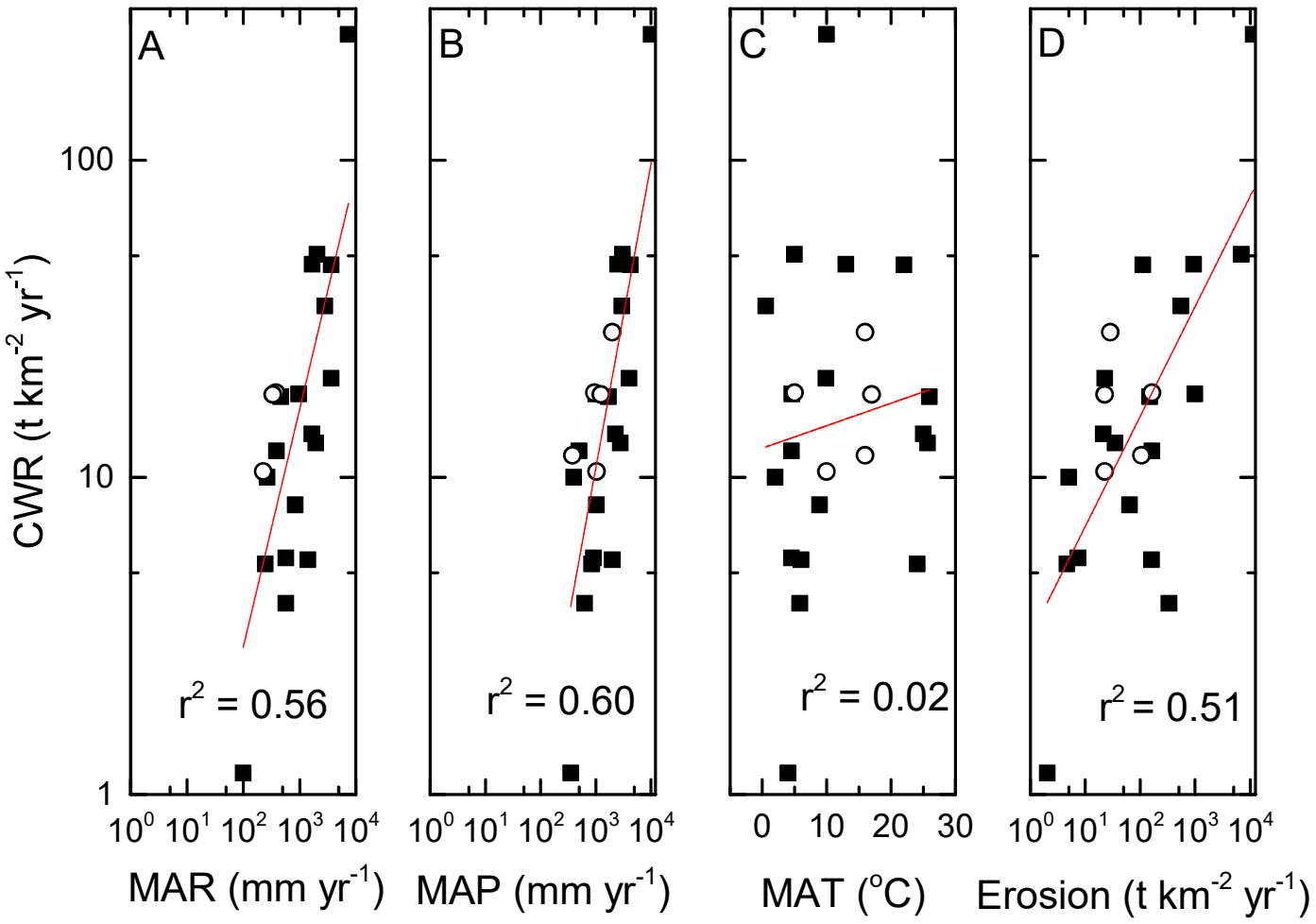
A
B
C
D
100
10
1
CWR (t km-2 yr-1)
r2 = 0.56
r2 = 0.60
r2 = 0.02
r2 = 0.51
10^0 10^1 10^2 10^3 10^4
0 10 20 30
MAR (mm yr-1)
MAP (mm yr-1)
MAT (°C)
Erosion (t km-2 yr-1)

Table 1: Site locations and environmental data

Site	Location	MAT (°C)	MAP (mm yr^{-1})	CWR (m Myr^{-1})	Erosion (m Myr^{-1})	Regolith Depth (m)	Lithology
Curacavi[a]	Chile	16	380	4.5	40.5 ± 22.5	>33	Granodiorite
Davis Run[b,c]	Virginia, USA	10	1040	4	8.75 ± 4.25	11	Granodiorite
Hakgala[d]	Sri Lanka	16	2013	11	11	6	Granitic Gneiss
Lysina[e,f]	Czech Republic	5	950	7.1	63	2.6	Leucogranite
Nsimi[g,h]	Cameroon	26	1700	2.8	1.9	38	Granite
Panola[b,c]	Georgia, USA	17	1240	7	8.75 ± 4.25	4.3	Granodiorite
Río Icacos[i,j,k]	Puerto Rico	22	4200	43	43	5	Tonalite

[a]Vázquez et al. (2016) [b]White et al. (2001), [c]Brantley et al. (2017), [d]Hewawasam et al. (2013), [e]Krám et al. (2012), [f]Dannhaus et al. (2018), [g]Braun et al. (2005), [h]Braun et al. (2012), [i]White and Blum (1995),[j]Chabaux et al. (2013),[k]Buss et al. (2017). MAT – Mean Annual Temperature, MAP – Mean Annual Precipitation, CWR – Chemical Weathering Rate (whole rock).

Table 2: Lysina bulk elemental chemistry[a]

Depth (m)	SiO_2 (wt %)	Al_2O_3 (wt %)	CaO (wt %)	Fe_2O_3 (wt %)	FeO[d] (wt %)	K_2O (wt %)	Li_2O (wt %)	MgO (wt %)	Na_2O (wt %)	TiO_2 (wt %)	CIA	Rock Type
Detection Limit	**0.01**	**0.01**	**0.01**	**0.01**	**0.1**	**0.01**	**0.0001**	**0.01**	**0.01**	**0.01**	**-**	**-**
0.15	nd[e]	9.0	0.11	0.82	nd[e]	2.01	0.10	0.10	1.61	0.23	54.9	R[f]
0.30	nd	11.7	0.09	0.93	nd	2.68	0.17	0.11	2.08	0.28	55.1	R
0.45	nd	12.4	0.10	1.62	nd	2.64	0.16	0.17	1.94	0.26	57.4	R
0.60	nd	13.7	0.15	2.24	nd	2.70	0.17	0.29	1.95	0.27	59.3	R
0.75	nd	12.9	0.10	2.06	nd	2.72	0.13	0.21	1.99	0.32	57.8	R
0.90	nd	12.3	0.18	1.65	nd	2.69	0.17	0.23	1.93	0.18	56.6	R
1.05	nd	14.4	0.24	1.73	nd	3.03	0.17	0.27	2.22	0.19	57.0	R
1.20	nd	13.5	0.26	1.60	nd	2.73	0.19	0.29	1.96	0.24	57.8	R
1.35	nd	16.6	0.19	1.28	nd	3.32	0.23	0.22	2.27	0.19	59.4	R
1.50	nd	15.2	0.18	1.22	nd	3.18	0.21	0.19	2.15	0.20	58.6	R
1.65	nd	11.0	0.12	1.21	nd	2.38	0.13	0.15	1.73	0.17	57.0	R
1.80	nd	12.5	0.10	1.17	nd	2.65	0.17	0.16	1.92	0.18	57.7	R
1.85[b]	72.1	13.7	0.67	1.77	1.6	4.20	0.17	0.55	1.19	0.08	64.4	R
2.10	nd	14.1	0.10	1.22	nd	2.97	0.18	0.19	2.19	0.22	57.7	R
2.40	nd	13.5	0.10	1.21	nd	2.86	0.19	0.18	2.07	0.21	57.8	R
2.65	nd	15.9	0.30	1.35	nd	3.27	0.22	0.22	2.41	0.10	57.3	LG
2.77[b]	75.1	13.4	0.35	1.53	1.4	4.64	0.15	0.15	2.49	0.07	58.0	LG
3.10	nd	14.3	0.21	1.36	nd	3.01	0.20	0.55	1.43	0.08	61.6	LG
3.40	nd	13.9	0.24	1.30	nd	2.74	0.21	0.68	1.14	0.08	63.8	LG
3.68	nd	13.3	0.23	1.30	nd	3.02	0.22	0.21	2.05	0.09	56.0	LG
4.20	nd	13.8	0.34	1.20	nd	3.25	0.21	0.13	2.34	0.08	54.0	LG
4.30[b]	73.5	13.9	0.52	1.52	1.4	4.54	0.16	0.18	2.52	0.07	57.9	LG
4.65[c]	72.8	14.3	0.50	1.17	1.0	4.66	0.12	0.19	3.29	0.08	55.0	LG
4.70	nd	13.3	0.30	1.25	nd	3.02	0.20	0.16	2.19	0.09	54.2	LG
5.20	nd	13.4	0.30	1.18	nd	3.14	0.20	0.15	2.28	0.06	54.1	LG
5.90	nd	13.8	0.34	1.13	nd	3.27	0.20	0.14	2.30	0.07	57.1	LG
6.17[b]	72.5	13.4	0.42	1.24	1.2	4.69	0.16	0.15	2.67	0.05	54.7	LG
6.40	nd	13.1	0.29	1.23	nd	3.16	0.23	0.16	2.08	0.08	53.9	LG
6.80	nd	13.6	0.26	1.10	nd	3.48	0.21	0.15	2.22	0.07	52.9	LG
7.10[c]	74.7	13.1	0.42	1.17	1.1	4.54	0.13	0.14	2.99	0.07	54.3	LG
7.45	nd	13.4	0.39	1.15	nd	3.24	0.23	0.18	2.39	0.07	52.7	LG
7.95	nd	13.7	0.35	1.20	nd	2.97	0.23	0.17	2.42	0.07	53.0	LG

8.45	nd	9.7	0.23	0.87	nd	2.38	0.18	0.09	1.77	0.04	53.0	LG
8.90	nd	13.4	0.38	1.14	nd	3.00	0.23	0.12	2.54	0.06	53.0	LG
9.40	nd	13.6	0.35	1.35	nd	3.30	0.27	0.12	2.43	0.07	52.8	LG
10.00	nd	13.2	0.31	0.99	nd	3.02	0.22	0.10	2.51	0.06	53.1	LG
10.40	nd	13.1	0.38	1.03	nd	3.02	0.22	0.14	2.45	0.06	53.1	LG
11.00	nd	12.8	0.39	0.92	nd	2.80	0.21	0.15	2.43	0.06	52.7	LG
11.45	nd	13.1	0.46	0.92	nd	2.88	0.21	0.15	2.41	0.06	52.8	LG
11.90	nd	12.9	0.36	1.00	nd	2.89	0.22	0.11	2.51	0.06	52.4	LG
12.45	nd	12.8	0.38	1.07	nd	2.98	0.24	0.13	2.39	0.06	53.0	LG
12.65[c]	74.3	13.3	0.63	1.04	1.0	3.97	0.12	0.16	3.08	0.07	53.0	LG
13.00	nd	13.1	0.49	1.07	nd	3.04	0.21	0.15	2.39	0.06	53.3	LG
13.45	nd	13.4	0.38	1.03	nd	2.98	0.23	0.12	2.57	0.06	57.0	LG
14.00	nd	14.4	0.48	0.95	nd	3.18	0.23	0.14	2.70	0.05	52.9	LG
14.40	nd	13.3	0.37	1.24	nd	3.06	0.28	0.18	2.41	0.08	53.2	LG
14.64[b]	71.9	14.3	0.46	1.05	1.1	4.35	0.14	0.12	3.44	0.05	52.2	LG
15.04	nd	13.1	0.41	0.88	nd	3.05	0.20	0.15	2.39	0.05	52.9	LG
15.35	nd	14.0	0.42	0.94	nd	3.07	0.22	0.18	2.62	0.06	53.3	LG
15.90	nd	13.2	0.78	1.00	nd	2.94	0.24	0.19	2.26	0.05	53.5	LG
16.35	nd	13.4	0.36	0.98	nd	3.17	0.22	0.12	2.47	0.06	55.1	LG
16.95	nd	13.9	0.40	1.03	nd	3.19	0.25	0.13	2.49	0.06	54.5	LG
17.45	nd	13.2	0.38	1.17	nd	3.16	0.27	0.15	2.24	0.07	54.4	LG
17.90	nd	15.1	0.45	0.94	nd	3.38	0.27	0.21	2.36	0.05	54.1	LG
18.25[c]	71.4	14.9	1.25	0.87	0.7	3.55	0.17	0.28	2.54	0.03	59.2	LG
18.40	nd	14.1	0.46	1.01	nd	3.19	0.27	0.22	2.26	0.06	54.3	LG
18.95	nd	14.9	0.43	1.07	nd	3.50	0.30	0.19	2.38	0.06	61.0	AFG
19.45	nd	14.5	0.60	1.28	nd	3.94	0.34	0.26	1.80	0.05	58.1	AFG
20.05	nd	15.4	0.95	1.46	0.8	2.93	0.40	0.22	2.43	0.06	65.0	AFG
20.22[b]	75.6	13.4	2.03	1.01	nd	3.32	0.27	0.22	0.92	0.03	50.0	AFG
20.45	nd	11.2	0.55	1.06	nd	1.94	0.26	0.21	1.47	0.05	58.1	AFG
20.90	nd	12.4	0.47	1.68	nd	2.23	0.40	0.16	0.75	0.07	65.0	AFG
21.40	nd	12.1	1.65	0.85	nd	2.27	0.24	0.16	1.82	0.03	50.0	AFG
22.05	nd	13.6	0.51	0.87	nd	2.82	0.27	0.27	1.64	0.04	58.1	AFG
22.35[c]	65.4	18.6	0.63	1.09	0.8	6.97	0.16	0.31	1.53	0.07	62.4	AFG
22.45	nd	13.1	0.45	0.67	nd	2.68	0.20	0.25	1.77	0.03	57.4	AFG
22.95	nd	18.4	0.71	0.98	nd	5.47	0.28	0.09	0.26	0.04	61.2	AFG

23.45	nd	13.7	0.55	0.87	nd	3.05	0.20	0.16	2.38	0.05	53.4	AFG
23.68[b]	69.5	15.9	0.80	1.31	1.1	5.77	0.22	0.13	3.10	0.05	56.3	AFG
23.95	nd	12.2	0.75	0.88	nd	2.77	0.15	0.13	1.99	0.03	52.4	AFG
24.45	nd	14.4	1.02	1.57	nd	3.31	0.35	0.19	2.30	0.08	51.8	AFG
24.95	nd	13.6	0.58	1.10	nd	3.06	0.26	0.13	2.43	0.05	52.8	AFG
25.63[b]	73.9	13.9	0.45	1.63	1.5	3.95	0.19	0.22	3.03	0.07	59.2	AFG
26.00[c]	69.5	15.4	0.54	1.09	1.1	6.86	0.16	0.23	2.54	0.09	55.0	AFG
27.75[c]	71.4	22.9	0.51	1.82	1.5	5.70	0.30	0.23	2.40	0.15	54.8	AFG
28.75[b]	59.6	22.9	0.57	1.79	1.5	8.67	0.25	0.45	3.07	0.08	59.7	AFG
30.15[c]	72.9	13.6	0.47	1.09	1.0	5.94	0.16	0.20	2.37	0.09	54.9	LG

[a]Lysina bulk chemistry measured using ICP-OES after Li metaborate fusion; Li and other trace elements measured by ICP-MS after multi-acid digest. [b]Samples analysed in this study, and [c]in Štědrá et al. (2016); other samples analysed by Nwaogu (2014). [d]FeO concentrations were measured by titration methods. Detection limits are shown in the second row. [e] SiO_2 and FeO concentrations were not determined by Nwaogu (2014), denoted by nd. [f] Simplified rock types within the Lysina core include *R* (regolith), *LG* (leucogranite), and *AFG* (alkali-feldspar granite). Due to the small volume of apatite within the Lysina core no correction for apatite was applied to the CIA values.

Table 3: Lysina mineralogy[a]

Depth (m)	Quartz (wt%)	Albite (wt%)	K-Feldspar (wt%)	Kaolinite (wt%)	Illite (wt%)	Li-Mica (wt%)	Apatite (wt%)	Density[c] (g cm^{-3})	Notes
1.85	33.4	4.30	15.9	24.9	nd[b]	10.9	0.75	2.53	1.9 % Jarosite
2.77	38.1	24.4	20.5	5.12	4.50	6.92	0.44	2.65	
4.30	29.7	27.0	27.3	6.05	5.05	4.28	0.52	2.47	
6.17	27.5	29.5	29.8	3.02	5.65	2.65	0.80	2.49	
14.64	35.5	30.3	16.8	5.18	5.27	5.72	0.48	2.59	
20.22	40.8	7.33	22.2	18.3	2.84	6.32	0.58	2.59	0.61 % Fe-oxides, fractured
23.68	24.9	25.8	25.0	8.76	1.11	3.33	nd	2.72	3 % fluorite
25.63	30.7	27.8	25.5	2.71	1.95	5.97	nd	2.54	
28.75	10.9	19.9	35.5	12.7	8.04	12.1	0.81	2.52	Heavily fractured

[a]Mineralogical abundances of Lysina samples derived from EDS phase analysis of thin sections and converted to wt % using mineral density values from the literature (Deer et al., 2013). [b] = not detected. [c]Density values were calculated using sample porosity values and literature values of mineral densities. Some minor minerals present (e.g., monazite) are not shown in this table due to low abundance and absence from some samples.

Table 4: Lysina mineral diameters[a]

	Sample Depth (m)	n	Mean Diameter[b,c] (μm)	Max Diameter (μm)	Min Diameter (μm)	Range (μm)
Albite	**1.85**	51	46 ± 4	168	14	154
	2.77	193	102 ± 4	323	18	305
	4.30	147	233 ± 14	1143	47	1096
	6.17	120	232 ± 20	1978	41	1937
	14.64	37	599 ± 89	1843	53	1790
K-feldspar	**1.85**	52	88 ± 7	224	24	200
	2.77	173	100 ± 6	549	21	528
	4.30	109	264 ± 23	1469	40	1429
	6.17	75	252 ± 44	2619	43	2576
	14.64	40	414 ± 62	1743	41	1702
Quartz	**1.85**	53	133 ± 24	1207	33	1174
	2.77	160	144 ± 19	2511	18	2493
	4.30	171	172 ± 10	712	31	681
	6.17	131	192 ± 11	675	49	626
	14.64	21	680 ± 146	2220	32	2188
Li-Mica	**1.85**	29	99 ± 31	928	17	911
	2.77	56	111 ± 12	440	16	424
	4.30	96	142 ± 8	432	30	402
	6.17	65	154 ± 11	438	51	387
	14.64	11	462 ± 155	1869	84	1785

[a]Diameters of the four primary minerals within the Lysina core. [b]Mineral diameters were measured using NSS 3.0. As many of the minerals had an elongated shape, the diameter was estimated as the square root of the sum of the long and short axes of a mineral grain. Secondary clays such as kaolinite had mineral grain sizes too small to accurately measure. [c]Uncertainty for mean diameter values was estimated from standard error calculations.

Table 5: Mineral specific weathering rates

	Lysina[a]	Davis Run[b]	Panola[b]	Río Icacos[d]
Plagioclase (log mol m^{-2} s^{-1})	-16.1	-16.4	-15.7	-13.0
K-Feldspar (log mol m^{-2} s^{-1})	-16.3	-16.8	nd	nd
Mica (log mol m^{-2} s^{-1})	nd	nd	-16.4[c]	-15.0

[a]This study, [b]White et al. (2001), [c]White et al. (2002), [d]Buss et al. (2008).

Table 1: Site locations and environmental data

Site	Location	MAT (°C)	MAP (mm yr^{-1})	CWR (m Myr^{-1})	Erosion (m Myr^{-1})	Regolith Depth (m)	Lithology
Curacavi[a]	Chile	16	380	4.5	40.5 ± 22.5	>33	Granodiorite
Davis Run[b,c]	Virginia, USA	10	1040	4	8.75 ± 4.25	11	Granodiorite
Hakgala[d]	Sri Lanka	16	2013	11	11	6	Granitic Gneiss
Lysina[e,f]	Czech Republic	5	950	7.1	63	2.6	Leucogranite
Nsimi[g,h]	Cameroon	26	1700	2.8	1.9	38	Granite
Panola[b,c]	Georgia, USA	17	1240	7	8.75 ± 4.25	4.3	Granodiorite
Río Icacos[i,j,k]	Puerto Rico	22	4200	43	43	5	Tonalite

[a]Vázquez et al. (2016) [b]White et al. (2001), [c]Brantley et al. (2017), [d]Hewawasam et al. (2013), [e]Krám et al. (2012), [f]Dannhaus et al. (2018), [g]Braun et al. (2005), [h]Braun et al. (2012), [i]White and Blum (1995),[j]Chabaux et al. (2013),[k]Buss et al. (2017). MAT – Mean Annual Temperature, MAP – Mean Annual Precipitation, CWR – Chemical Weathering Rate (whole rock).

Table 2: Lysina bulk elemental chemistry[a]

Depth (m)	SiO_2 (wt %)	Al_2O_3 (wt %)	CaO (wt %)	Fe_2O_3 (wt %)	FeO[d] (wt %)	K_2O (wt %)	Li_2O (wt %)	MgO (wt %)	Na_2O (wt %)	TiO_2 (wt %)	CIA	Rock Type
Detection Limit	**0.01**	**0.01**	**0.01**	**0.01**	**0.1**	**0.01**	**0.0001**	**0.01**	**0.01**	**0.01**	**-**	**-**
0.15	nd[e]	9.0	0.11	0.82	nd[e]	2.01	0.10	0.10	1.61	0.23	54.9	R[f]
0.30	nd	11.7	0.09	0.93	nd	2.68	0.17	0.11	2.08	0.28	55.1	R
0.45	nd	12.4	0.10	1.62	nd	2.64	0.16	0.17	1.94	0.26	57.4	R
0.60	nd	13.7	0.15	2.24	nd	2.70	0.17	0.29	1.95	0.27	59.3	R
0.75	nd	12.9	0.10	2.06	nd	2.72	0.13	0.21	1.99	0.32	57.8	R
0.90	nd	12.3	0.18	1.65	nd	2.69	0.17	0.23	1.93	0.18	56.6	R
1.05	nd	14.4	0.24	1.73	nd	3.03	0.17	0.27	2.22	0.19	57.0	R
1.20	nd	13.5	0.26	1.60	nd	2.73	0.19	0.29	1.96	0.24	57.8	R
1.35	nd	16.6	0.19	1.28	nd	3.32	0.23	0.22	2.27	0.19	59.4	R
1.50	nd	15.2	0.18	1.22	nd	3.18	0.21	0.19	2.15	0.20	58.6	R
1.65	nd	11.0	0.12	1.21	nd	2.38	0.13	0.15	1.73	0.17	57.0	R
1.80	nd	12.5	0.10	1.17	nd	2.65	0.17	0.16	1.92	0.18	57.7	R
1.85[b]	72.1	13.7	0.67	1.77	1.6	4.20	0.17	0.55	1.19	0.08	64.4	R
2.10	nd	14.1	0.10	1.22	nd	2.97	0.18	0.19	2.19	0.22	57.7	R
2.40	nd	13.5	0.10	1.21	nd	2.86	0.19	0.18	2.07	0.21	57.8	R
2.65	nd	15.9	0.30	1.35	nd	3.27	0.22	0.22	2.41	0.10	57.3	LG
2.77[b]	75.1	13.4	0.35	1.53	1.4	4.64	0.15	0.15	2.49	0.07	58.0	LG
3.10	nd	14.3	0.21	1.36	nd	3.01	0.20	0.55	1.43	0.08	61.6	LG
3.40	nd	13.9	0.24	1.30	nd	2.74	0.21	0.68	1.14	0.08	63.8	LG

3.68	nd	13.3	0.23	1.30	nd	3.02	0.22	0.21	2.05	0.09	56.0	LG
4.20	nd	13.8	0.34	1.20	nd	3.25	0.21	0.13	2.34	0.08	54.0	LG
4.30[b]	73.5	13.9	0.52	1.52	1.4	4.54	0.16	0.18	2.52	0.07	57.9	LG
4.65[c]	72.8	14.3	0.50	1.17	1.0	4.66	0.12	0.19	3.29	0.08	55.0	LG
4.70	nd	13.3	0.30	1.25	nd	3.02	0.20	0.16	2.19	0.09	54.2	LG
5.20	nd	13.4	0.30	1.18	nd	3.14	0.20	0.15	2.28	0.06	54.1	LG
5.90	nd	13.8	0.34	1.13	nd	3.27	0.20	0.14	2.30	0.07	57.1	LG
6.17[b]	72.5	13.4	0.42	1.24	1.2	4.69	0.16	0.15	2.67	0.05	54.7	LG
6.40	nd	13.1	0.29	1.23	nd	3.16	0.23	0.16	2.08	0.08	53.9	LG
6.80	nd	13.6	0.26	1.10	nd	3.48	0.21	0.15	2.22	0.07	52.9	LG
7.10[c]	74.7	13.1	0.42	1.17	1.1	4.54	0.13	0.14	2.99	0.07	54.3	LG
7.45	nd	13.4	0.39	1.15	nd	3.24	0.23	0.18	2.39	0.07	52.7	LG
7.95	nd	13.7	0.35	1.20	nd	2.97	0.23	0.17	2.42	0.07	53.0	LG
8.45	nd	9.7	0.23	0.87	nd	2.38	0.18	0.09	1.77	0.04	53.0	LG
8.90	nd	13.4	0.38	1.14	nd	3.00	0.23	0.12	2.54	0.06	53.0	LG
9.40	nd	13.6	0.35	1.35	nd	3.30	0.27	0.12	2.43	0.07	52.8	LG
10.00	nd	13.2	0.31	0.99	nd	3.02	0.22	0.10	2.51	0.06	53.1	LG
10.40	nd	13.1	0.38	1.03	nd	3.02	0.22	0.14	2.45	0.06	53.1	LG
11.00	nd	12.8	0.39	0.92	nd	2.80	0.21	0.15	2.43	0.06	52.7	LG
11.45	nd	13.1	0.46	0.92	nd	2.88	0.21	0.15	2.41	0.06	52.8	LG
11.90	nd	12.9	0.36	1.00	nd	2.89	0.22	0.11	2.51	0.06	52.4	LG
12.45	nd	12.8	0.38	1.07	nd	2.98	0.24	0.13	2.39	0.06	53.0	LG
12.65[c]	74.3	13.3	0.63	1.04	1.0	3.97	0.12	0.16	3.08	0.07	53.0	LG

13.00	nd	13.1	0.49	1.07	nd	3.04	0.21	0.15	2.39	0.06	53.3	LG
13.45	nd	13.4	0.38	1.03	nd	2.98	0.23	0.12	2.57	0.06	57.0	LG
14.00	nd	14.4	0.48	0.95	nd	3.18	0.23	0.14	2.70	0.05	52.9	LG
14.40	nd	13.3	0.37	1.24	nd	3.06	0.28	0.18	2.41	0.08	53.2	LG
14.64[b]	71.9	14.3	0.46	1.05	1.1	4.35	0.14	0.12	3.44	0.05	52.2	LG
15.04	nd	13.1	0.41	0.88	nd	3.05	0.20	0.15	2.39	0.05	52.9	LG
15.35	nd	14.0	0.42	0.94	nd	3.07	0.22	0.18	2.62	0.06	53.3	LG
15.90	nd	13.2	0.78	1.00	nd	2.94	0.24	0.19	2.26	0.05	53.5	LG
16.35	nd	13.4	0.36	0.98	nd	3.17	0.22	0.12	2.47	0.06	55.1	LG
16.95	nd	13.9	0.40	1.03	nd	3.19	0.25	0.13	2.49	0.06	54.5	LG
17.45	nd	13.2	0.38	1.17	nd	3.16	0.27	0.15	2.24	0.07	54.4	LG
17.90	nd	15.1	0.45	0.94	nd	3.38	0.27	0.21	2.36	0.05	54.1	LG
18.25[c]	71.4	14.9	1.25	0.87	0.7	3.55	0.17	0.28	2.54	0.03	59.2	LG
18.40	nd	14.1	0.46	1.01	nd	3.19	0.27	0.22	2.26	0.06	54.3	LG
18.95	nd	14.9	0.43	1.07	nd	3.50	0.30	0.19	2.38	0.06	61.0	AFG
19.45	nd	14.5	0.60	1.28	nd	3.94	0.34	0.26	1.80	0.05	58.1	AFG
20.05	nd	15.4	0.95	1.46	0.8	2.93	0.40	0.22	2.43	0.06	65.0	AFG
20.22[b]	75.6	13.4	2.03	1.01	nd	3.32	0.27	0.22	0.92	0.03	50.0	AFG
20.45	nd	11.2	0.55	1.06	nd	1.94	0.26	0.21	1.47	0.05	58.1	AFG
20.90	nd	12.4	0.47	1.68	nd	2.23	0.40	0.16	0.75	0.07	65.0	AFG
21.40	nd	12.1	1.65	0.85	nd	2.27	0.24	0.16	1.82	0.03	50.0	AFG
22.05	nd	13.6	0.51	0.87	nd	2.82	0.27	0.27	1.64	0.04	58.1	AFG
22.35[c]	65.4	18.6	0.63	1.09	0.8	6.97	0.16	0.31	1.53	0.07	62.4	AFG

22.45	nd	13.1	0.45	0.67	nd	2.68	0.20	0.25	1.77	0.03	57.4	AFG
22.95	nd	18.4	0.71	0.98	nd	5.47	0.28	0.09	0.26	0.04	61.2	AFG
23.45	nd	13.7	0.55	0.87	nd	3.05	0.20	0.16	2.38	0.05	53.4	AFG
23.68[b]	69.5	15.9	0.80	1.31	1.1	5.77	0.22	0.13	3.10	0.05	56.3	AFG
23.95	nd	12.2	0.75	0.88	nd	2.77	0.15	0.13	1.99	0.03	52.4	AFG
24.45	nd	14.4	1.02	1.57	nd	3.31	0.35	0.19	2.30	0.08	51.8	AFG
24.95	nd	13.6	0.58	1.10	nd	3.06	0.26	0.13	2.43	0.05	52.8	AFG
25.63[b]	73.9	13.9	0.45	1.63	1.5	3.95	0.19	0.22	3.03	0.07	59.2	AFG
26.00[c]	69.5	15.4	0.54	1.09	1.1	6.86	0.16	0.23	2.54	0.09	55.0	AFG
27.75[c]	71.4	22.9	0.51	1.82	1.5	5.70	0.30	0.23	2.40	0.15	54.8	AFG
28.75[b]	59.6	22.9	0.57	1.79	1.5	8.67	0.25	0.45	3.07	0.08	59.7	AFG
30.15[c]	72.9	13.6	0.47	1.09	1.0	5.94	0.16	0.20	2.37	0.09	54.9	LG

[a]Lysina bulk chemistry measured using ICP-OES after Li metaborate fusion; Li and other trace elements measured by ICP-MS after multi-acid digest. [b]Samples analysed in this study, and [c]in Štědrá et al. (2016); other samples analysed by Nwaogu (2014). [d]FeO concentrations were measured by titration methods. Detection limits are shown in the second row. [e] SiO_2 and FeO concentrations were not determined by Nwaogu (2014), denoted by nd. [f] Simplified rock types within the Lysina core include *R*(regolith), *LG*(leucogranite), and *AFG*(alkali-feldspar granite). Due to the small volume of apatite within the Lysina core no correction for apatite was applied to the CIA values.

Table 3: Lysina mineralogy[a]

Depth (m)	Quartz (wt%)	Albite (wt%)	K-Feldspar (wt%)	Kaolinite (wt%)	Illite (wt%)	Li-Mica (wt%)	Apatite (wt%)	Density[c] (g cm^{-3})	Notes
1.85	33.4	4.30	15.9	24.9	nd[b]	10.9	0.75	2.53	1.9 % Jarosite
2.77	38.1	24.4	20.5	5.12	4.50	6.92	0.44	2.65	
4.30	29.7	27.0	27.3	6.05	5.05	4.28	0.52	2.47	
6.17	27.5	29.5	29.8	3.02	5.65	2.65	0.80	2.49	
14.64	35.5	30.3	16.8	5.18	5.27	5.72	0.48	2.59	
20.22	40.8	7.33	22.2	18.3	2.84	6.32	0.58	2.59	0.61 % Fe-oxides, fractured
23.68	24.9	25.8	25.0	8.76	1.11	3.33	nd	2.72	3 % fluorite
25.63	30.7	27.8	25.5	2.71	1.95	5.97	nd	2.54	
28.75	10.9	19.9	35.5	12.7	8.04	12.1	0.81	2.52	Heavily fractured

[a]Mineralogical abundances of Lysina samples derived from EDS phase analysis of thin sections and converted to wt % using mineral density values from the literature (Deer et al., 2013). [b] = not detected. [c]Density values were calculated using sample porosity values and literature values of mineral densities. Some minor minerals present (e.g., monazite) are not shown in this table due to low abundance and absence from some samples.

Table 4: Lysina mineral diameters[a]

	Sample Depth (m)	n	Mean Diameter[b,c] (μm)	Max Diameter (μm)	Min Diameter (μm)	Range (μm)
Albite	**1.85**	51	46 ± 4	168	14	154
	2.77	193	102 ± 4	323	18	305
	4.30	147	233 ± 14	1143	47	1096
	6.17	120	232 ± 20	1978	41	1937
	14.64	37	599 ± 89	1843	53	1790
K-feldspar	**1.85**	52	88 ± 7	224	24	200
	2.77	173	100 ± 6	549	21	528
	4.30	109	264 ± 23	1469	40	1429
	6.17	75	252 ± 44	2619	43	2576
	14.64	40	414 ± 62	1743	41	1702
Quartz	**1.85**	53	133 ± 24	1207	33	1174
	2.77	160	144 ± 19	2511	18	2493
	4.30	171	172 ± 10	712	31	681
	6.17	131	192 ± 11	675	49	626
	14.64	21	680 ± 146	2220	32	2188
Li-Mica	**1.85**	29	99 ± 31	928	17	911
	2.77	56	111 ± 12	440	16	424
	4.30	96	142 ± 8	432	30	402
	6.17	65	154 ± 11	438	51	387
	14.64	11	462 ± 155	1869	84	1785

[a]Diameters of the four primary minerals within the Lysina core. [b]Mineral diameters were measured using NSS 3.0. As many of the minerals had an elongated shape, the diameter was estimated as the square root of the sum of the long and short axes of a mineral grain. Secondary clays such as kaolinite had mineral grain sizes too small to accurately measure. [c]Uncertainty for mean diameter values was estimated from standard error calculations.

Table 5: Mineral specific weathering rates

	Lysina[a]	Davis Run[b]	Panola[b]	Río Icacos[d]
Plagioclase (log mol m^{-2} s^{-1})	-16.1	-16.4	-15.7	-13.0
K-Feldspar (log mol m^{-2} s^{-1})	-16.3	-16.8	nd	nd
Mica (log mol m^{-2} s^{-1})	nd	nd	-16.4[c]	-15.0

[a]This study
[b]White et al. (2001)
[c]White et al. (2002)
[d]Buss et al. (2008).

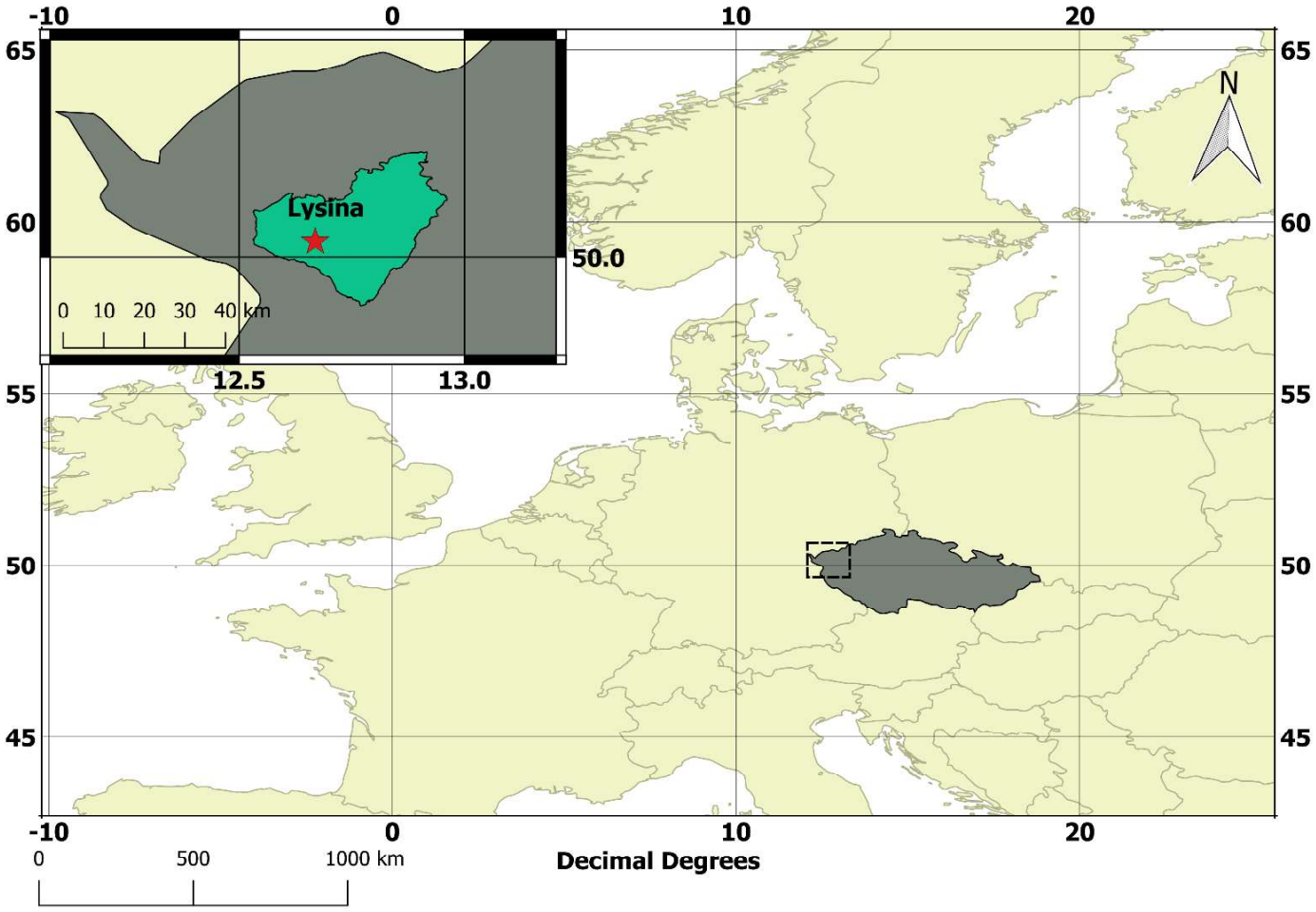

Figure 1: The field study was located in the west (dashed box) of the Czech Republic (dark gray). The inset shows the location of the Lysina catchment (red star) within the Slavkov Forest region (green).

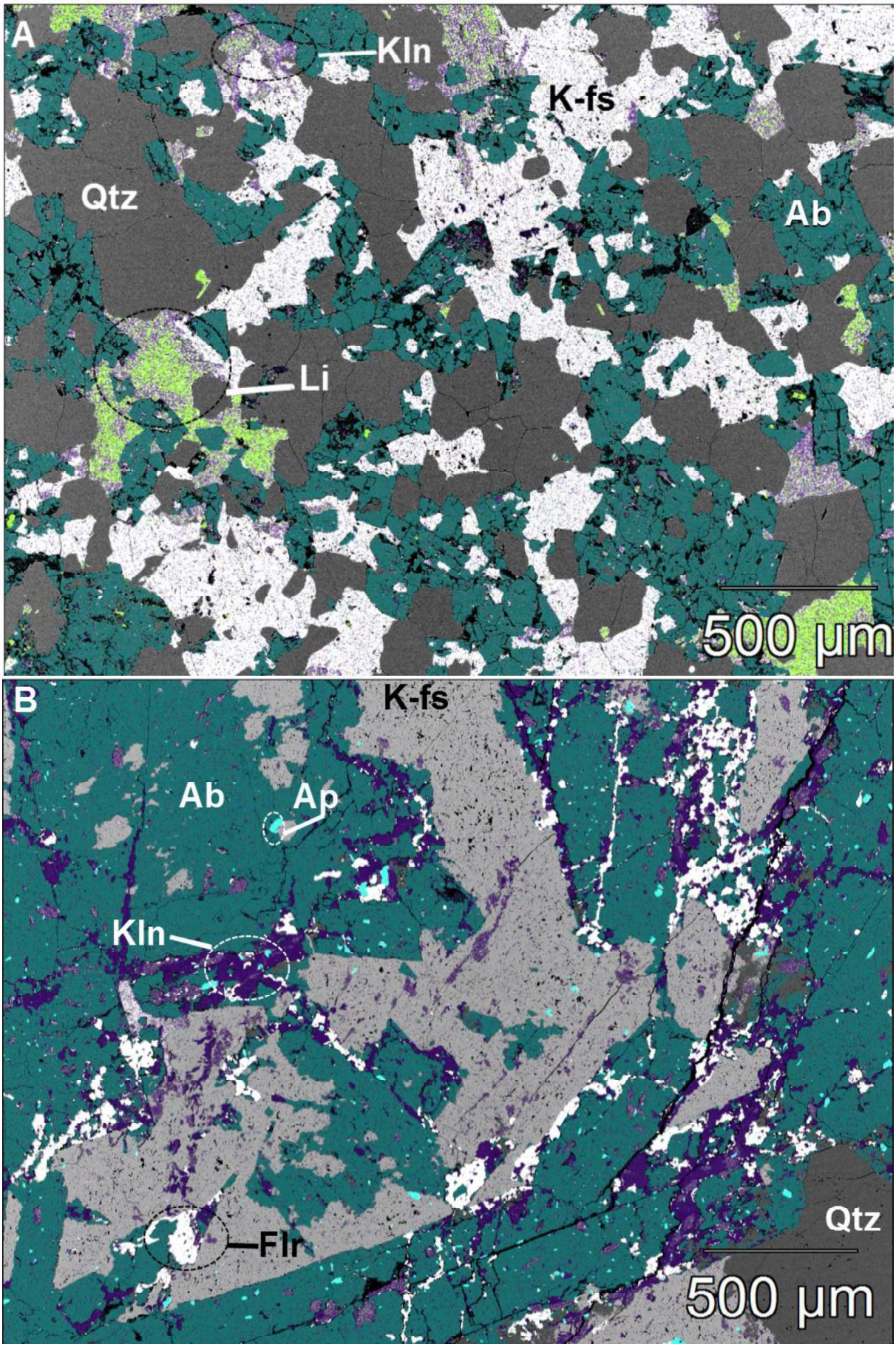
A
Kln
K-fs
Qtz
Ab
Li
500 µm
B
K-fs
Ab
Ap
Kln
Flr
Qtz
500 µm

Figure 2: (A) False colour BSE image of weathering Li-micas from a sample at 6.17 m depth from the Lysina core. Li-micas (Li) are highlighted in green, kaolinite (Kln) is highlighted in purple, and (Ab) albite in blue. The Li-micas maintain distinct mineral grains despite undergoing extensive alteration, as evidenced by the high abundance of clays within the mineral grains. Albite also shows extensive alteration and grains are beginning to lose their structure. Also shown are (Qtz) quartz in dark grey and (K-fs) K-feldspar grains in lighter grey. (B) False colour BSE image of fluorite grains (flr, white) occupying pore spaces within albite grains (Ab, blue) with kaolinite (Kln, purple) in the Lysina core from 23.68 m depth. Also shown are apatite (Ap, cyan), K-feldspar (K-fs, light grey) and quartz (Qtz, dark grey). Fluorite grains are restricted to the more heavily weathered albite crystals and are absent from the less weathered K-feldspar and quartz grains, suggesting that fluorite formation occurred post albite weathering.

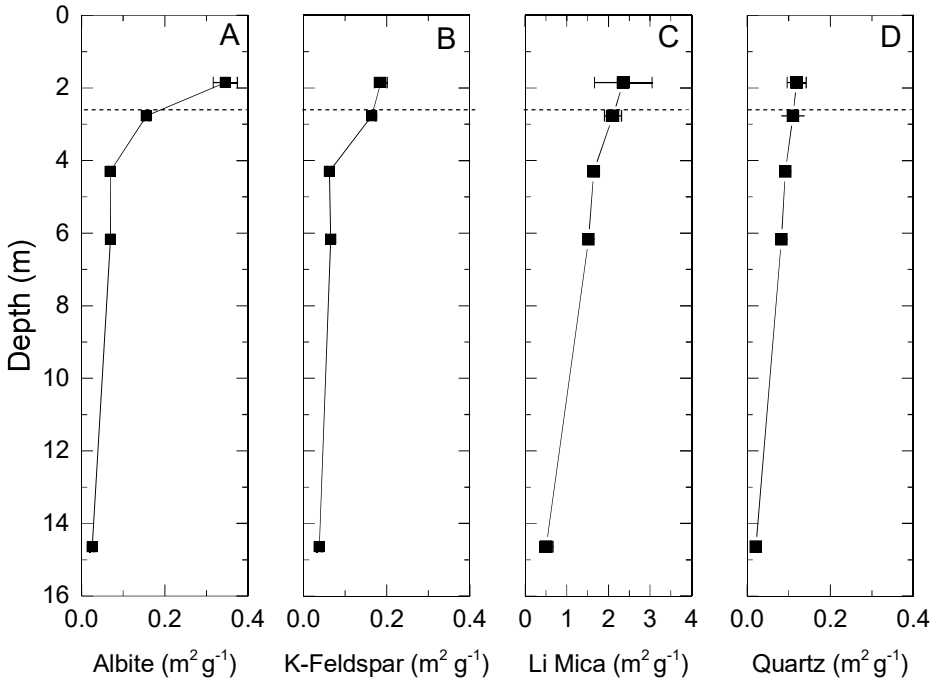

Figure 3: Calculated geometric surface areas (Eq. 6) for the four key minerals within the Lysina profile. Dotted lines indicate the regolith-bedrock boundary. Note differing x-axis scale on panel C due to larger Li-mica surface area values. Uncertainty values were derived from standard error calculations on mineral diameters in each sample. Mineral surface areas increase relative to the parent sample in the upper 6.17 m of the core, particularly for (A) albite and (B) K-feldspar. (D) Quartz shows minimal significant changes in mineral surface areas through the profile.

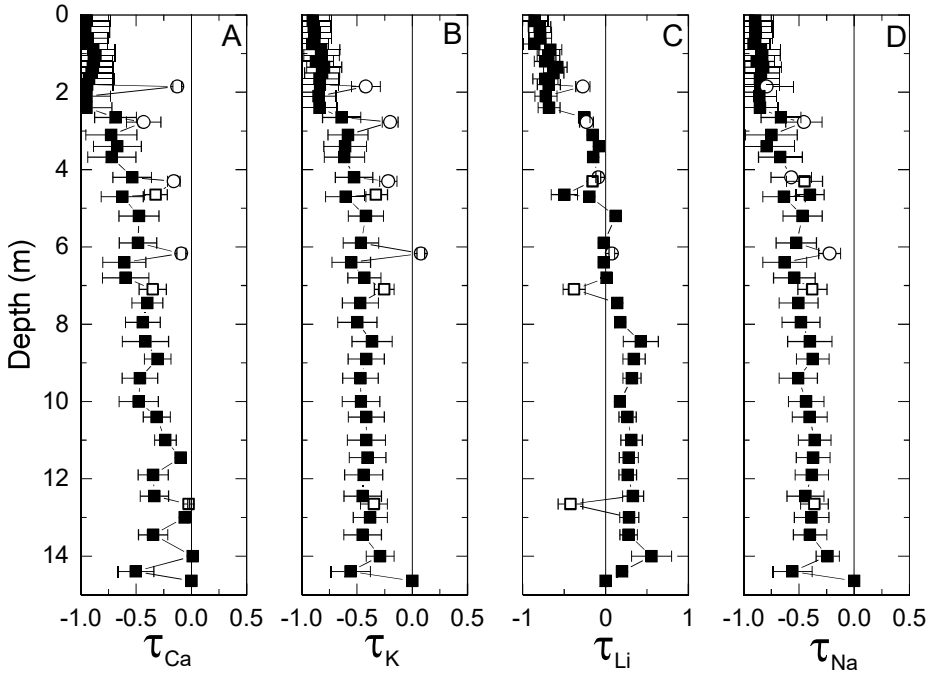

Figure 4: Mass transfer coefficient (τ, Eq. 1) of select mobile elements within the Lysina profile, normalised to Ti. Black squares indicate data from Nwaogu (2014), open squares indicate data from Štědrá et al. (2016), while open circles indicate data produced in this study. Note differing x-axis scale on panel c due to enrichment of Li relative to the parent sample. All elements show a general depletion trend above 14.64 m except Li which shows depletion above 5 m.

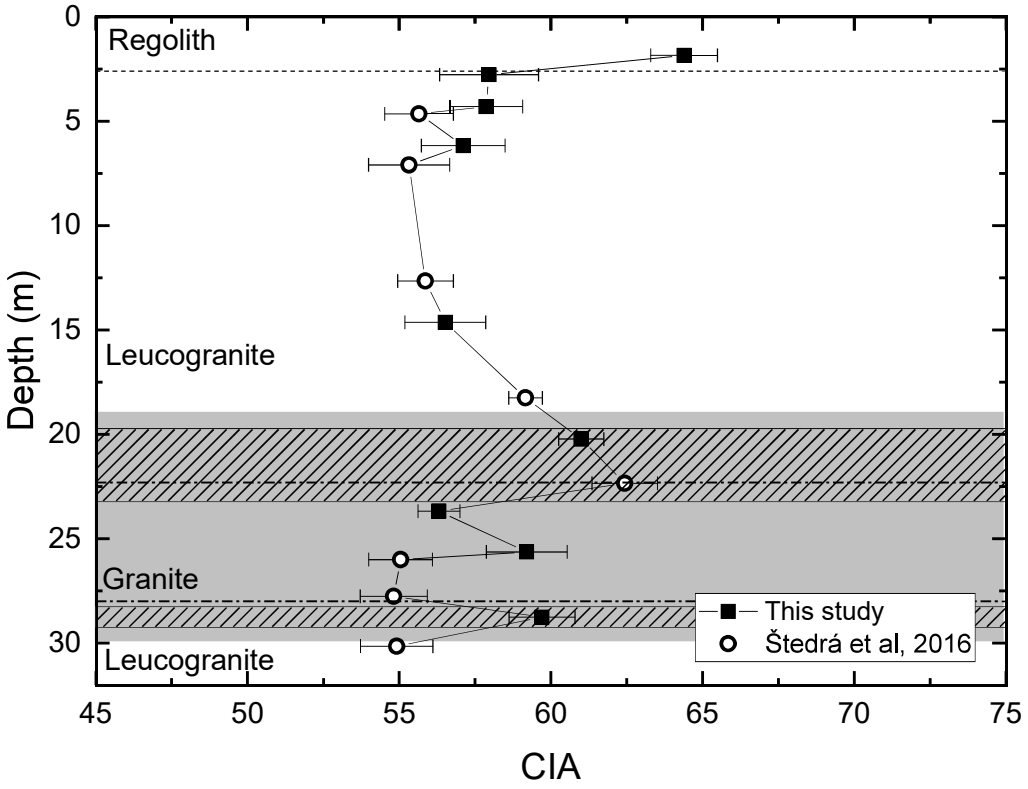

Figure 5: The chemical index of alteration (CIA, Eq. 3) with depth in the Lysina core. The Lysina profile shows only limited weathering (CIA = 54-64); unweathered granites typically have CIA values of 40-55 (Bahlburg and Dobrzinski, 2011). Open circles indicate CIA values calculated using bulk geochemistry data from Štědrá et al. (2016). Error bars represent potential range of CIA values based on uncertainties in oxide abundance, propagated through all calculations and reported to 1 standard error. Shaded area indicates hydrothermally altered zone while dotted-dashed lines indicate boundaries of a zone of lithological variation identified by Štědrá et al. (2016) between 22.3 and 28 m depth. The hashed shaded area indicates zones of the core which have a higher degree of fracturing.

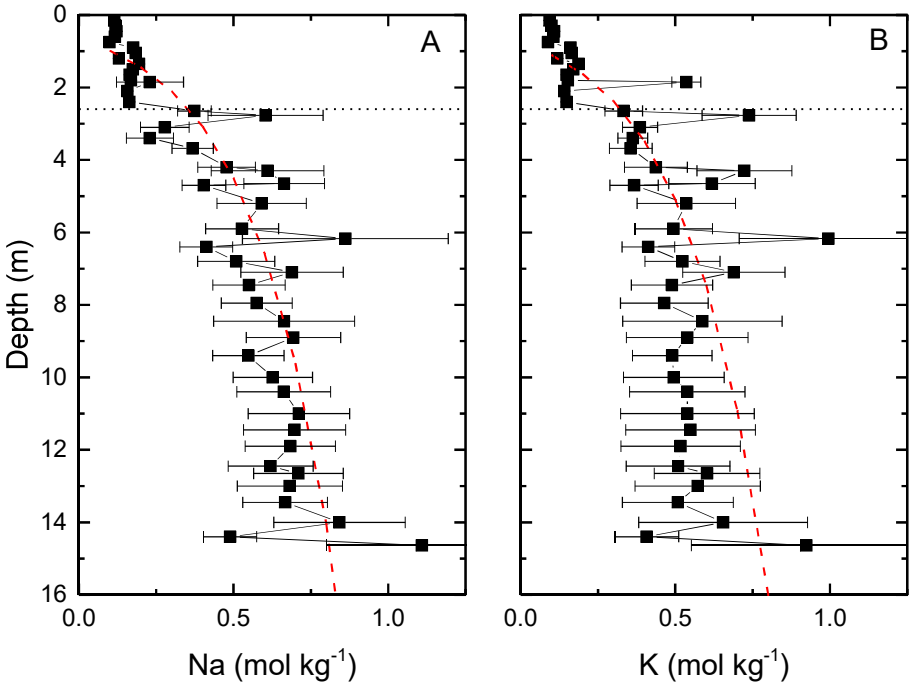

Figure 6: Lysina elemental concentrations (C_w) normalised to Ti (Eq.4) in the upper 14.64 m of the Lysina core. Dashed red lines show gradients used in weathering rate calculations (Eq. 5) and dotted lines indicate the bedrock-regolith boundary. (A) Na shows gradual loss from 14.64 m to 4.3 m and more significant losses above 4.3 m. (B) K shows initial loss between 14.64 m and 14.4 m but remains relatively stable until 4.3 m, above which loss occurs towards the surface.

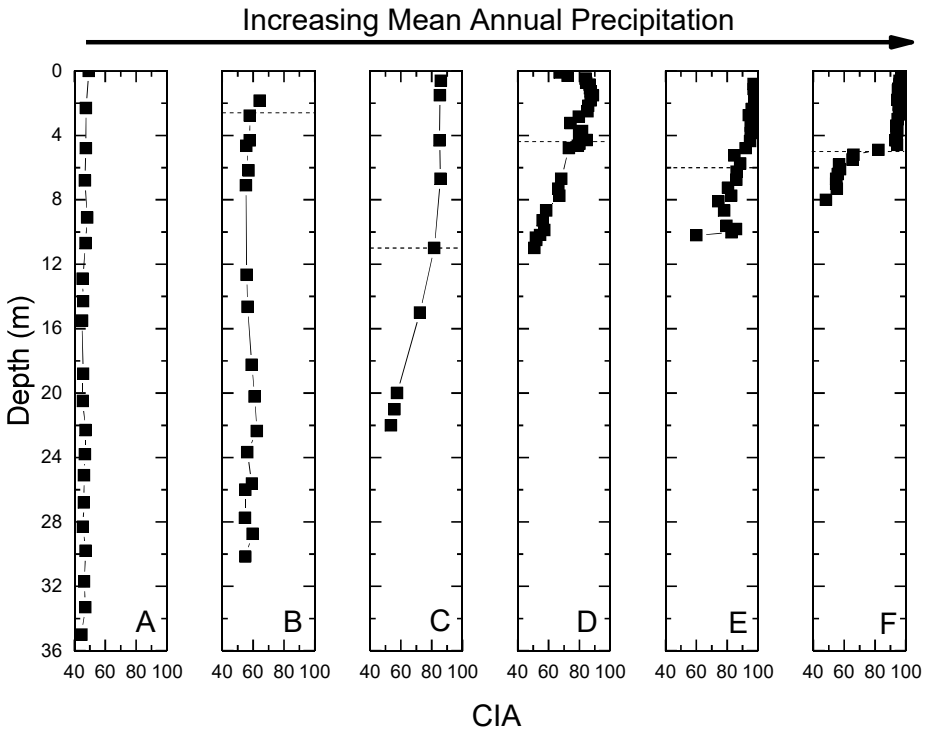

Figure 7: Chemical Index of Alteration (CIA, Eq. 3) with depth for (A) Curacavi, (B) Lysina, (C) Davis Run, (D) Panola, (E) Hakgala, and (F) Río Icacos in order of increasing MAP. Dotted lines indicate the bedrock-regolith boundaries. The Curacavi profile is entirely saprolite and fresh bedrock was not reached. Curacavi and Lysina show deep profiles with only limited changes in CIA values, while Davis Run, Panola, and Hakgala show clear transitions from fresh to more highly weathered material over 5-10 m distances. Río Icacos displays a sharp transition from fresh to nearly totally depleted material over only 1 m distance. Nsimi is excluded due to non-continuous sampling methods used on that profile.

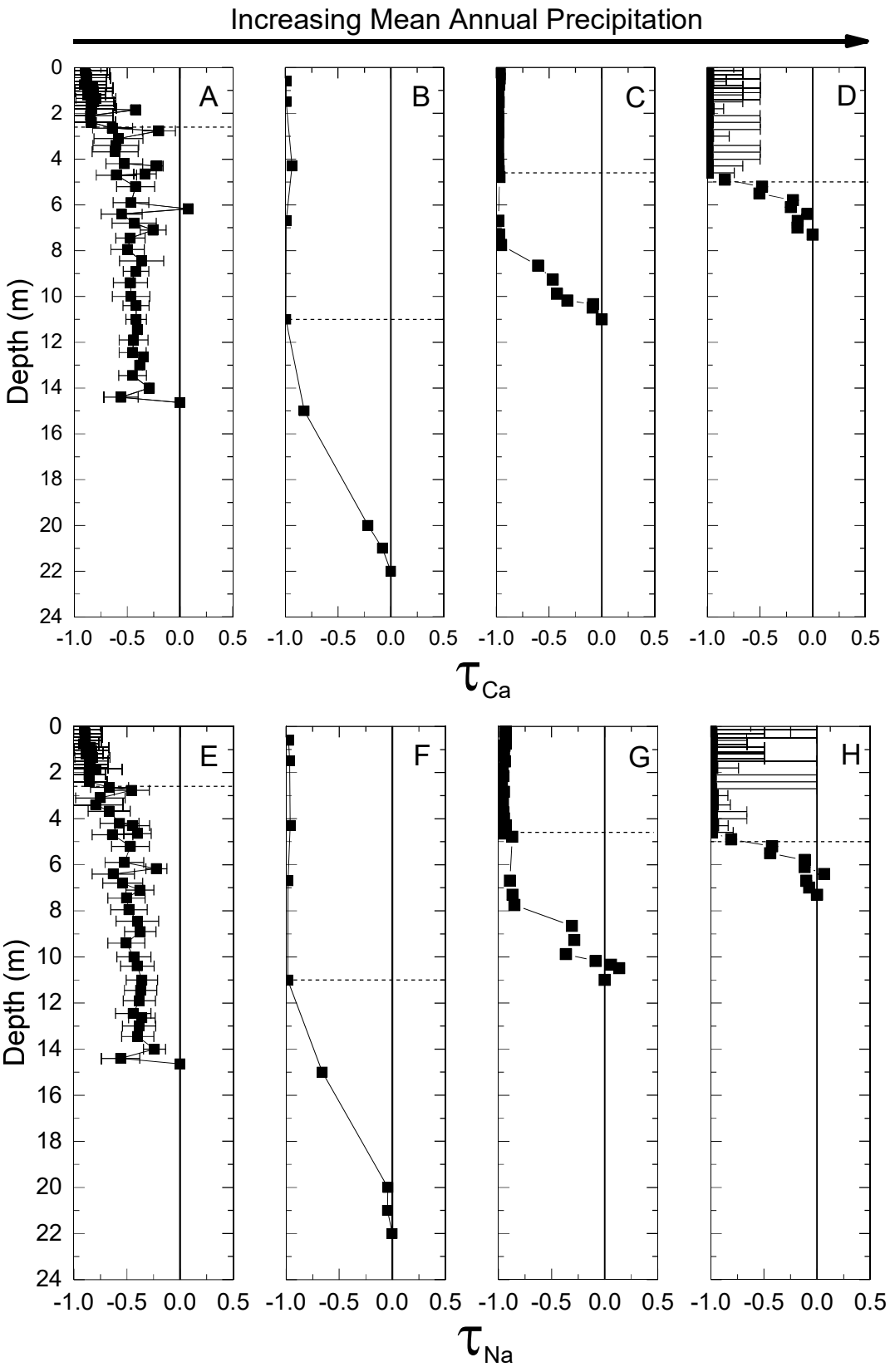
Increasing Mean Annual Precipitation
A
B
C
D
E
F
G
H
Depth (m)
0
2
4
6
8
10
12
14
16
18
20
22
24
-1.0
-0.5
0.0
0.5
τ_{Ca}
τ_{Na}

Figure 8: Ca mass transfer, τ_{Ca} (Eq.1), with depth, normalised to Ti for (A) Lysina, (B) Davis Run, (C) Panola, (D) Río Icacos, and Na mass transfer coefficients normalised to Ti for (E) Lysina, (F) Davis Run, (G) Panola, and (H) Río Icacos. The dotted line indicates the regolith-bedrock boundary. Uncertainty estimates are unavailable for Davis Run and Panola.

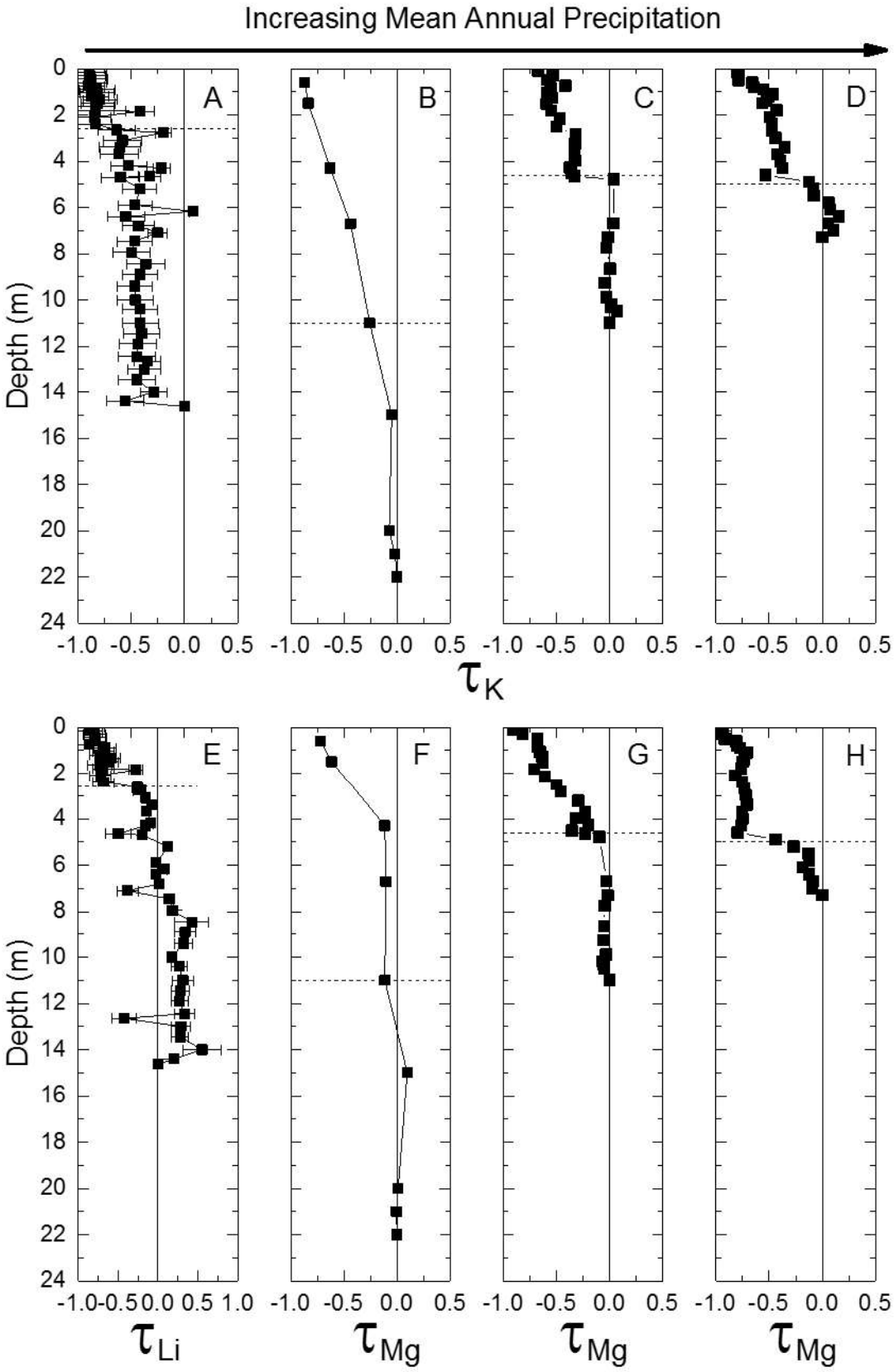

Figure 9: K mass transfer , τ_K (Eq. 1), with depth, normalised to Ti for (A) Lysina, (B) Davis Run, (C) Panola, (D) Río Icacos, and Li or Mg mass transfer coefficients normalised to Ti (τ_{Li} for Lysina and τ_{Mg} for the other sites)

for (E) Lysina, (F) Davis Run, (G) Panola, and (H) Río Icacos, representing mica weathering fronts at each site. Note differing x-axis scale on panel e to show enrichment of Li in the Lysina profile. Dotted line indicates the regolith-weathering boundary. Uncertainty estimates are unavailable for Davis Run and Panola. Uncertainty values are sufficiently small at Río Icacos to be contained within the symbols.

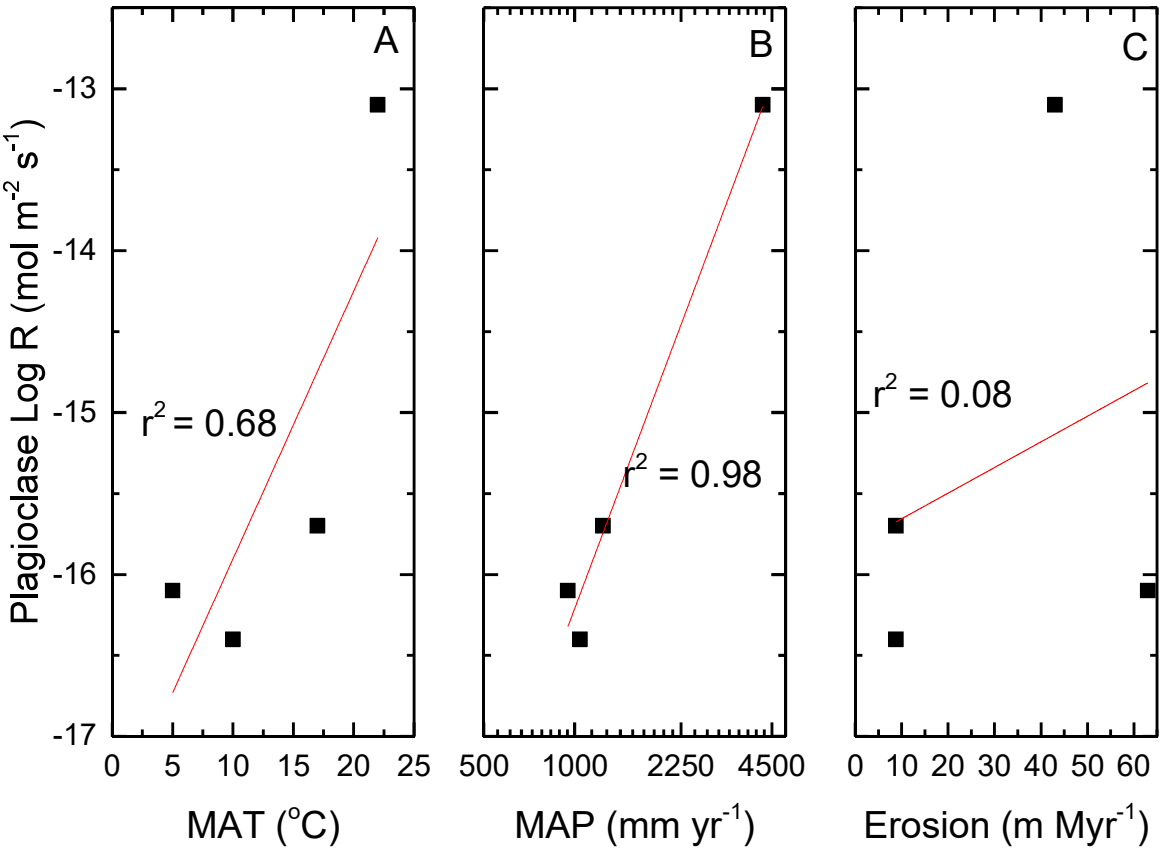

Figure 10: Plagioclase weathering rates from the four primary sites plotted against (A) mean annual temperature, (B) mean annual precipitation, and (C) erosion rates (Tables 1 and 5). Plagioclase rates show a stronger correlation with MAP (r^2 = 0.98, p = 0.009) than MAT (r^2 = 0.68, p = 0.18) which shows inconsistent changes in rates over similar values (i.e., a decrease in rates over a 5 °C increase between Lysina and Davis Run, and three orders of magnitude increase over a 5 °C increase between Panola and Río Icacos). Erosion rates show no clear correlation with plagioclase weathering rates in this sample. Due to the small sample size, confidence in these correlations is very low.

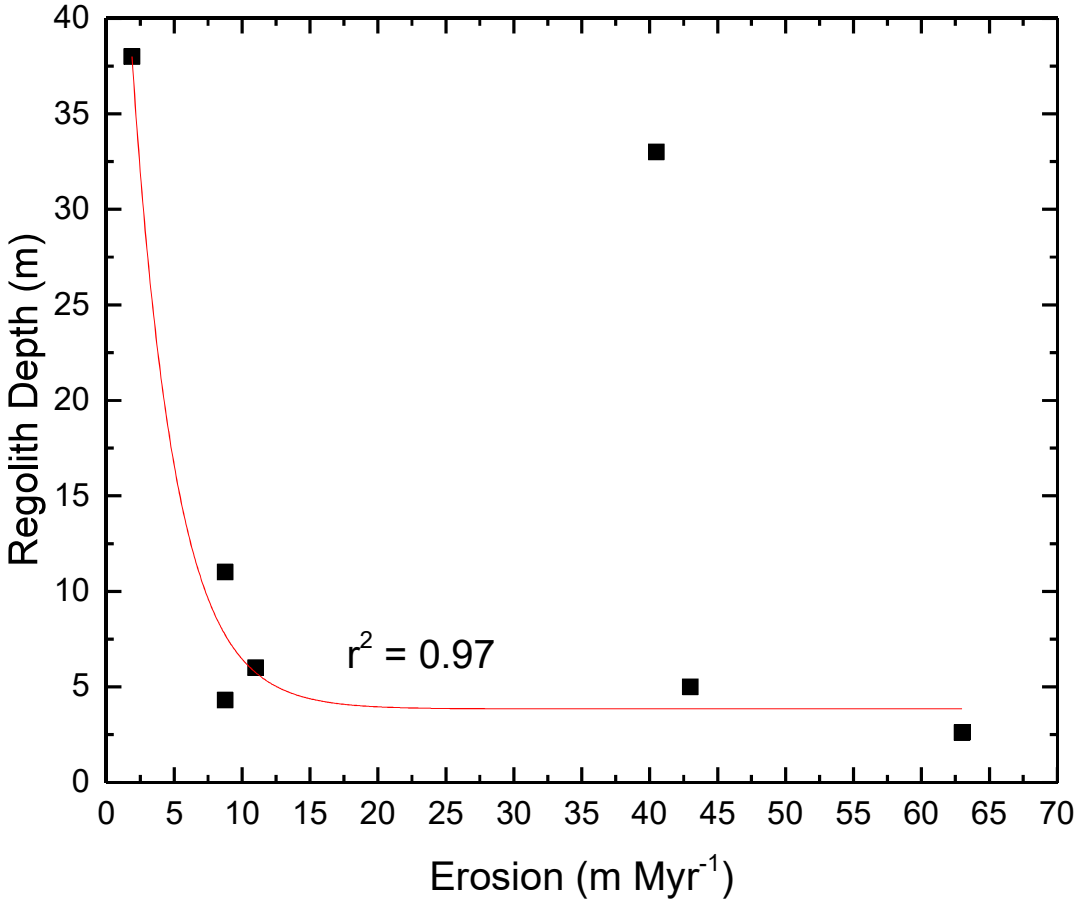

Figure 11: Regolith depth plotted against erosion rates for all sites (Table 1). Regolith depth shows a general decrease where erosion rates are highest, although Curacavi (Erosion Rate = 40.5 m Myr^{-1}, Depth = 33 m) is an outlier in this trend. An exponential trendline returns a correlation of r^2=0.97 (significant at the 95% confidence level) if the outlier (Curacavi) is excluded.

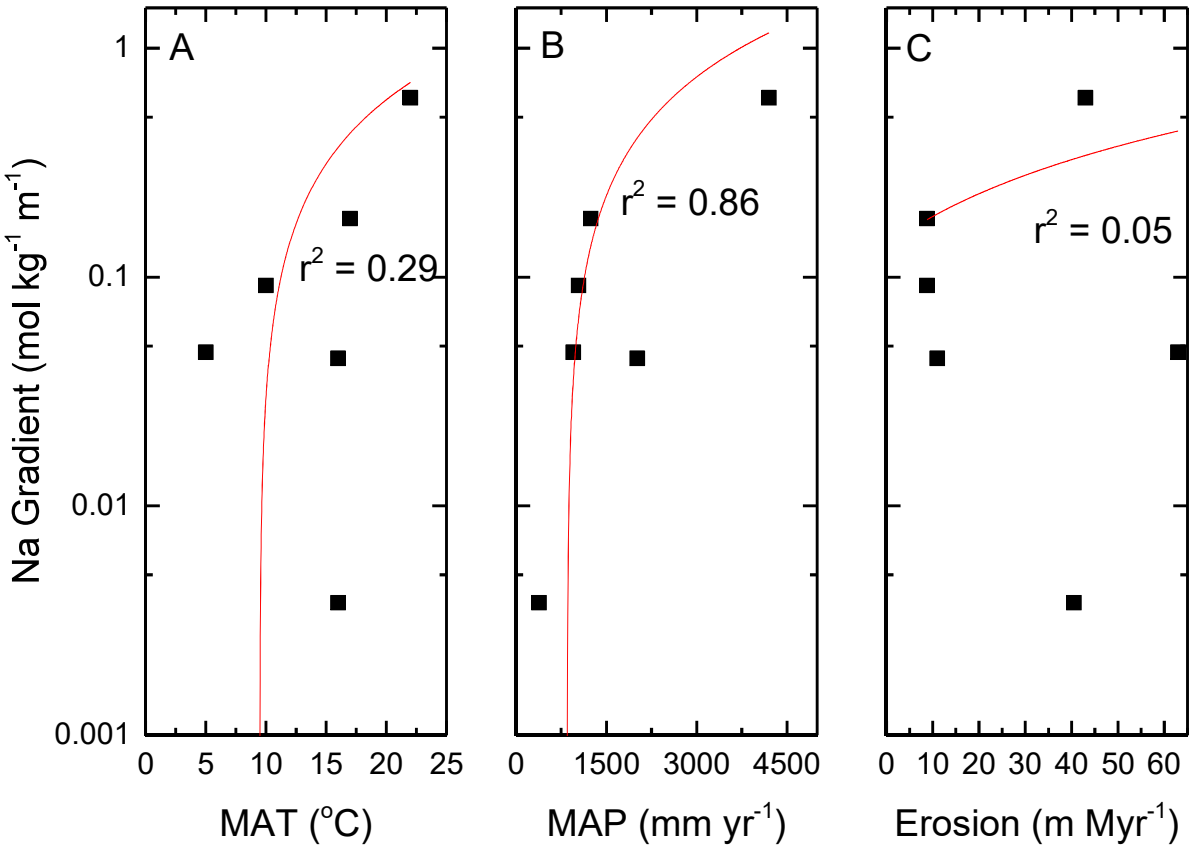

Figure 12: Na weathering gradients (as a proxy for plagioclase weathering) correlated against (A) MAT, (B) MAT, and (C) erosion rates at six of the field sites (Table 1). Nsimi is excluded due to non-continuous sampling of that profile preventing the calculation of a gradient value. Na weathering gradients strongly correlate with MAP (r^2 = 0.86, p = 0.007), while correlations are much weaker for MAT and erosion rates.

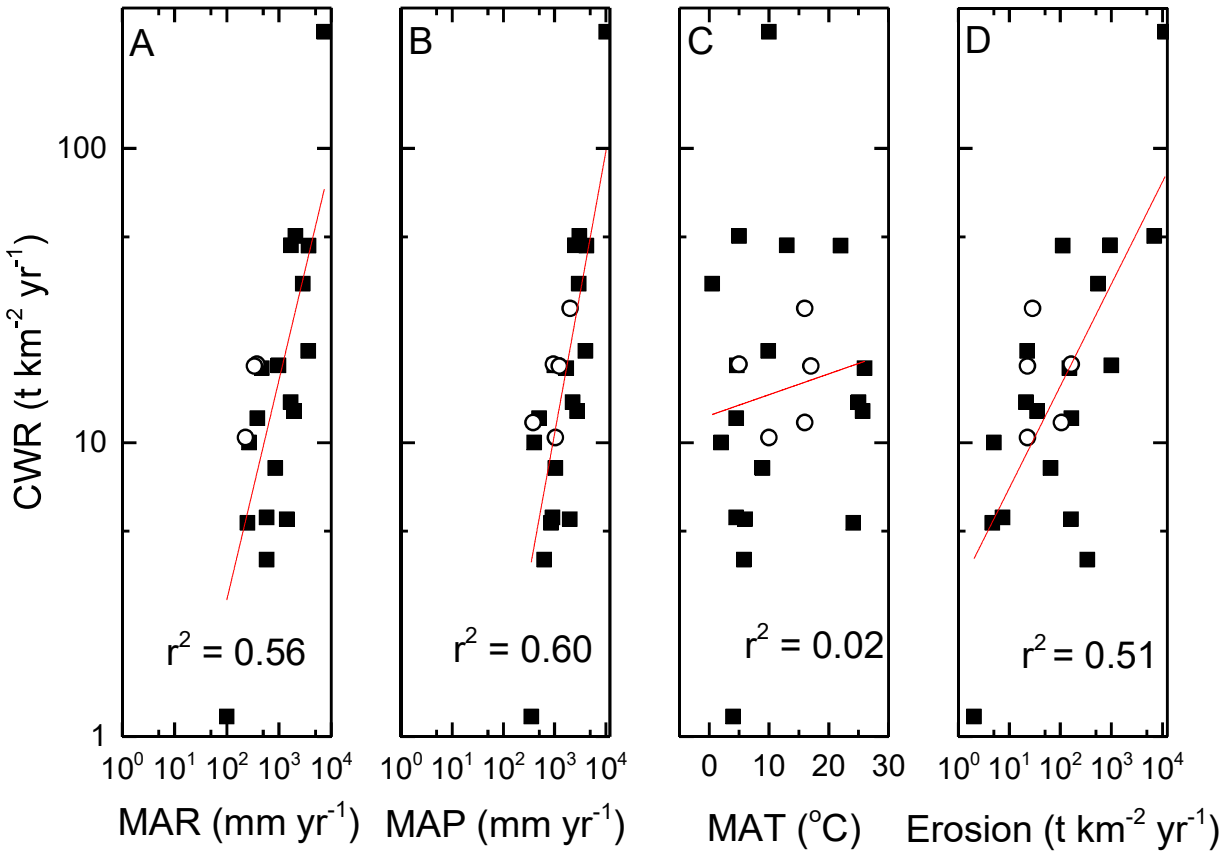

Figure 13: Chemical weathering rates (CWR) from 18 sites plotted against (A) mean annual runoff (MAR), (B) mean annual precipitation, (C) mean annual temperatures (MAT), and (D) erosion rates, using data compiled by West et al. (2005) (black squares) and sites from this study (open circles) where data are available. Note that the Nsimi and Río Icacos catchments are included within the West et al. (2005) dataset. The strongest correlations are between CWR and MAP/MAR, with a slightly weaker correlation between CWR and erosion rates. MAT shows no significant correlation with CWR, suggesting that MAR, MAP and erosion are much stronger controls on CWR. The majority of the sites are granitic or granitic/metamorphic, along with four sites with purely metamorphic lithologies.

Appendix A:

Table A1: Lysina mass transfer (Equation 1)[a].

Depth (m)	Ca τTi	K τTi	Li τTi	Na τTi
0.15	-0.95 ± 0.21	-0.90 ± 0.17	-0.85 ± 0.16	-0.90 ± 0.17
0.30	-0.97 ± 0.23	-0.89 ± 0.15	-0.80 ± 0.14	-0.89 ± 0.14
0.45	-0.96 ± 0.22	-0.88 ± 0.16	-0.79 ± 0.14	-0.89 ± 0.16
0.60	-0.94 ± 0.18	-0.89 ± 0.15	-0.79 ± 0.14	-0.90 ± 0.15
0.75	-0.97 ± 0.21	-0.90 ± 0.15	-0.86 ± 0.14	-0.91 ± 0.15
0.90	-0.89 ± 0.19	-0.83 ± 0.17	-0.67 ± 0.14	-0.84 ± 0.17
1.05	-0.87 ± 0.18	-0.82 ± 0.16	-0.69 ± 0.14	-0.83 ± 0.16
1.20	-0.88 ± 0.17	-0.87 ± 0.16	-0.73 ± 0.13	-0.88 ± 0.16
1.35	-0.89 ± 0.19	-0.80 ± 0.16	-0.58 ± 0.12	-0.82 ± 0.16
1.50	-0.90 ± 0.19	-0.82 ± 0.16	-0.63 ± 0.12	-0.84 ± 0.16
1.65	-0.93 ± 0.22	-0.84 ± 0.18	-0.73 ± 0.15	-0.85 ± 0.18
1.80	-0.94 ± 0.23	-0.83 ± 017	-0.68 ± 0.14	-0.85 ± 0.17
1.85	-0.13 ± 0.04	-0.42 ± 0.13	-0.27 ± 0.09	-0.79 ± 0.25
2.10	-0.95 ± 0.22	-0.85 ± 0.16	-0.72 ± 0.13	-0.86 ± 0.16
2.40	-0.95 ± 0.23	-0.84 ± 0.23	-0.68 ± 0.16	-0.85 ± 0.16
2.65	-0.69 ± 0.19	-0.64 ± 0.17	-0.26 ± 0.07	-0.66 ± 0.18
2.77	-0.43 ± 0.16	-0.20 ± 0.07	-0.23 ± 0.08	-0.46 ± 0.16
3.10	-0.72 ± 0.23	-0.58 ± 0.18	-0.15 ± 0.05	-0.75 ± 0.23
3.40	-0.67 ± 0.21	-0.61 ± 0.19	-0.08 ± 0.03	-0.79 ± 0.25
3.68	-0.72 ± 0.22	-0.61 ± 0.18	-0.15 ± 0.04	-0.67 ± 0.20
4.20	-0.54 ± 0.17	-0.53 ± 0.17	-0.09 ± 0.03	-0.57 ± 0.18
4.30	-0.16 ± 0.06	-0.22 ± 0.08	-0.16 ± 0.06	-0.45 ± 0.16
4.65	-0.32 ± 0.10	-0.33 ± 0.11	-0.50 ± 0.16	-0.40 ± 0.13
4.70	-0.63 ± 0.19	-0.60 ± 0.18	-0.19 ± 0.06	-0.64 ± 0.19
5.20	-0.47 ± 0.18	-0.42 ± 0.16	0.12 ± 0.05	-0.47 ± 0.18
5.90	-0.48 ± 0.17	-0.46 ± 0.16	-0.02 ± 0.01	-0.52 ± 0.18
6.17	-0.09 ± 0.04	0.08 ± 0.03	0.08 ± 0.03	-0.22 ± 0.10
6.40	-0.61 ± 0.19	-0.55 ± 0.17	-0.02 ± 0.01	-0.63 ± 0.20
6.80	-0.59 ± 0.21	-0.43 ± 0.15	0.01 ± 0.005	-0.54 ± 0.19
7.10	-0.35 ± 0.12	-0.25 ± 0.09	-0.38 ± 0.13	-0.38 ± 0.13
7.45	-0.40 ± 0.14	-0.47 ± 0.16	0.14 ± 0.05	-0.50 ± 0.18
7.95	-0.44 ± 0.16	-0.50 ± 0.18	0.18 ± 0.06	-0.48 ± 0.17
8.45	-0.42 ± 0.21	-0.36 ± 0.18	0.43 ± 0.21	-0.40 ± 0.20
8.90	-0.31 ± 0.12	-0.42 ± 0.16	0.34 ± 0.13	-0.37 ± 0.15
9.40	-0.47 ± 0.16	-0.47 ± 0.16	0.32 ± 0.11	-0.51 ± 0.17
10.00	-0.48 ± 0.18	-0.46 ± 0.17	0.17 ± 0.06	-0.43 ± 0.16
10.40	-0.31 ± 0.12	-0.42 ± 0.16	0.27 ± 0.10	-0.40 ± 0.16
11.00	-0.24 ± 0.10	-0.42 ± 0.17	0.31 ± 0.13	-0.36 ± 0.15
11.45	-0.10 ± 0.04	-0.40 ± 0.17	0.28 ± 0.12	-0.37 ± 0.15
11.90	-0.35 ± 0.14	-0.44 ± 0.17	0.27 ± 0.11	-0.38 ± 0.15
12.45	-0.34 ± 0.13	-0.45 ± 0.17	0.33 ± 0.13	-0.44 ± 0.17
12.65	-0.02 ± 0.09	-0.35 ± 0.12	-0.42 ± 0.15	-0.36 ± 0.13
13.00	-0.06 ± 0.25	-0.38 ± 0.15	0.29 ± 0.12	-0.39 ± 0.16
13.45	-0.35 ± 0.13	-0.45 ± 0.17	0.28 ± 0.11	-0.40 ± 0.15
14.00	0.01 ± 0.01	-0.29 ± 0.13	0.56 ± 0.24	-0.24 ± 0.10
14.40	-0.50 ± 0.16	-0.56 ± 0.18	0.20 ± 0.06	-0.56 ± 0.18
14.64	0.00	0.00	0.00	0.00

[a]Uncertainty estimated and propagated from geochemical analytical technique detection limits

* Calculated using data from Štědrá et al. (2016).

Table A2: Davis Run mass transfer and CIA[a].

Depth (m)	Ca τTi	K τTi	Mg τTi	Na τTi	CIA
0.60	-0.99	-0.87	-0.72	-0.98	86.0
1.50	-0.99	-0.84	-0.61	-0.97	85.3
4.30	-0.94	-0.63	-0.11	-0.96	85.0
6.70	-0.99	-0.44	-0.10	-0.98	85.7
11.0	-0.99	-0.26	-0.11	-0.98	81.6
15.0	-0.82	-0.05	0.10	-0.66	72.4
20.0	-0.22	-0.07	0.010	-0.04	57.5
21.0	-0.08	-0.02	-0.01	-0.05	55.7
22.0	0	0	0	0	53.6

[a]Calculated from data in Pavich et al. (1989).

Table A3: Panola mass transfer and CIA[a].

Depth (m)	Ca τTi	K τTi	Mg τTi	Na τTi	CIA
0.10	-0.97	-0.67	-0.90	-0.93	67.3
0.30	-0.97	-0.54	-0.82	-0.93	72.5
0.48	-0.97	-0.58	-0.68	-0.93	84.1
0.74	-0.97	-0.42	-0.68	-0.93	84.6
0.84	-0.98	-0.55	-0.68	-0.94	86.7
1.07	-0.98	-0.59	-0.65	-0.95	86.8
1.27	-0.98	-0.54	-0.63	-0.95	87.2
1.52	-0.98	-0.59	-0.63	-0.94	88.8
1.83	-0.98	-0.55	-0.71	-0.96	87.3
2.16	-0.98	-0.47	-0.61	-0.95	85.8
2.51	-0.98	-0.50	-0.50	-0.97	85.3
2.84	-0.98	-0.32	-0.46	-0.95	79.6
3.23	-0.98	-0.32	-0.30	-0.96	74.3
3.73	-0.98	-0.33	-0.23	-0.95	81.8
3.99	-0.98	-0.33	-0.31	-0.95	79.8
4.29	-0.98	-0.37	-0.20	-0.93	84.7
4.52	-0.98	-0.36	-0.36	-0.95	80.1
4.65	-0.98	-0.33	-0.23	-0.95	78.9
4.79	-0.97	0.04	-0.10	-0.87	73.2
6.69	-0.98	0.03	-0.03	-0.89	68.3
7.30	-0.97	-0.01	-0.02	-0.87	66.4
7.75	-0.95	-0.03	-0.05	-0.85	67.1
8.66	-0.60	0.00	-0.05	-0.31	58.5
9.27	-0.47	-0.04	-0.06	-0.29	56.2
9.88	-0.42	-0.03	-0.03	-0.36	57.3
10.18	-0.33	0.01	-0.06	-0.08	54.5
10.34	-0.08	0.01	-0.05	0.06	51.8
10.49	-0.09	0.07	-0.05	0.14	51.9
11.0	0	0	0	0	50.7

[a]Calculated from data in White et al. (2001).

Table A4: Río Icacos mass transfer and CIA[a].

Depth (m)	Ca τTi	K τTi	Mg τTi	Na τTi	CIA
0.15	-0.99 ± 0.33	-0.80 ± 0.04	-0.93 ± 0.08	-1.00 ± 1.00	97.5
0.30	-0.99 ± 0.33	-0.79 ± 0.04	-0.94 ± 0.09	-0.99 ± 0.50	97.1
0.50	-1.00 ± 0.50	-0.79 ± 0.03	-0.92 ± 0.05	-1.00 ± 1.00	97.5
0.60	-0.99 ± 0.17	-0.66 ± 0.02	-0.81 ± 0.02	-0.99 ± 0.33	96.0
0.80	-0.99 ± 0.33	-0.64 ± 0.02	-0.80 ± 0.03	-0.99 ± 0.33	96.0
0.90	-1.00 ± 0.50	-0.55 ± 0.01	-0.77 ± 0.02	-0.99 ± 0.50	96.0
1.10	-1.00 ± 0.50	-0.47 ± 0.01	-0.71 ± 0.02	-0.99 ± 0.50	95.1
1.20	-0.99 ± 0.33	-0.50 ± 0.01	-0.73 ± 0.02	-0.99 ± 0.50	94.9
1.40	-1.00 ± 0.50	-0.52 ± 0.01	-0.73 ± 0.02	-0.99 ± 0.50	95.4
1.50	-1.00 ± 0.33	-0.56 ± 0.01	-0.75 ± 0.02	-1.00 ± 1.00	95.6
1.80	-0.99 ± 0.14	-0.43 ± 0.01	-0.76 ± 0.02	-0.99 ± 0.25	94.4
2.10	-1.00 ± 0.50	-0.49 ± 0.01	-0.82 ± 0.02	-1.00 ± 1.00	95.4
2.40	-1.00 ± 0.50	-0.47 ± 0.01	-0.75 ± 0.03	-1.00 ± 1.00	96.6
2.70	-1.00 ± 0.50	-0.47 ± 0.01	-0.73 ± 0.02	-1.00 ± 1.00	95.6
3.00	-0.99 ± 0.20	-0.44 ± 0.01	-0.72 ± 0.02	-0.98 ± 0.14	94.8
3.40	-1.00 ± 0.50	-0.35 ± 0.01	-0.71 ± 0.02	-0.98 ± 0.17	94.0
3.70	-1.00 ± 0.50	-0.42 ± 0.01	-0.75 ± 0.02	-0.99 ± 0.33	94.6
4.00	-1.00 ± 0.50	-0.39 ± 0.01	-0.75 ± 0.02	-0.99 ± 0.33	94.0
4.30	-0.99 ± 0.33	-0.38 ± 0.01	-0.77 ± 0.02	-0.98 ± 0.14	93.4
4.60	-0.99 ± 0.25	-0.53 ± 0.01	-0.80 ± 0.02	-0.99 ± 0.20	94.4
4.90	-0.83 ± 0.02	-0.13 ± 0.003	-0.44 ± 0.01	-0.81 ± 0.02	82.2
5.20	-0.48 ± 0.01	-0.08 ± 0.002	-0.27 ± 0.01	-0.42 ± 0.01	66.2
5.50	-0.50 ± 0.01	-0.08 ± 0.002	-0.13 ± 0.003	-0.44 ± 0.01	65.4
5.80	-0.19 ± 0.01	0.06 ± 0.002	-0.12 ± 0.004	-0.11 ± 0.003	56.8
6.10	-0.21 ± 0.01	0.07 ± 0.002	-0.18 ± 0.01	-0.12 ± 0.003	57.3
6.40	-0.05 ± 0.002	0.15 ± 0.005	-0.12 ± 0.004	0.07 ± 0.002	55.9
6.70	-0.14 ± 0.004	0.05 ± 0.001	-0.09 ± 0.003	-0.10 ± 0.003	54.9
7.00	-0.14 ± 0.004	0.10 ± 0.003	-0.09 ± 0.003	-0.07 ± 0.002	54.8
7.30	0.00	0.00	0.00	0.00	55.2

[a]Calculated from data in Buss et al. (2017). Uncertainty estimated and propagated from geochemical analytical technique detection limits. Uncertainty values of 1 occur in samples where Na was below detection limit (0.01 wt %).

Table A5: Lysina CIA

Depth (m)	CIA

1.85	64.4 ± 1.10
2.77	58.0 ± 1.63
4.3	57.8 ± 1.21
4.65*	55.7 ± 1.13
6.17	57.1 ± 1.38
7.1*	55.3 ± 1.34
12.65*	55.9 ± 0.91
14.64	56.5 ± 1.33
18.25*	59.2 ± 0.55
20.22	61.0 ± 0.74
22.35*	62.4 ± 1.08
23.68	56.3 ± 0.69
25.63	59.2 ± 1.34
26*	55.0 ± 1.05
27.75*	54.8 ± 1.10
28.75	59.7 ± 1.09
30.15*	54.9 ± 1.20

*Calculated using data in Štědrá et al. (2016).

Bahlburg, H., Dobrzinski, N., 2011. A review of the Chemical Index of Alteration (CIA) and its application to the study of Neoproterozoic glacial deposits and climate transitions. Geological Society, London, Memoirs, 36(1): 81-92.

Brantley, S.L., Lebedeva, M.I., Balashov, V.N., Singha, K., Sullivan, P.L., Stinchcomb, G., 2017. Toward a conceptual model relating chemical reaction fronts to water flow paths in hills. Geomorphology, 277: 100-117.

Braun, J.J., Ngoupayou, J.R.N., Viers, J., Dupre, B., J.P., B.B., Boeglin, J.L., Robain, H., Nyeck, B., Freydier, R., Nkamdjou, L.S., Rouiller, J., Muller, J.P., 2005. Present weathering rates in a humid tropical watershed: Nsimi, South Cameroon. GCA, 69(2): 357-387.

Braun, J.J., Marechal, J.C., Riotte, J., Boeglin, J.L., Bedimo Bedimo, J.P., Ndam Ngoupayou, J.R., Nyeck, B., Robain, H., Sekhar, M., Audry, S., Viers, J., 2012. Elemental weathering fluxes and saprolite production rate in a Central African lateritic terrain (Nsimi, South Cameroon). GCA, 99: 243-270.

Buss, H.L., Sak, P.B., Webb, S.M., Brantley, S.L., 2008. Weathering of the Rio Blanco quartz diorite, Luquillo Mountains, Puerto Rico: Coupling oxidation, dissolution, and fracturing. GCA, 72(18): 4488-4507.

Buss, H.L., Lara, M.C., Moore, O.W., Kurtz, A.C., Schulz, M.S., White, A.F., 2017. Lithological influences on contemporary and long-term regolith weathering at the Luquillo Critical Zone Observatory. GCA, 196: 224-251.

Chabaux, F., Blaes, E., Stille, P., Roupert, R.D., Pelt, E., Dosseto, A., Ma, L., Buss, H.L., Brantley, S.L., 2013. Regolith formation rate from U-series nuclides: Implications from the study of a spheroidal weathering profile in the Rio Icacos watershed (Puerto Rico). Geochimica Et Cosmochimica Acta, 100: 73-95.

Dannhaus, N., Wittmann, H., Krám, P., Christl, M., von Blanckenburg, F., 2018. Catchment-wide weathering and erosion rates of mafic, ultramafic, and granitic rock from cosmogenic meteoric $^{10}Be/^{9}Be$ ratios. GCA, 222: 618-641.

Deer, W.A., Howie, R.A., Zussman, J., 2013. An Introduction to the Rock-Forming Minerals. The Mineralogical Society, London, 498 pp.

Hewawasam, T., von Blanckenburg, F., Bouchez, J., Dixon, J.L., Schuessler, J.A., Maekeler, R., 2013. Slow advance of the weathering front during deep, supply-limited saprolite formation in the tropical Highlands of Sri Lanka. GCA, 118: 202-230.

Krám, P., Hruška, J., Shanley, J.B., 2012. Streamwater chemistry in three contrasting monolithologic Czech catchments. Applied Geochemistry, 27(9): 1854-1863.

Nwaogu, C., 2014. Mobility and biogeochemical cycling of base cations (Ca and Mg) during weathering processes in a sensitive forest ecosystem, Lysina, Slavkov Forest, Czech Republic. M.Sc. Thesis, Czech University of Life Sciences, Prague.

Štědrá, V., Jarchovský, T., Krám, P., 2016. Lithium-rich granite in the Lysina-V1 borehole in the southern part of the Slavkov Forest, western Bohemia. Geoscience Research Reports, 49: 137-142.

Vázquez, M., Ramírez, S., Morata, D., Reich, M., Braun, J.-J., Carretier, S., 2016. Regolith production and chemical weathering of granitic rocks in central Chile. Chemical Geology, 446: 87-98.

West, A., Galy, A., Bickle, M., 2005. Tectonic and climatic controls on silicate weathering. Earth and Planetary Science Letters, 235(1-2): 211-228.

White, A.F., Blum, A., 1995. Effects of climate on chemical weathering in watersheds. GCA, 59(9): 1729-1747.

White, A.F., Bullen, T.D., Schultz, M.S., Blum, A.E., Huntington, T.G., Peters, N.E., 2001. Differential rates of feldspar weathering in granitic regoliths. Geochimica et Cosmochimica Acta, 65: 847-869.

White, A.F., Blum, A.E., Schulz, M.S., Huntington, T.G., Peters, N.E., Stonestrom, D.A., 2002. Chemical weathering of the Panola Granite: Solute and regolith elemental fluxes and the dissolution rate of biotite. In: Hellmann, R., Wood, S.A. (Eds.),

Water-rock Interaction, Ore Deposits, and Environmental Geochemisty: A tribute to David A. Crerar. The Geochemical Society, pp. 37-59.